

**SEISMIC VELOCITY CONTRASTS AND TEMPORAL CHANGES
OF STRIKE-SLIP FAULTS IN CENTRAL CALIFORNIA**

A Dissertation
Presented to
The Academic Faculty

by

Peng Zhao

In Partial Fulfillment
of the Requirements for the Degree
DOCTOR OF PHILOSOPHY (GEOLOGICAL SCIENCES) in the
SCHOOL OF EARTH AND ATMOSPHERIC SCIENCES, GEORGIA INSTITUTE OF
TECHNOLOGY

Georgia Institute of Technology
December 2010

**SEISMIC VELOCITY CONTRASTS AND TEMPORAL CHANGES
OF STRIKE-SLIP FAULTS IN CENTRAL CALIFORNIA**

Approved by:

Dr. Zhigang Peng, Advisor
School of Earth and Atmospheric Sciences
Georgia Institute of Technology

Dr. Karim Sabra
School of Mechanical Engineering
Georgia Institute of Technology

Dr. Andrew Newman
School of Earth and Atmospheric Sciences
Georgia Institute of Technology

Dr. Dominic Assimaki
School of Civil and Environmental
Engineering
Georgia Institute of Technology

Dr. Josef Dufek
School of Earth and Atmospheric Sciences
Georgia Institute of Technology

Date Approved: August 2, 2010

To my parents

ACKNOWLEDGEMENTS

I would like to first thank my advisor Dr. Zhigang Peng for his leadership and enthusiastic advice during my Ph.D. study. None of this work would be done without him. His support and guidance throughout my graduate studies has helped me to attain a broader picture of the Earth Sciences. Ambient noise study in this work benefits from the stimulating discussion with Dr. Karim Sabra. I would also thank my committee members Dr. Andrew Newman, Dr. Josef Dufek, and Dr. Dominic Assimaki for their valuable guidance and critical comments.

This work also benefits from the discussion and helps from many researchers. I would like to give my thanks to Dr. Yehuda Ben-Zion, Dr. Leland Timothy Long, Zheqiang Shi, Michael Lewis, Jeff Hoefft, Chuquan Wu, Kevin Chao, and Chi-Chia Tang. Fault zone trapped waves synthetic code is from Dr. Yehuda Ben-Zion.

Financial support for my studies was provided by the National Science Foundation grant EAR-0710959, the U.S. Geological Survey's NEHRP program G09AP00114, and Georgia Institute of Technology.

I would also like to thank many people during my study in Georgia Institute of Technology. They are Dr. Xiaofeng Jia, Dr. Carol Paty, Morris Jones, Lujia Feng, Ming-Chu Chen, James Lowell, Jenn Telling, Dr. Wenyue Xu, Xiaofeng Meng, Yan Luo, Shiqing Xu, and Wenzheng Yang. In particular, Jaime Convers is always willing to provide help and humor when things got rough. Dr. Kurt Frankel introduces me the beauty of Geology and nature.

Last but not least, I thank my parents for their support and understanding. To them I dedicate this work.

TABLE OF CONTENTS

	Page
ACKNOWLEDGEMENTS.....	iv
LIST OF FIGURES.....	ix
SUMMARY.....	xii
INTRODUCTION.....	1
 <u>CHAPTER</u>	
1 VARIATIONS OF THE VELOCITY CONTRAST AND RUPTURE PROPERTIES OF M6 EARTHQUAKES ALONG THE PARKFIELD SECTION OF THE SAN ANDREAS FAULT	
.....	5
SUMMARY.....	5
1.1 INTRODUCTION.....	6
1.2 TECTONIC SETTING AND PREVIOUS STUDIES OF VELOCITY STRUCTURES AROUND THE PARKFIELD SECTION OF THE SAF.....	9
1.3 SEISMIC FAULT ZONE HEAD WAVES.....	13
1.4 DATA AND ANALYSIS PROCEDURE.....	16
1.5 VARIATIONS OF THE VELOCITY CONTRAST ALONG THE STRIKE OF THE SAF.....	22
1.6 VARIATIONS OF THE VELOCITY CONTRAST WITH HYPOCENTRAL DEPTH.....	25
1.7 POSSIBLE REVERSAL OF VELOCITY CONTRAST BETWEEN MM AND GH.....	29
1.8 DISCUSSION.....	32
2 VELOCITY CONTRAST ALONG THE CALAVERAS FAULT FROM ANALYSIS OF FAULT ZONE HEAD WAVES GENERATED BY REPEATING EARTHQUAKES	

.....	39
SUMMARY.....	39
2.1 INTRODUCTION.....	39
2.2 REPEATING EARTHQUAKE IDENTIFICATION.....	41
2.3 WAVEFORM STACKING AND ALIGNMENT.....	42
2.4 VARIATIONS OF VELOCITY CONTRAST ALONG STRIKE AND DEPTH.....	46
2.5 DISCUSSION.....	48
3 DEPTH EXTENT OF DAMAGE ZONES AROUND THE CENTRAL CALAVERAS FAULT FROM WAVEFORM ANALYSIS OF REPEATING EARTHQUAKES	
.....	51
SUMMARY.....	51
3.1 INTRODUCTION.....	52
3.2 BACKGROUND AND REPEATING CLUSTER IDENTIFICATION.....	56
3.3 ANALYSIS PROCEDURE.....	60
3.4 SPATIAL VARIATIONS OF TEMPORAL CHANGES.....	66
3.4.1 General Observations.....	66
3.4.2 Possible Regions of Temporal Changes.....	68
3.4.3 Depth Extent of the Damage Zone around Station CCO.....	69
3.5 DISCUSSION.....	72
3.6 APPENDIX: ESTIMATION OF TEMPORAL CHANGES OF A THREE-MEDIA FAULT MODEL USING SYNTHETIC SEISMOGRAMS.....	82
4 DETECTING REMOTELY TRIGGERED TEMPORAL CHANGES AROUND THE PARKFIELD SECTION OF THE SAN ANDREAS FAULT	
.....	86

SUMMARY.....	86
4.1 INTRODUCTION.....	87
4.2 DATA AND ANALYSIS PROCEDURE.....	92
4.3 MEASURING TEMPORAL CHANGES FROM EGFS.....	96
4.4 RESULTS.....	100
4.5 DISCUSSION.....	103
RECAPTULATION.....	108
REFERENCES.....	111

LIST OF FIGURES

	Page
Figure 1.1: (a) A map of the Parkfield section of the San Andreas Fault and locations of seismic networks; (b) along-strike locations of ~9000 relocated microearthquakes and 1966 and 2004 M6 Parkfield earthquake.....	11
Figure 1.2: Velocity model in the Parkfield from Thurber et al. (2006).....	13
Figure 1.3: Relation between critical normal distances vs. velocity contrast for different propagating distances of fault zone head waves	15
Figure 1.4: Examples of different quality factors for head waves phase picking.....	20
Figure 1.5: Plot of FZHW recorded at station MMNB and estimated velocity contrasts from two sides of the stations.....	21
Figure 1.6: Plot of FZHW recorded at station CRAB and estimated velocity contrasts from two sides of the stations.....	23
Figure 1.7: Plot of FZHW recorded at station EADB and estimated velocity contrasts from two sides of the stations.....	24
Figure 1.8: A summary of velocity contrasts in the Parkfield area.....	25
Figure 1.9: Plots of FZHW and estimated velocity contrasts from microearthquakes directly beneath stations MMNB and GHIB, respectively.....	27
Figure 1.10: Plot of FZHW recorded at station GHIB from events shallower than 7 km	28
Figure 1.11: Plot of vertical seismograms recorded at station GHIB from events deeper than 7 km.....	29
Figure 1.12: Plot of vertical seismograms recorded at station PHA.....	31
Figure 1.13: Focal mechanism of selected events from “suspected” region with reversed velocity contrast (Figure 1.2) and the events marked with red circles in Figure 1.12.....	32
Figure 1.14: Location of high-velocity igneous rocks NE of SAF near GH.....	35
Figure 1.15: Regional isostatic gravity map near Parkfield section.....	35
Figure 2.1: (a) A map of central Calaveras Fault and station locations; (b) locations of 353 repeating clusters in the cross-section view along the fault.....	41

Figure 2.2: Examples of waveforms from Cluster C243 recorded at four different stations with the stacked results.....	44
Figure 2.3: Plots of moveout of FZHW recorded at stations CCO and CMH with corresponding estimated velocity contrast.....	45
Figure 2.4: Fitting of differential arrival time between FZHW and direct P waves for events from different segments recorded at station CCO and CMH.....	47
Figure 2.5: Schematic summary of the results from the traveltimes analysis of FZHW at stations CCO and CMH.....	50
Figure 3.1: (a) A map of central Calaveras Fault and station locations; (b) locations of 333 repeating clusters in the cross-section view along the fault.....	57
Figure 3.2: Cross-section views of 15 events within cluster C127 in both along-strike and normal directions.....	59
Figure 3.3: Comparison of locations of repeating clusters from this thesis, Rubin (2002), and Templeton et al. (2009) in the cross-section view.....	60
Figure 3.4: (a) Vertical seismograms of Cluster C127 recorded at station CCO; (b) calculated delay time and (c) de-correlation index using moving-window cross-correlation technique.....	62
Figure 3.5: An illustration of median delay time vs. logarithmic elapsed time since the 1984 mainshock.....	65
Figure 3.6: Median delay time against the logarithmic elapsed time since the 1984 Morgan Hill earthquake for the vertical-component seismograms recorded at the 6 stations.....	66
Figure 3.7: Delay-time at one day after the 1984 mainshock versus depths of events for all 6 stations.....	68
Figure 3.8: Median delay time plotted against the logarithmic elapsed time after the 1984 mainshock for seismograms recorded at station CCO from three segments (Figure 3.1b).....	71
Figure 3.9: Delay-time at one day after the 1984 mainshock versus depths of events recorded at station CCO from different segments (Figure 3.1b).....	71
Figure 3.10: Median delay time plotted against the logarithmic elapsed time after the 1984 mainshock for repeating clusters from different depths.....	76
Figure 3.11: A schematic diagram of the damage zone near station CCO.....	77
Figure 3.A1: A schematic 3-medium fault model.....	83

Figure 3.A2: (a) Synthetic waveforms generated from the model in Figure A.1 at different depths; (b) Calculated delay-time from (a); (c) median values of delay-time in (b) vs. depths; (d) slopes of delay-time in (b) vs. depths.....	85
Figure 4.1: Changes of decorrelation index of repeating earthquakes in Parkfield after the 2004 great Sumatra earthquake.....	89
Figure 4.2: An illustration of seismic ambient noise cross-correlation technique.....	91
Figure 4.3: Seismic velocity change near Parkfield section using ambient noise cross-correlation technique.....	92
Figure 4.4: A map of the Parkfield section of SAF and locations of 10 HRSN stations...	94
Figure 4.5: Waveforms of the daily Empirical Green Functions (EGFs) between the station pair CCRB and MMNB before and after the 2004 M6 Parkfield earthquake.....	96
Figure 4.6: An illustration of the stretch/compression method.....	99
Figure 4.7: An illustration of the de-correlation index method.....	100
Figure 4.8: (a) Median velocity changes from all station pairs versus the occurrence dates relative to the 2004 M6 Parkfield earthquake; (b) Median value of de-correlation index versus the occurrence dates relative to the 2004 M6 Parkfield earthquake.....	101
Figure 4.9: Temporal changes in the median velocity changes associated with the four regional/teleseismic events.....	102
Figure 4.10: Temporal changes in the median de-correlation indexes associated with the four regional/teleseismic events.....	103

SUMMARY

The spatial patterns of bimaterial interfaces along the Parkfield section of the San Andreas Fault (SAF) and central section of the Calaveras Fault are systematically investigated with large data sets of near-fault waveforms. Different from the usage of direct P and S waves in traditional tomographic studies, a particular seismic phase named fault zone head wave (FZHW) is used to image the bimaterial fault interfaces. The results show clear variations of seismic velocities contrast both along-strike and along-depth directions in both regions, which is in general consistent with local geological setting at surface and existing 3D tomography results. In the Parkfield section of SAF, the result of velocity contrast is used to test the relationship between preferred rupture directions of M6 Parkfield earthquakes and bimaterial interface. Strong velocity contrast ($\sim 5\text{-}10\%$) near Middle Mountain (MM) could control the rupture directions of nearby earthquakes to SE, such as the case for 1966 M6 Parkfield earthquake. In comparison, weak velocity contrast ($\sim 0\text{-}2\%$) near the epicenter of the 2004 Parkfield M6 earthquake (i.e., Gold Hill) probably has no influence on controlling its rupture direction, which is consistent with the bilateral rupture of the 2004 Parkfield earthquake. In the central Calaveras Fault, a detailed analysis of the moveout between FZHWs and direct P waves revealed the existence of a complicated fault structure with velocity contrast increasing from NW to SE of station CCO. The high velocity contrast SE of station CCO could be caused by a low-velocity zone SE of station CCO.

The spatio-temporal variations of seismic velocity around the central Calaveras Fault and its nearby region are investigated based on the waveform analysis of 333

repeating clusters following the 1984 $M_L 6.2$ Morgan Hill earthquake. Clear reduction of seismic velocity is shown for all repeating clusters immediately after the mainshock, followed by a logarithmic recovery. The coseismic change mostly occurs at shallow layers (top few hundred meters) for the region away from the rupture area of the mainshock, but extends much deeper around the rupture zone of the Morgan Hill earthquake. The estimated depth of the damage zone is up to 6 km in the fault based on the repeating clusters directly beneath station CCO.

Finally, temporal changes around the Parkfield section of SAF are studied using recently developed ambient noise cross-correlation technique. The extracted daily empirical Green functions (EGFs) from 0.4-1.3 Hz noise records are used to estimate subtle temporal changes associated with large earthquakes from local to teleseismic distances. The results show clear coseismic reduction of seismic velocities after the 2004 M_6 Parkfield earthquake, similar to the previous observation based on repeating earthquakes. However, no systematic changes have been detected for other four regional/teleseismic events that have triggered clear tremor activity in the same region. These results suggest that temporal changes associated with distance sources are very subtle or localized so that they could not be detected within the resolution of the current technique ($\sim 0.2\%$).

INTRODUCTION

Large earthquakes ($M > 6$) occur on major active faults such as the San Andreas Fault (SAF) in California. An accurate determination of fault zone (FZ) properties at seismogenic depth is critical for us to better understand many aspects of earthquake physics, including faulting mechanism, temporal evolution of FZ during earthquake cycle, seismic hazard near active FZs, and interaction between FZ and earthquakes. Dense regional seismic networks in California with permanent and temporal stations provide abundant dataset to investigate the internal structures and time-varying properties of FZs using seismic methods. This thesis takes advantage of high-quality seismograms recorded in many near-fault stations in the Parkfield section of San Andreas Fault (SAF) and the central Calaveras Fault to image the bimaterial interfaces and detect temporal changes of FZ properties associated with large nearby and teleseismic earthquakes.

Due to long-term fault movements, strike-slip faults generally juxtapose rocks with different elastic properties on two sides, forming well-defined bimaterial fault interfaces. Properties of earthquake ruptures on a bimaterial interface and associated seismic radiation are significantly different from those expected for a fault in a homogenous medium (e.g., Ben-Zion 1989; Ben-Zion and Aki 1990). To image these bimaterial interfaces, a unique phase called fault zone head waves (FZHW) is used, which provide a high-resolution image of the bimaterial fault interface than traditional body-wave tomography methods (Ben-Zion and Malin 1991; Ben-Zion et al. 1992). So far FZHW were only observed along the northern part of the Parkfield section along the SAF with a relative small dataset (Ben-Zion and Malin 1991) and south of Hollister

(McGuire and Ben-Zion 2005; Lewis et al 2007). The first two chapters of this thesis deal with systematic analysis of large sets of seismic waveforms data for imaging the bimaterial fault interfaces along the entire Parkfield section of SAF and the central Calaveras Fault.

In Chapter 1 (Zhao et al. 2010), we use the waveforms of ~ 9000 microearthquakes recorded by several seismic networks around the Parkfield section of SAF to obtain the first-order bimaterial interface properties. The result shows clear variation of velocity contrast in the along-strike direction. The strongest velocity contrast ($\sim 5\text{-}10\%$) is found near Middle Mountain (MM) and it systematically decreases to $\sim 0\text{-}2\%$ near Gold Hill (GH). However, we did not observe any reversal of velocity contrast along the active fault interface near GH, as suggested from previous tomography results (e.g., Thurber et al. 2006). We also use the obtained velocity-contrast information to explain the mixed rupture directions of the M6-type Parkfield earthquake sequences.

In Chapter 2 (Zhao and Peng 2008), the first-order bimaterial interface properties of the central Calaveras Fault are investigated using about 8000 relocated events (Schaff et al., 2002). To reduce the number of events, we first stack waveforms from a total of 353 repeating clusters and then pick the phases for FZHW and direct waves manually from these stacked seismograms. The obtained velocity contrasts are 2-3% and 12-14% NW and SE of station CCO, respectively. These results are consistent with the interpretation that in the NW the fault interface is relatively simple and sharp, while in the SE, the fault structure is complicated with a presence of a low-velocity zone.

In addition to the spatial properties of FZs, such as velocity contrast, it is also important to understand the temporal variations of FZ properties. In last ten years, many

studies based on artificial repeatable sources/repeating earthquakes have reported that the occurrences of local large earthquakes can weaken the strength of FZ materials and result in reduction of seismic velocity and increase of attenuation (Vidale and Li 2003; Rubinstein and Beroza 2004a, b; Peng and Ben-Zion 2006). These observed short-term temporal changes might help us to understand the initiation and evolution of damage zones of strike-slip faults in the geological time scale after many earthquakes cycles (e.g., Vidale and Li 2003). Chapter 3 documents clear temporal changes in the near-surface layers and around the rupture area of the central Calaveras fault following the 1984 M_l 6.2 Morgan Hill earthquake. The obtained results are used to constrain the spatial extension of the damage zone induced by this mainshock. Finally, recent observations of remote triggered tremors (e.g., Rubinstein et al., 2010; and references there in) and microearthquakes (e.g., Hill and Prejean, 2007; and references therein) raise the question about whether dynamic stresses associated with the passing surface waves of large regional/teleseismic events could perturb a fault system. This thesis tries to address this problem in the last part (Chapter 4) using the new developed ambient noise cross correlation technique (Sabra et al. 2005a, b, 2006; Brenguier et al., 2008b).

In Chapter 3 (Zhao and Peng 2009), temporal changes of FZ properties associated with the occurrence of the 1984 Morgan Hill earthquake are investigated using a set of 333 repeating earthquakes. A moving-window cross-correlation technique (Niu et al. 2003) is used to detect temporal changes between each repeating earthquake and the reference event. The largest temporal changes are observed at station CCO that is the closest station to the rupture zone of the 1984 mainshock. In addition, for this station, time delays are larger from clusters in the top 5-6 km, and decrease at larger depths. In

comparison, the time delays from other 5 stations are much smaller, and do not show clear relationship with hypocentral depths. These results are consistent with the inference of a widespread damage and non-linearity in the near-surface layers associated with strong ground motions of nearby large earthquakes, and localized damages and flower-type structures around active faults based on previous studies of FZ structures (Ben-Zion et al. 2003; Peng et al. 2003; Peng and Ben-Zion 2004) and recent 3-D numerical simulations (e.g., Ma 2008).

In Chapter 4 (Zhao et al. 2010), a systematic search of temporal changes along the Parkfield section of the SAF is conducted by cross-correlating relatively high-frequency (0.4-1.3 Hz) ambient noise signals recorded by 10 borehole stations of the High Resolution Seismic Network. Using both stretch/compressed and moving-window cross-correlation techniques to measure the delay time and the decorrelation-index between the daily empirical Green Functions (EGFs), clear changes have been found from both median seismic velocity and decorrelation-index associated with the 2004 M6 Parkfield earthquake. Then the same procedure is applied to the data around four regional/teleseismic events that have triggered non-volcanic tremor in the same region, in order to investigate the interaction between large earthquakes from large distances and fault zone systems. These results suggest that temporal changes associated with distance sources are very subtle or localized so that they could not be detected within the resolution of the current technique ($\sim 0.2\%$).

CHAPTER 1

**VARIATIONS OF THE VELOCITY CONTRAST AND RUPTURE
PROPERTIES OF M6 EARTHQUAKES ALONG THE PARKFIELD
SECTION OF THE SAN ANDREAS FAULT**

Summary

The work in this chapter is published in Zhao et al. (2010a). We investigate the seismic velocity contrast across the San Andreas Fault (SAF) in the Parkfield area using fault zone head waves (FZHW) that propagate along the bimaterial fault interface and direct P waves. We systematically analyze large data sets of near-fault waveforms recorded by several seismic networks over the period 1984–2005. Clear FZHW are observed at many stations on the NE side of the fault in the creeping section of the SAF north of Middle Mountain (MM). This indicates the presence of a sharp bimaterial interface and that the NE side of the fault has lower seismic velocities in that region. The obtained P-wave velocity contrast is about 5–10% north of MM, and it systematically decreases to 0–2% near Gold Hill (GH). The along-strike variations of the velocity contrast are consistent with geological observations of a sliver of high-velocity rock immediately to the NE of the SAF near GH, associated with the GH fault, and existing 3-D seismic tomography results. The obtained imaging results offer an explanation for the mixed rupture directions of the Magnitude (M) 6 type Parkfield earthquakes. The strong velocity contrast around MM is expected to produce a preferred propagation direction to the SE for earthquakes that nucleate near MM (e.g. the 1934 and 1966 Parkfield

earthquakes). In contrast, the near-zero velocity contrast and multiple fault branches near GH imply that earthquakes that nucleate near GH (e.g. the 2004 Parkfield earthquake) are not expected to have a preferred propagation direction to the SE, and are likely to propagate in directions that are controlled by other factors such as structural and stress heterogeneities. The observed systematic reduction of the velocity contrast along the SAF from NW of MM to SE of GH provides a dynamic arrest mechanism for earthquakes that nucleate in the northern part of the Parkfield section and propagate to the SE, and a dynamic arrest mechanism for earthquakes that nucleate in the southern section and propagate to the NW.

1.1 Introduction

Large earthquakes occur on major fault structures. Due to long-term tectonic movements, such faults tend to juxtapose rocks of different elastic properties, resulting in well-defined bimaterial interfaces. Contrasts of elastic properties across large faults have been imaged by seismic reflection and refraction studies (e.g. Fuis et al. 2001, 2003; Catchings et al. 2002; Lutter et al. 2004), body and surface wave tomography (e.g. Eberhart-Phillips and Michael 1993; Shapiro et al. 2005; Thurber et al. 2006), modeling of geodetic data (Le Pichon et al. 2005; Fialko 2006; Wdowinski et al. 2007) and analysis of fault zone head waves (FZHW) that refract along the biomaterial fault interfaces (Ben-Zion and Malin 1991; Ben-Zion et al. 1992; Hough et al. 1994; McGuire and Ben-Zion 2005; Lewis et al. 2007; Zhao and Peng 2008).

Properties of earthquake ruptures on a bimaterial interface and associated seismic radiation can be significantly different from those expected for a fault in a homogenous

solid (e.g. Weertman 1980; Andrews and Ben-Zion 1997; Ranjith and Rice 2001; Ben-Zion 2001). In contrast to the case of a homogenous solid, ruptures on a planar bimaterial interface produce dynamic changes of normal stress σ_n that depend on the spatial derivative of in-plane slip, material properties, rupture velocity, and the direction of rupture propagation. For standard subshear ruptures the change of σ_n at the tip propagating in the direction of slip of the compliant solid (referred to as the “preferred” direction) is tensile, while the change at the tip propagating in the opposite direction is compressive. For supershear ruptures, the senses of changes of σ_n are reversed (Weertman 2002; Shi and Ben-Zion 2006). The amplitudes of the near-tip changes increase with propagation distance along the bimaterial interface due to a continual transfer of energy to shorter wavelengths (e.g. Adams 1995; Ben-Zion and Huang 2002). The above dynamic effects produce a slip pulse that propagates for wide ranges of frictional, bimaterial contrast, and initial stress conditions predominately in the preferred direction (e.g. Shi and Ben-Zion 2006; Dalguer and Day 2007; Brietzke et al. 2007, 2009; Ampuero and Ben-Zion 2008). The seismic shaking hazard associated with earthquake ruptures depend strongly on the rupture direction (e.g. Aki and Richards 2002; Ben-Zion 2003; Olsen et al. 2006). The interaction between slip and normal traction along a bimaterial interface makes those interfaces mechanically-favored surfaces for rupture propagation (Ben-Zion and Andrews 1998; Brietzke and Ben-Zion 2006).

Many moderate and large earthquakes appear to be unilateral (McGuire et al. 2001). If the rupture propagation directions of earthquakes are affected strongly by the existence of bimaterial interfaces, the imaging of such interfaces can be used to predict a statistical preference for the propagation directions of earthquakes on the various

structures. This knowledge can greatly improve the ability to evaluate local seismic risks and mitigate earthquake hazard. The seismic data associated with the well-instrumented Parkfield section of the San Andreas Fault (SAF) in central California (e.g. Bakun et al. 2005) provide important opportunities for detailed examinations of the relations between fault zone structures and earthquake properties. The SAF in that area (Figure 1.1) juxtaposes overall a faster granitic block on the SW side against a slower Franciscan block on the NE side, but the velocity structure is associated with various local complexities (e.g. Eberhart-Phillips and Michael 1993; Rymer et al. 2006; Thurber et al. 2006). The 1966 M6 Parkfield earthquake (and presumably several previous M6 events in the area) nucleated under Middle Mountain (MM) and propagated along the SAF toward the SE, while the 2004 M6 Parkfield earthquake started near Gold Hill (GH) and propagated primarily in the opposite direction (Bakun et al. 2005).

The “opposite” propagation direction of the 2004 Parkfield event led Harris (2004) and Harris and Day (2005) to conclude that bimaterial interfaces are not important for earthquakes rupture on natural faults. Ben-Zion (2006) commented that the mixed propagation directions may be produced by local variations of the velocity structure associated with (1) a sliver of high-velocity rock immediately to the NE of the SAF, related to the GH fault, which may produce a local reversal of the velocity contrast near the hypocenter of the 2004 M6 event, and (2) the existence of two major bimaterial interfaces - the main SAF and the Southwest Fracture Zone (SWFZ) - having velocity contrasts of opposite sense. Ben-Zion (2006) pointed out that higher resolution imaging studies of bimaterial interfaces, along with better statistics, are needed to test the hypothesis of preferred propagation direction of earthquake ruptures in the Parkfield area.

In this chapter we provide detailed seismic imaging of the velocity contrast across the SAF in the Parkfield area, by systematically analyzing FZHW recorded by many near-fault seismic instruments. The results show systematic variations of the velocity contrast across the SAF that may help to explain the observed behavior of moderate and large earthquakes in the area. In the next section we describe the geological setting and previous studies of the velocity structures around Parkfield. In Section 1.3 we provide a brief review of FZHW signals and in Section 1.4 we describe details of the analysis procedure. The results are presented in Sections 1.5 to 1.7 and further discussed in Section 1.8.

1.2 Tectonic Setting and Previous Studies of Velocity Structures around the Parkfield section of the SAF

The SAF is a right-lateral strike-slip fault that extends approximately 1200 km along the boundary between the Pacific and the North American plates. The Parkfield section of the SAF straddles the transition between the creeping segment of the fault to the NW and the locked segment to the SE that last ruptured in the great 1857 Fort Tejon earthquake (Sieh 1978). At least 7 characteristic earthquakes of $\sim M6$ occurred at Parkfield since 1857, with the most recent one on September 28th 2004 (Bakun et al. 2005). The quasi-periodicity of the first 6 events led to the deployment of many seismic instruments as part of the Parkfield Earthquake Prediction Experiment (Bakun and Lindh 1985). The instrumentation was further augmented by the recent development of the SAFOD project (Hickman et al. 2004).

The surface geological setting around Parkfield is complicated. In general, the rock types in this section are characterized by faster Salinian granite on the SW side of the fault, and slower Franciscan rocks and Great Valley sequence on the NE side (Page 1981; Walter and Mooney 1982; Lees and Malin 1990). However, the near-fault seismic velocity structure includes numerous local variations (e.g., Eberhart-Phillips and Michael 1993; Thurber et al. 2006). In addition, the San Andreas system between MM and GH is expressed as two principal surface traces (Brown et al. 1967; Rymer et al. 2006): the main SAF and the SWFZ (Figure 1.1). The main SAF surface trace shows a right-stepping offset across the Cholame Valley south of GH. This offset is considered to be the northern end of the locked segment that ruptured in the 1857 event, and responsible for bounding the southern rupture extents of the M6 Parkfield earthquakes (Lindh and Boore 1981).

While the detailed near-surface structures of the San Andreas system appear complicated, the relocated seismicity outlines a much simpler fault at seismogenic depth (Waldhauser et al. 2004; Thurber et al. 2006). The aftershocks of the 2004 Parkfield earthquake concentrate along the same locations associated with the pre-2004 seismicity, and form a linear trend that is directly beneath the SWFZ rather than the main SAF (Waldhauser et al. 2004; Thurber et al. 2006; Simpson et al. 2006). The seismicity trend connects to the creeping and locked sections of the SAF without obvious bends, suggesting that the SAF is expressed as a single planar fault at seismogenic depth (Eberhart-Phillips and Michael 1993; Thurber et al. 2006). Based on this and other geological observations, Simpson et al. (2006) suggested that the step-over and the wrapping of the main SAF to the NE is a consequence, rather than the cause, of the

segmentation of the ~M6 Parkfield earthquakes and the locked patch further south that last ruptured in the 1857 Fort Tejon earthquake.

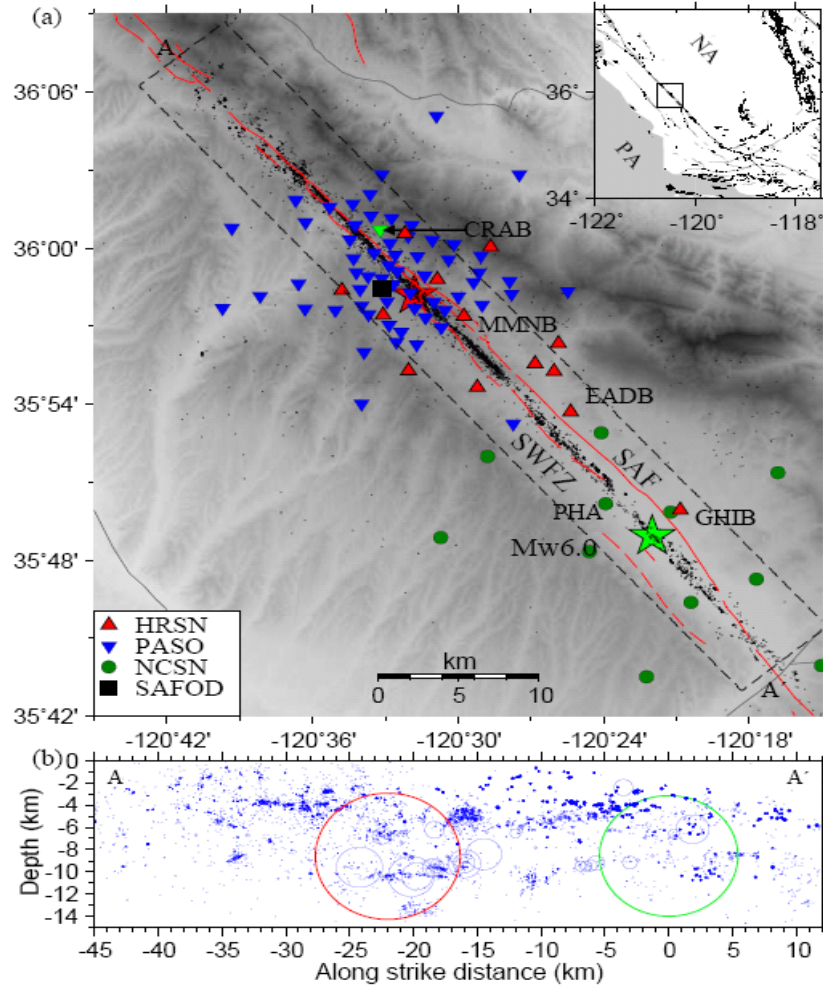


Figure 1.1. (a) A map of the Parkfield section of the San Andreas fault (SAF). The background seismicity from 1984 and 2005 (Thurber et al. 2006) and the epicenters of the 1966 and 2004 M6 Parkfield earthquakes are marked with small dots, and red and green stars, respectively. The red lines denote surface traces of faults. Seismic stations of several networks are shown with different symbols. Selective station names are marked. The background is shaded topography with white being low and dark being high. The inset shows the area on a map of California. SAF: the main San Andreas fault; SWFZ: Southwest Fracture Zone. (b) Hypocenters of about 9000 earthquakes inside the dashed box along the cross-section AA' (139.2° strike) in (a). The radius of each circle is estimated from its magnitude, based on a moment-magnitude relationship (Abercrombie 1996) with a circular crack model (Eshelby 1957) assuming a nominal 3-MPa stress drop. The red and green circles mark the hypocenters of the 1966 and 2004 M6 Parkfield earthquakes, respectively.

Several local earthquake tomography models have been developed for a wide region around Parkfield (Lee and Malin 1990; Eberhart-Phillips and Michael 1993; Thurber et al. 2006), and a small region around MM (Michellini and McEvilly 1991; Thurber et al. 2003, 2004). A common feature among these models is a clear seismic velocity gradient across the SAF, with SW being overall fast and NE being overall slow, which is generally consistent with the geological observation at the surface. Ben-Zion and Malin (1991) observed FZHW at several stations on the NE side of the SAF, indicative of a sharp velocity contrast, and derived from the moveout between the head and direct P waves an average velocity contrast of about 5% across the SAF near MM. Ben-Zion et al. (1992) inverted arrival times of FZHW and direct P waves for depth-variations of the velocity contrast near MM, and obtained values that range from 10-20% in the top 3 km and 3-7% in the deeper section.

Eberhart-Phillips and Michael (1993) and Thurber et al. (2006) imaged in tomography studies the existence of a high-velocity rock on the (nominally slow) NE side of the fault at seismogenic depth near GH (Figure 1.2). This high-velocity body has a maximum P wave velocity of 6.6 km/s, and is assumed to consist of the greenstones and mafic rocks of the Permanente Terrane (McLaughlin et al. 1996). Thurber et al. (2006) suggested that this high-velocity body is very close to or in contact with the SAF interface at depth, and might be spatially related to the area of primary slip (10 cm or more) during the 2004 Parkfield mainshock (Langbein et al. 2005).

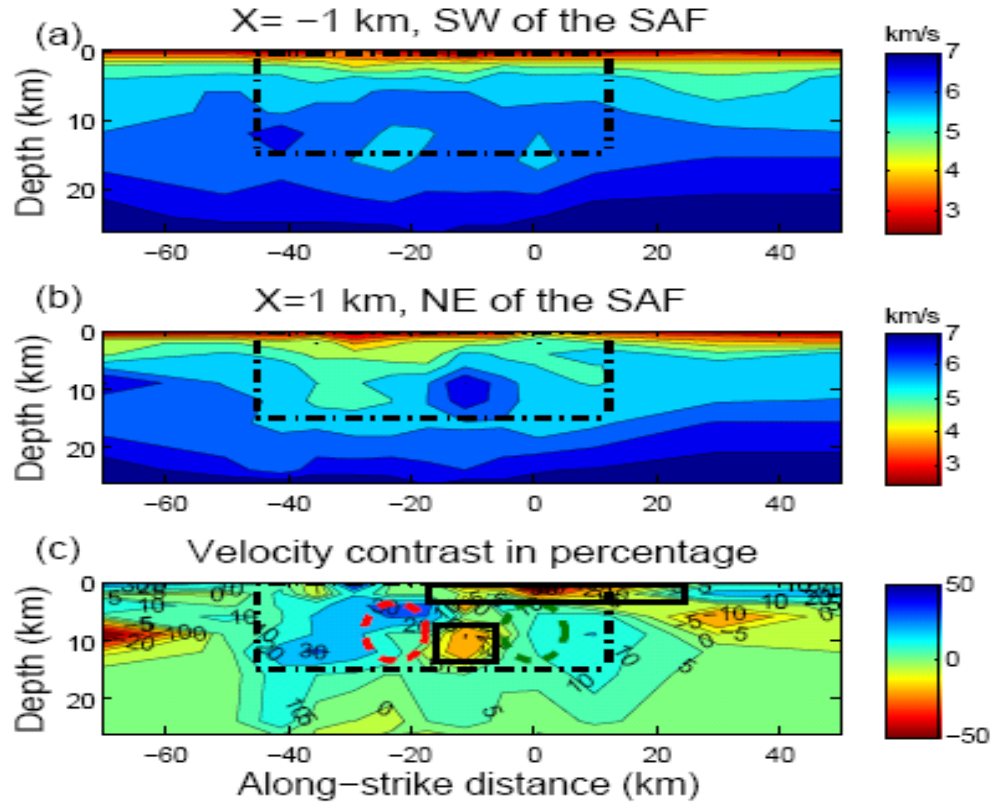


Figure 1.2. A velocity model from Thurber *et al.* (2006) at (a) $x = -1$ km, SW of the SAF and (b) $x = 1$ km, NE of the SAF. (c) The velocity contrast in percentage along the fault-strike and downdip directions, obtained by dividing the difference with the averaged velocity shown in (a) and (b). The positive number corresponds to faster velocity in the SW side. Two black rectangles roughly outline the two regions with reversed velocity contrast larger than 5% (i.e. the NE side has faster velocity than the SW side). The red and green dashed circles mark, respectively, the hypocenters of the 1966 and 2004 Parkfield M6 events. The dashed black boxes correspond to the region shown in Figure 1.1b.

1.3 Seismic Fault Zone Head Waves

Unlike the aforementioned tomography studies that use travel times of the direct P or S waves to image properties of volumetric rock elements, we utilize FZHW to image directly the bimaterial interface along the Parkfield section of the SAF. A sharp material contrast across a fault interface should generate FZHW that spend a large portion of their

propagation paths refracting along the bimaterial interface (Ben-Zion 1989, 1990; Ben-Zion and Aki 1990). The FZHW propagate along the fault with the velocity and motion polarity of the block with faster seismic velocity. From the bimaterial interface, the FZHW are radiated to the slower velocity side, where they are characterized by an emergent waveform with opposite motion polarity to that of the direct body wave. The FZHW are the first arriving phases at locations on the slower block with normal distance to the fault (Ben-Zion 1989) less than a critical distance x_c given by

$$x_c = r \cdot \tan[\cos^{-1}(\alpha_2 / \alpha_1)], \quad (1.1)$$

where r is the distance that the FZHW propagate along the bimaterial interface and α_1 , α_2 are the average P wave velocities of the faster and slower media, respectively. Figure 1.3 illustrates the relations between the velocity contrast and critical distance x_c for different along-fault distances r . For a given distance r , smaller values of the velocity contrast require stations that are closer to the fault to detect the FZHW. With known values of r and normal distances of stations from the fault, Figure 1.3 could be used to place limits on the velocity contrast, as done in Section 1.7 of the paper.

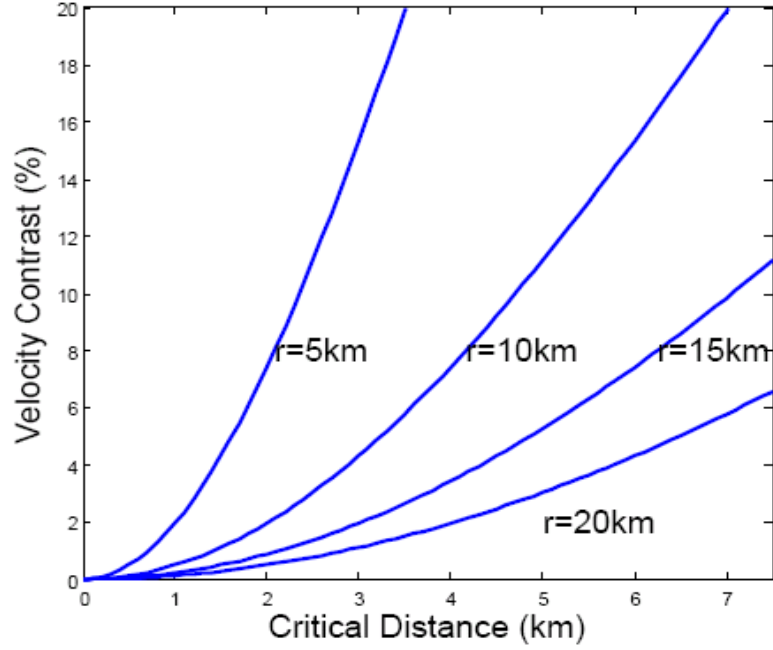


Figure 1.3. The critical normal distance from the fault x_c vs. the value of velocity contrast as a function of along-fault propagation distance r using Equation (1). FZHW are the first arrivals for the parameters above the blue curves with different propagation distances r .

Since FZHW owe their existence to and spend most of their propagation paths along the fault interface, they provide a high-resolution tool for imaging the velocity contrast across the fault, as demonstrated in previous studies (e.g., Ben-Zion et al. 1992; McGuire and Ben-Zion 2005; Lewis et al. 2007; Zhao and Peng 2008). For an interface between two different quarter spaces, the differential arrival time (Δt) between first arriving head wave and the following direct P wave grows with r (Ben-Zion and Malin 1991) as

$$\Delta t \sim r \left(\frac{1}{\alpha_2} - \frac{1}{\alpha_1} \right) \sim r \left(\frac{\Delta \alpha}{\alpha^2} \right), \quad (1.2)$$

where α and $\Delta\alpha$ denote the average and differential P wave velocities, respectively. In this study, we use Equation (1.2) to estimate along-strike variations of the velocity contrast in the Parkfield section of the SAF.

As mentioned, Ben-Zion and Malin (1991) and Ben-Zion et al. (1992) used head and direct P waves to image the velocity contrast across the SAF near MM. Ben-Zion et al. (1992) also demonstrated with numerical tests that including FZHW can significantly improve the resolution of the velocity structure near the fault. However, these studies only utilized a small data set associated with about 100 earthquakes NW of MM, and hence did not provide detailed images of the velocity contrast at different along-strike locations, and in particular around the epicenter of the 2004 Parkfield event near GH. In the following sections we conduct a comprehensive analysis of FZHW and P body waves for the velocity contrast across the SAF at different along-strike positions, using all the available relevant seismic data in the Parkfield area from 1984 to 2005.

1.4 Data and Analysis Procedure

The seismic data analyzed in this study are recorded by two permanent networks, the Northern California Seismic Network (NCSN) operated by the United States Geological Survey (USGS) and the High Resolution Seismic Network (HRSN) operated by the Berkeley Seismological Laboratory (BSL), along with one temporary Incorporated Research Institutions for Seismology (IRIS) Program for Array Seismic Studies of the Continental Lithosphere (PASSCAL) deployment, the Parkfield Area Seismic Observatory (PASO) Network (Thurber et al. 2003). Most surface instruments (NCSN and PASO) are 1Hz L4C or 2Hz L22 short-period velocity sensors with a sampling rate

of 100/s. In the PASO network, 29 stations are equipped with Guralp 40T broadband instruments. The 13 HRSN 2 Hz or 4.5 Hz short-period sensors are deployed in 100-300m deep boreholes and have a sampling rate of 250/s. In this study, we only analyze waveforms recorded by the vertical component. The hypocenter locations and origin times of earthquakes are obtained from the relocated catalog of Thurber et al. (2006).

The employed analysis procedure is as follows. First, we select events occurring near the SAF. Because the majority of the seismicity in Parkfield appears as one linear trend beneath the surface traces of the SWFZ (Figure 1.1), we only use events within 1 km of the linear seismicity trend. The strike of this trend is 139.2° clockwise from the North and we use the epicenter of the 2004 M6 event (120.366° , 35.815°) listed in Thurber et al. (2006) as the projection center. Next, we select high-quality waveforms with signal-to-noise ratio (SNR) ≥ 5 for the HRSN data. We use SNR ≥ 10 for the PASO and NCSN data because waveforms recorded by the surface stations are generally noisier than those from borehole instruments.

After the previous steps, we obtain about 2500 and 150 events for stations of the HRSN and PASO networks, respectively. This provides a good spatial coverage, especially around the epicenter of the 1966 Parkfield earthquake (i.e. MM). The distribution of seismic stations around the epicenter of 2004 Parkfield earthquake is relatively sparse. To balance the distribution of stations and seismicity, we select only 11 stations of the NCSN, which are located on the southern end of our study region near GH (Figure 1.1). We use about 600 events for these 11 NCSN stations, ranging from 27 km north of the epicenter of the 2004 M6 event to the southern end of our study region.

After selecting waveforms with high SNR, we remove the mean value of each trace and apply a high-pass filter with a corner frequency of 1 Hz to suppress long period noise. Because the characteristics of FZHW are best expressed in displacement seismograms, we integrate the original velocity seismograms to obtain the displacement records, and pick the onset of FZHW and direct P waves manually by examining the velocity and displacement seismograms simultaneously. We identify FZHW as emergent first arrivals with opposite motion polarities and systematic moveout from the direct P waves. The onset of the P wave is picked at a place with a sharp increase of amplitude in the displacement seismogram (Ben-Zion 1989). Moreover, we require the polarities of direct P waves to be consistent with right-lateral focal mechanisms. This is justified by the fact that ~75% of the microseismicity at Parkfield are pure strike-slip events on the near-vertical planes aligned with the seismicity trend (Thurber et al. 2006; J. L. Hardebeck, written communication 2008). We also remove records with wrong polarities generated during certain operation periods of the stations.

Next, we assign three quality factors (A, B, and C) to the picks of both FZHW and P waves. Quality A and C represent the highest and lowest confidence levels for phase picking, respectively, while Quality B is an intermediate level. The selection criteria are as follows. Phases with Quality A have both correct polarities based on right-lateral focal mechanisms and similar waveform characteristics as the synthetic solutions of the FZHW and P waves (Ben-Zion 1989, 1990). For stations on the NE of the SAF, the expected polarities of the direct P waves for events from the NW and SE along-strike directions are up and down, respectively. The direct P waves are expected to have strong sharp peaks/troughs, and the FZHW are expected to be emergent phases with opposite

polarity from that of the direct P waves (Figure 1.4a). Quality C is used when either the onset of FZHW/direct P wave is not reliable due to a low SNR value, or it is relatively difficult to determine the phase types because of waveform complexities. In Figure 1.4c the polarity of the first-arriving phase is consistent with that of a FZHW for a right-lateral focal mechanism, but the complex waveform makes it difficult to pick the onset of the direct phase. In such cases we set the qualities of both the FZHW and P wave to be C. In Figure 1.4b the polarity of the first peak suggests that it is a head wave, assuming a right-lateral focal mechanism. However, its amplitude is at the same level as the later-arriving direct P phase and there is no sharp transition in the character of the two phases as in Quality A seismograms. Hence, we set the quality factors of both head wave and direct P arrival to be B. The selection of quality factors is somewhat subjective and relies on the experience of an analyst. To confirm the quality factor of each picked phase, we also check phases of nearby events and compare the results from different stations. The results presented in the following sections are based only on phase picks with quality A or B.

Figure 1.5 shows clear examples of FZHW at station MMNB that are generated by events to the NW and SE of the station. For events with along-interface distances larger than ~ 7 km, the polarities of the first arrival phases are opposite to those predicted for right-lateral focal solutions, as expected for FZHW. In addition, the differential arrival time between FZHW and direct P waves increases generally with the along-interface distance. We fit the moveout with the least-squares method and estimate the velocity contrast based on the slope of the moveout using Equation (1.2). As in Ben-Zion and Malin (1991), we use 5.5 km/s as the average P wave velocity in Equation (2). This is consistent with the average value of seismic velocities at seismogenic depth based on the

3D velocity model of Thurber et al. (2006). The estimated average velocity contrasts are $\sim 5.1\%$ and $\sim 3.3\%$ for the fault sections to the NW and SE of station MMNB, respectively. In the next three sections we perform similar analysis using data that are recorded at different stations, and derive detailed results for spatial variations of the velocity contrast in different sub-sections of the SAF at Parkfield.

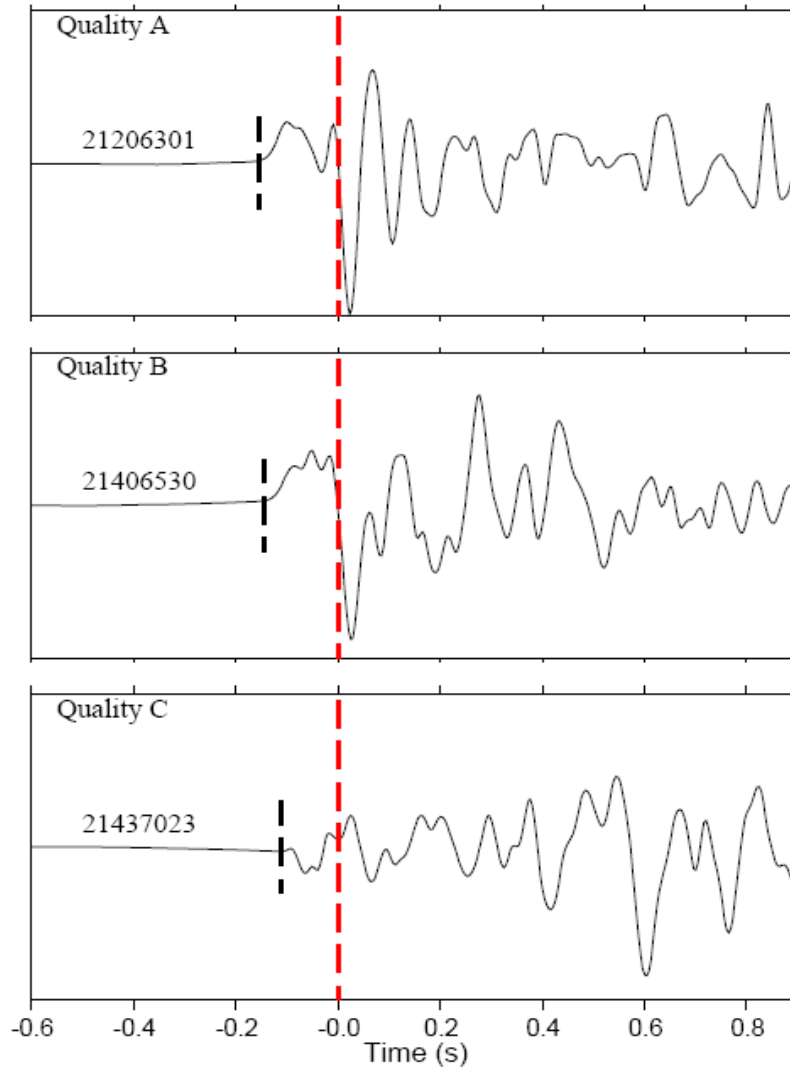


Figure 1.4. Examples of displacement waveforms recorded at station MMNB showing different qualities of the FZHW picks. The red and black vertical dashed lines mark the onsets of direct P waves and FZHW, respectively. The 8-digit numbers denote the CUSP id of the corresponding waveforms.

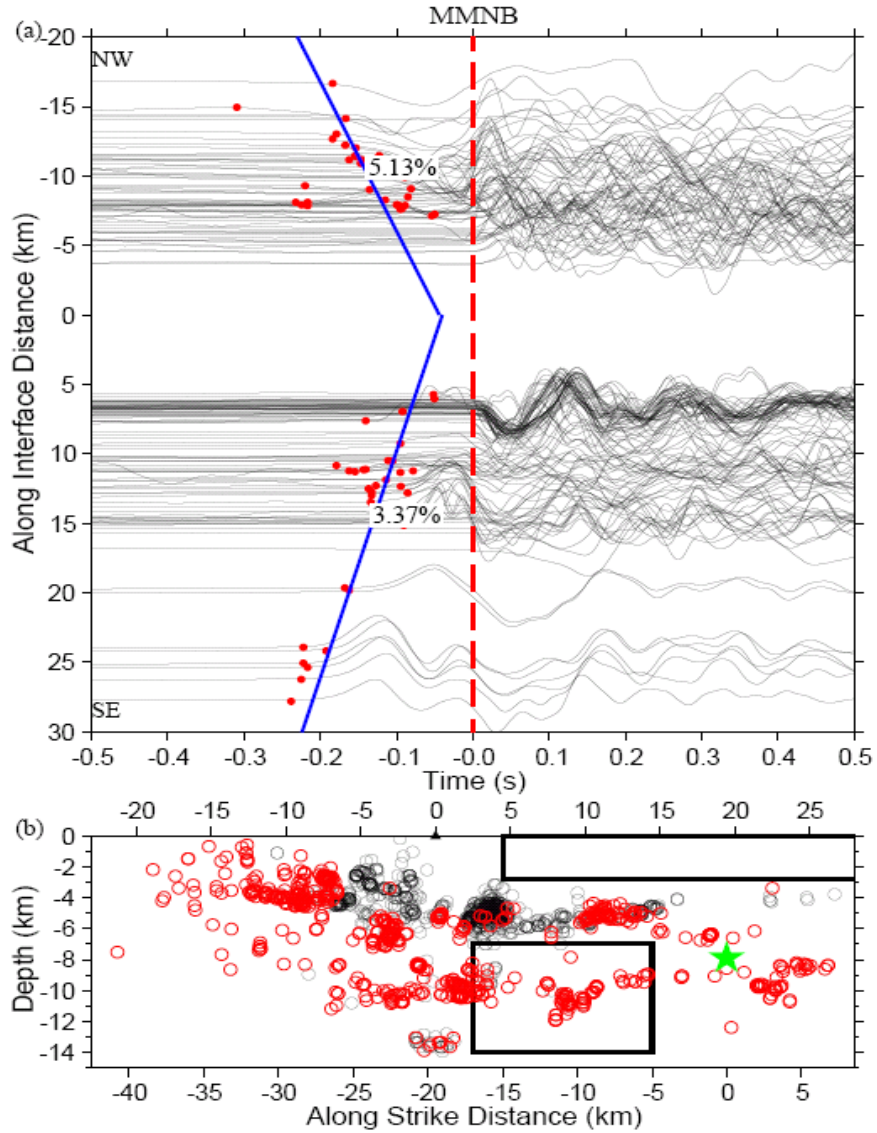


Figure 1.5. (a) Vertical displacement seismograms recorded by the HRSN station MMNB showing the moveout between FZHW and direct P waves along the fault. The red vertical dashed lines mark the onset of the P waves. The red dots mark the onset of FZHW and the blue line shows the least-squares fitting of the moveout. The estimated velocity contrasts using Equation (1.2) and an average P wave velocity of 5.5 km/s are also labeled. The number of plotted waveforms is reduced by 90% from the analyzed data for better illustration. (b) A cross-section view of the seismicity with corresponding waveforms shown in (a) along the 139.2° strike direction. Events with FZHW are marked by red circles. The distances on the top and bottom of the panel are relative to the recording station (black triangle) and the 2004 Parkfield earthquake (the green star) projected along the SAF strike, respectively. The two black rectangles outline the regions with reversed velocity contrast as marked in Figure 1.2c.

1.5 Variations of the Velocity Contrast along the Strike of the SAF

The identification (or absence) of FZHW associated with given source-receiver geometries can be used to infer the existence (or absence) of a sharp velocity contrast across the fault in the study region. For example, station CRAB north of MMNB belongs to the PASO network, and is located within 1 km of the creeping section of the SAF and approximately 3.2 km north of the SAFOD site (Figure 1.1). Clear head waves are observed at this station for events in the NW and SE along-strike directions (Figure 1.6). Using an average P wave velocity of 5.5 km/s, the moveout corresponds to an average velocity contrast of $\sim 7.6\%$ and $\sim 9.9\%$ for the fault sections to the NW and SE of station CRAB, respectively. Similarly, Figure 1.7 shows clear head wave signals recorded at the HRSN borehole station EADB between stations MMNB and GHIB (Figure 1.1). Here, however, the estimated velocity contrasts for sections centered at this station, obtained by the same procedure, are about 5.7% to the NW and only 3.9% to the SE. In addition, the absolute differential arrival times between the FZHW and direct P waves from the NW are considerably larger than those from the SE, indicating a possible change of velocity contrast near EADB.

Figure 1.8 gives a summary of the velocity contrast values that are derived for sections to the NW and SE that are centered at different stations in the study area. Clear head waves are only observed at stations located NE of the fault, indicating that the seismic velocity on the SW side of the fault is overall faster than that on the NE side. As shown in Figure 1.8, however, the results also indicate clear variations of the velocity contrast along the fault. The general pattern is that the velocity contrast reaches its maximum value to the NW of MM (5-10%) and starts decreasing towards the SE. Near

the epicenter of the 2004 Parkfield earthquake (i.e. GH), the estimated velocity contrast is very small (0-2%). Additional results on the velocity contrasts at different depths, and in the opposite along-strike directions around GH, are given in Sections 1.6 and 1.7.

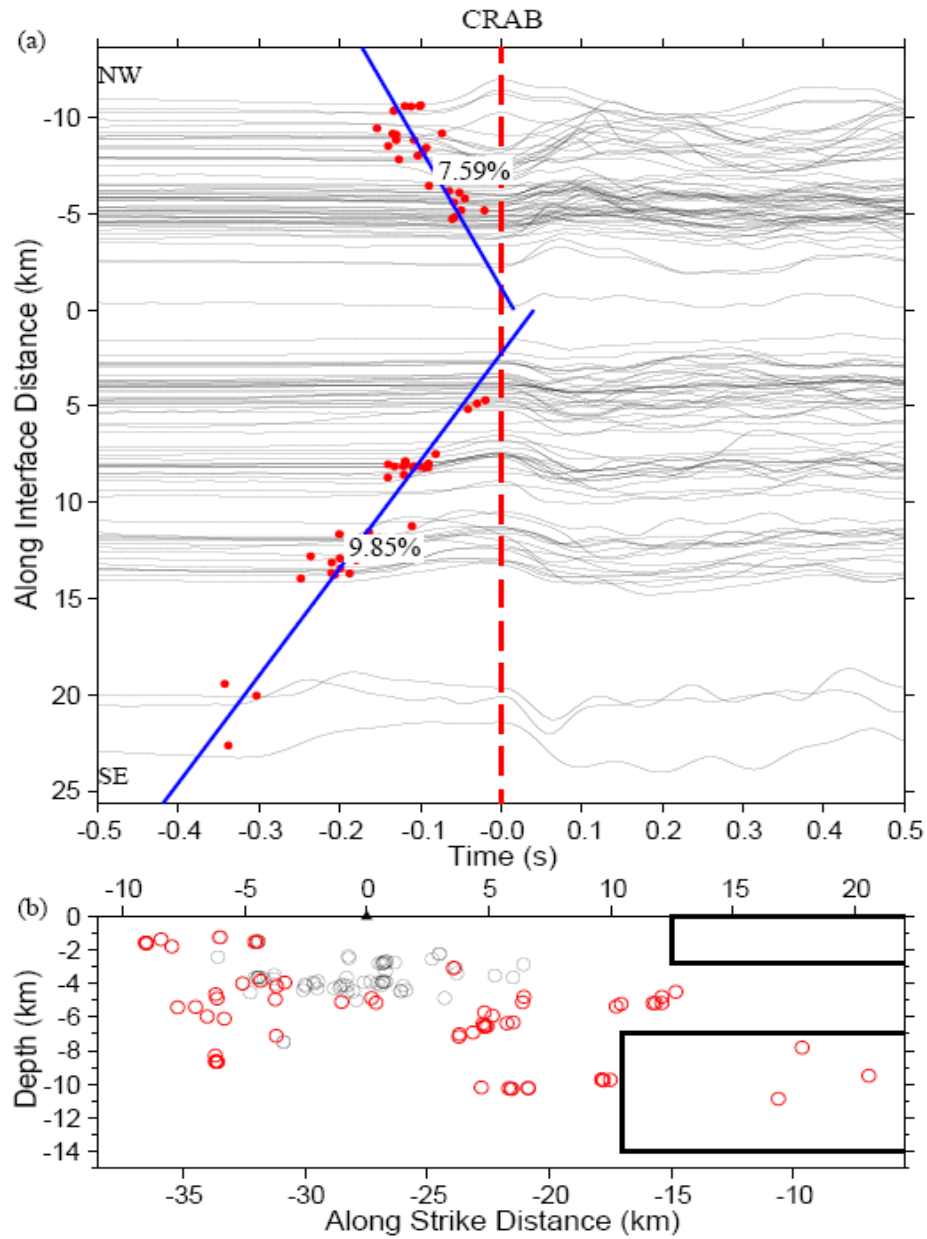


Figure 1.6. Vertical displacement seismograms recorded by the PASO station CRAB showing the moveout between FZHW and direct P waves along the fault. Other symbols are the same as in Figure 1.5.

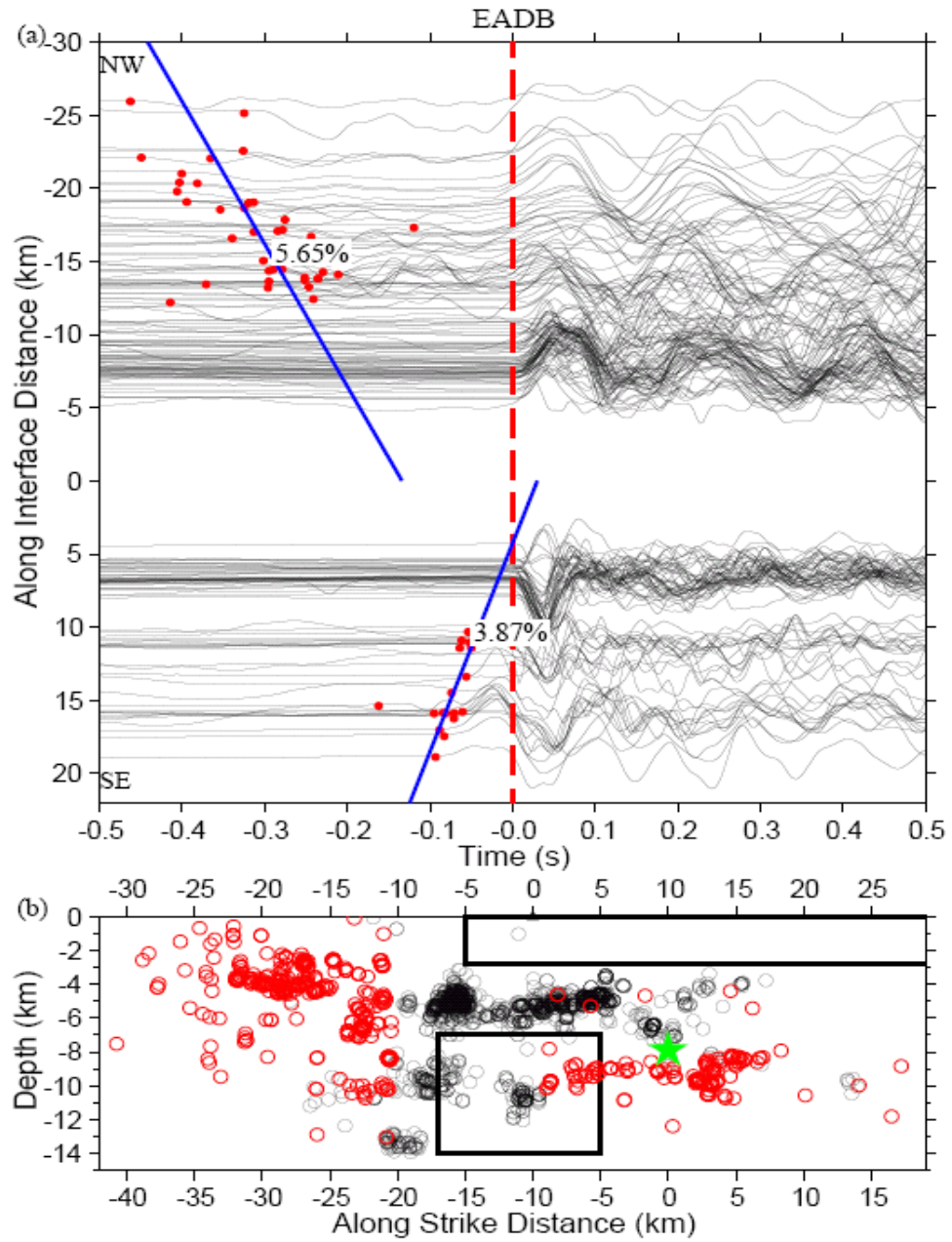


Figure 1.7. Vertical displacement seismograms recorded by the HRSN station EADB showing the moveout between FZHW and direct P waves along the fault. Other symbols are the same as in Figure 1.5. The number of waveforms in (a) is reduced by 90% for better illustration.

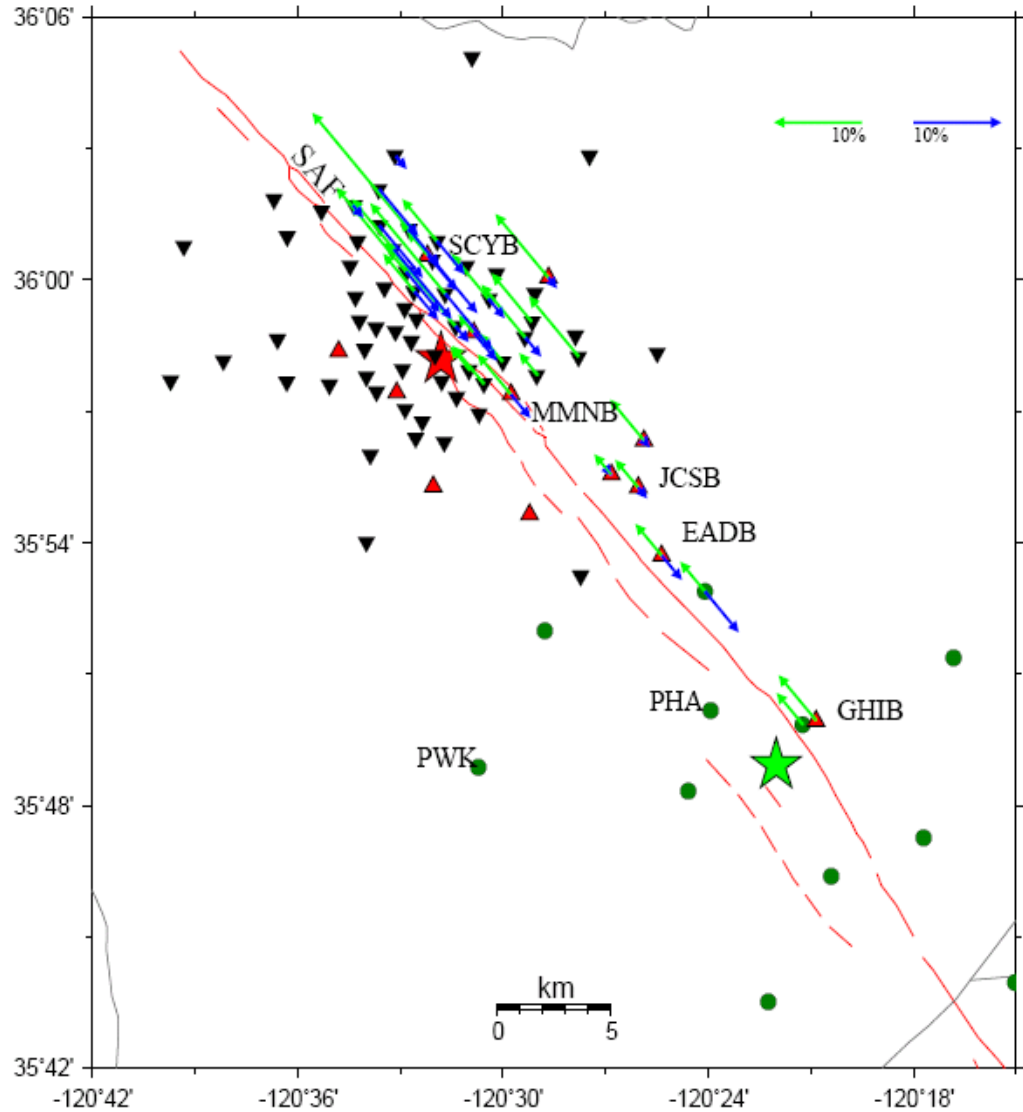


Figure 1.8. A summary of the obtained velocity contrasts across the SAF in the Parkfield area. The green and blue arrows represent, respectively, velocity contrast values for along-strike sections to the NW and SE that are centered at different stations. The length of each arrow is proportional to the percentage of the velocity contrast. Other symbols are the same as in Figure 1.1.

1.6 Variations of the Velocity Contrast with Hypocentral Depth

We observe the existence of velocity contrast across the fault throughout the seismogenic zone, along with changes of the velocity contrast with depth and with different locations along the fault. Figure 1.9a shows a clear moveout of differential

arrival times with increasing depth for events having along-strike distances from station MMNB of less than 2 km. Assuming again that the average P wave velocity is 5.5 km/s, the average velocity contrast for the entire seismogenic zone in that location is $\sim 7.3\%$. This value is compatible with the inference of a deep penetrating fault interface near MM from 3D tomography (Thurber et al. 2006) and previous FZHW studies (Ben-Zion et al. 1992). In contrast, for events directly beneath station GHIB, which is located close to the epicenter of the 2004 M6 event, we can only identify candidate FZHW in several traces (Figure 1.9b). The results imply a lack of a velocity contrast (in which the NE side is the block with slower seismic velocity) over much of the seismogenic zone beneath GHIB.

To obtain additional results on values of the velocity contrasts in the GH region, we plot in Figures 1.10 and 1.11 the moveout of FZHW in waveforms at station GHIB that are generated by earthquakes at different depth sections. We separate the entire dataset into two groups associated with earthquakes above and below 7 km, which is roughly the boundary between two major near-horizontal seismic streaks identified from relocated seismicity (Waldhauser et al. 2004; Thurber et al. 2006). Compared with the results around MM near the epicenters of the 1934 and 1966 M6 events (Figures 1.5 and 1.9a), the pattern of velocity contrast around GH near the epicenter of the 2004 M6 event exhibits a strong along-strike asymmetry. A clear moveout is shown to the NW side of station GHIB for both shallow and deep seismicity, especially for events that are north of MM (at along-strike distance of about -20 km). This is generally consistent with our previous observations that the velocity contrast is strongest north of MM and decreases towards GH (Section 1.5). However, a striking feature of Figures 1.10 and 1.11 is the near absence of FZHW at station GHIB from seismicity to the SE section of the fault.

This is especially pronounced in Figure 1.10, indicating the lack of or very small velocity contrast in the shallow portion of the fault at that section. Even for the seismicity in the deeper part of the fault to the SE of GHIB, head waves can only be observed sparsely from certain locations (Figure 1.11), rather than continuously as shown at the stations to the NW. These results demonstrate clear variations in the strength of the velocity contrast near the epicentral region of the 2004 Parkfield earthquake in both along-strike and down-dip directions.

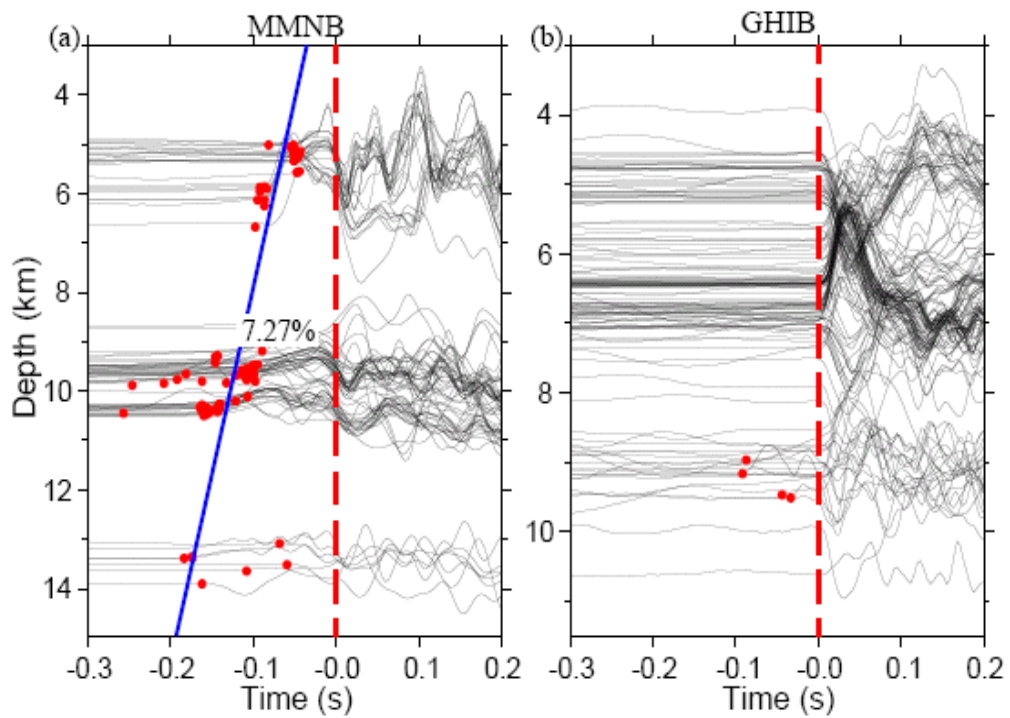


Figure 1.9. (a) Vertical displacement seismograms recorded at the HRSN station MMNB showing the moveout between FZHW and direct P waves with increasing hypocentral depth. The employed events are approximately underneath the station. Other symbols are the same as in Figure 1.5. (b) Vertical displacement seismograms recorded at the HRSN station GHIB for events approximately underneath the station. Other symbols are the same as (a).

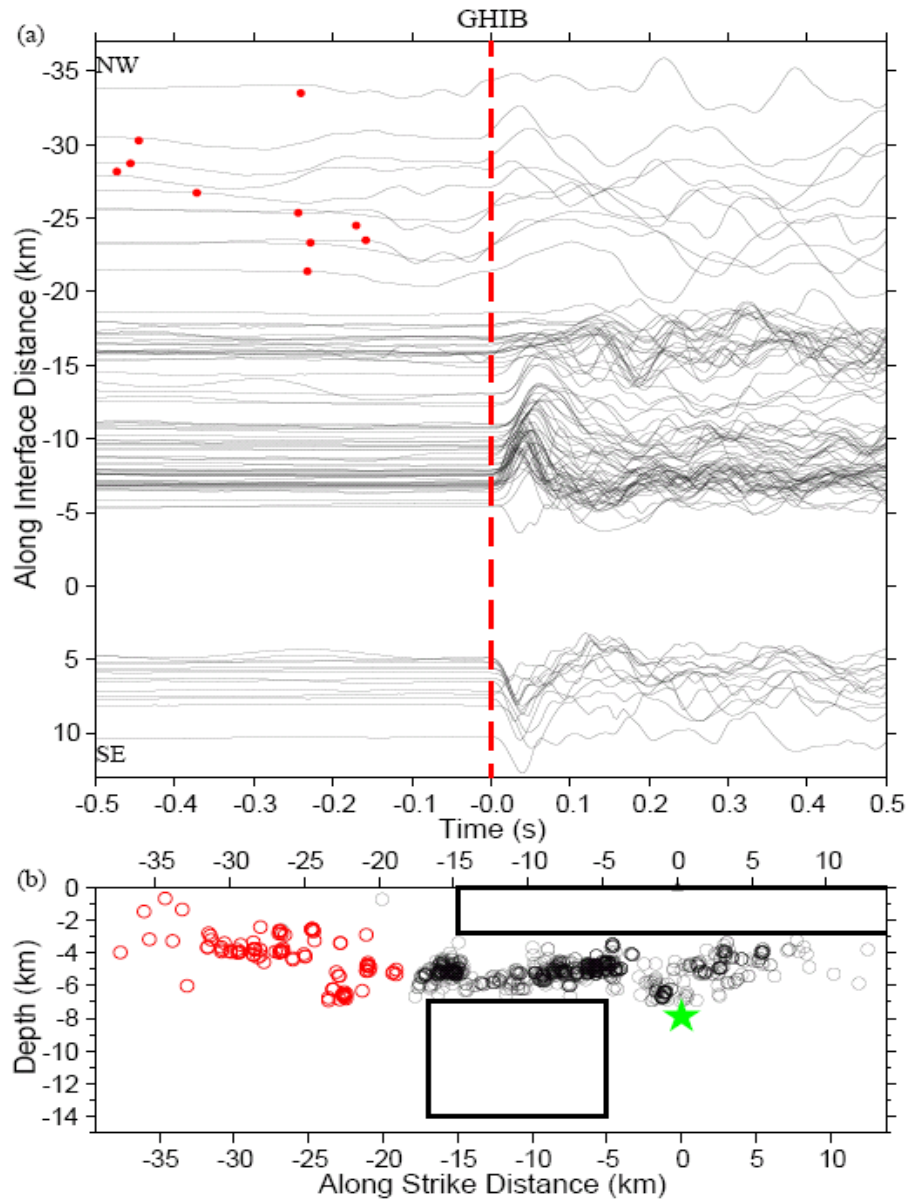


Figure 1.10. Vertical displacement seismograms recorded by the HRSN station Ghib for earthquakes with hypocenter depths less than 7 km. Other symbols are the same as in Figure 1.5. The number of waveforms in (a) is reduced by 75% for better illustration.

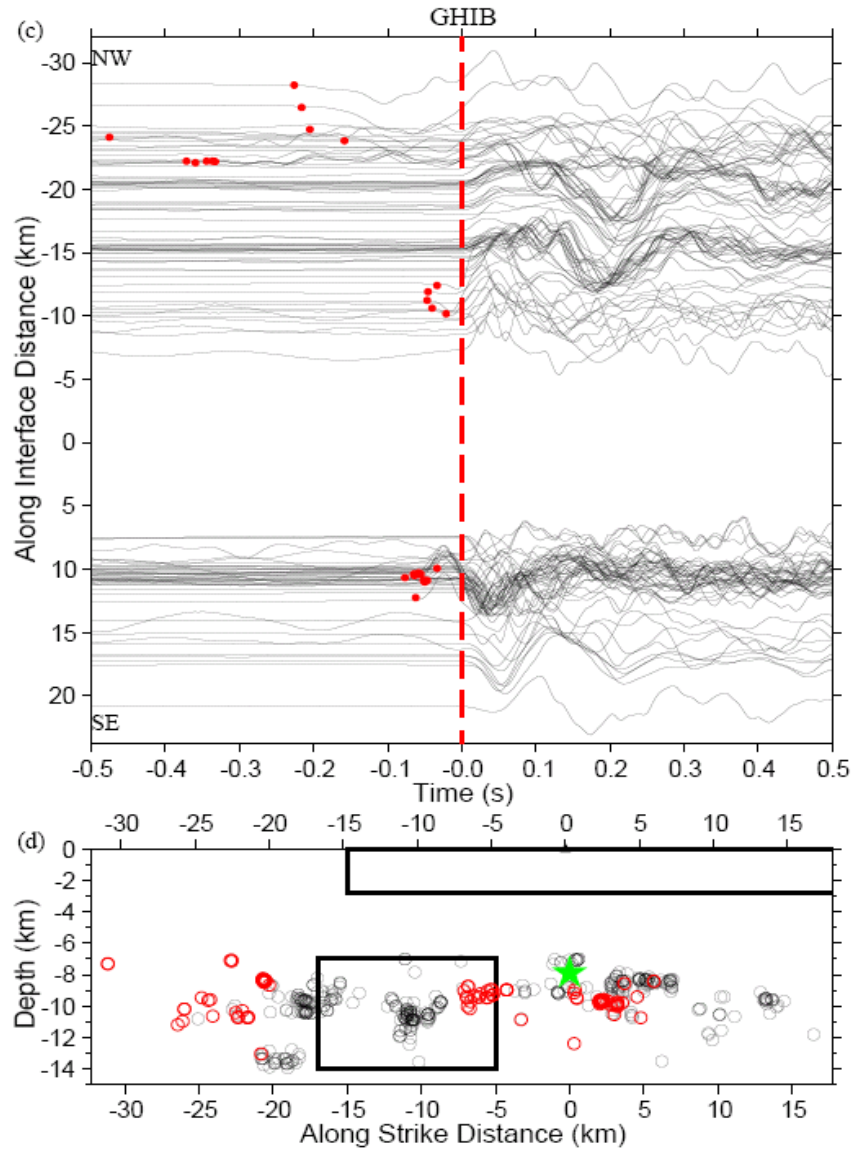


Figure 1.11. Vertical displacement seismograms recorded by the HRSN station GHIB for earthquakes with hypocenter depths larger than 7 km. Other symbols are the same as in Figure 1.5. The number of waveforms in (a) is reduced by 90% for better illustration.

1.7 Possible Reversal of Velocity Contrast between MM and GH

As mentioned in Section 1.2, Eberhart-Phillips and Michael (1993) and Thurber et al. (2006) observed a high P-wave velocity rock on the (nominally slow) NE side of the SAF at seismogenic depth (Figure 1.2). If this high-velocity body is very close to or

directly in contact with the active SAF, as suggested by Thurber et al. (2006), it will produce a locally reversed velocity contrast. This could generate FZHW that will be recorded at stations on the SW side (generally considered as the fast side) that are within the critical distance x_c for a given along-fault propagation distance (Figure 1.3).

To test the possibility of a local reversal of the velocity contrast, we examine waveforms recorded at six NCSN stations on the SW side of the fault near GH (Figure 1.1) for systematic opposite first motion polarities. Figure 1.12 shows records from station PHA, which is the closest station to the fault on the SW side. The first motions generally match the expected polarities of the direct P waves from right-lateral strike-slip focal mechanisms, even for events near the local high velocity region NE of the fault of Thurber et al. (2006). The only exception is one cluster of events at depth around 14 km, which are outside the “suspected” region. However, the abnormal first arrivals from this cluster are unlikely to be associated with FZHW since their focal mechanisms contain a mixture of strike-slip and normal faulting (Figure 1.13). We also observe abnormal first motions from this cluster of events at all six stations on the SW side of the SAF. We conclude that the abnormal first motions from this cluster are probably caused by different focal mechanisms in a region of complex source geometries.

Based on the lack of observation of FZHW at station PHA, we can attempt to estimate the upper-limit value of the possible reversed velocity contrast from the local high velocity region NE of the SAF (Figure 1.2). Using in Equation (1.1) and Figure 1.3, a normal distance of station PHA from the SAF of 2 km and an average propagation distance of 10 km, the corresponding limit for a reversed velocity contrast is 2%. This estimate assumes that the seismicity is located on the interface between the high velocity

body of Figure 1.2 and the main SAF. However, the seismicity is clearly offset from the SAF and occurs essentially under the SWFZ. This limits our ability to constrain the maximum allowable value of a sharp reversed velocity contrast of the localized high velocity body NE of the SAF that is imaged by Eberhart-Phillips and Michael (1993) and Thurber et al. 2006).

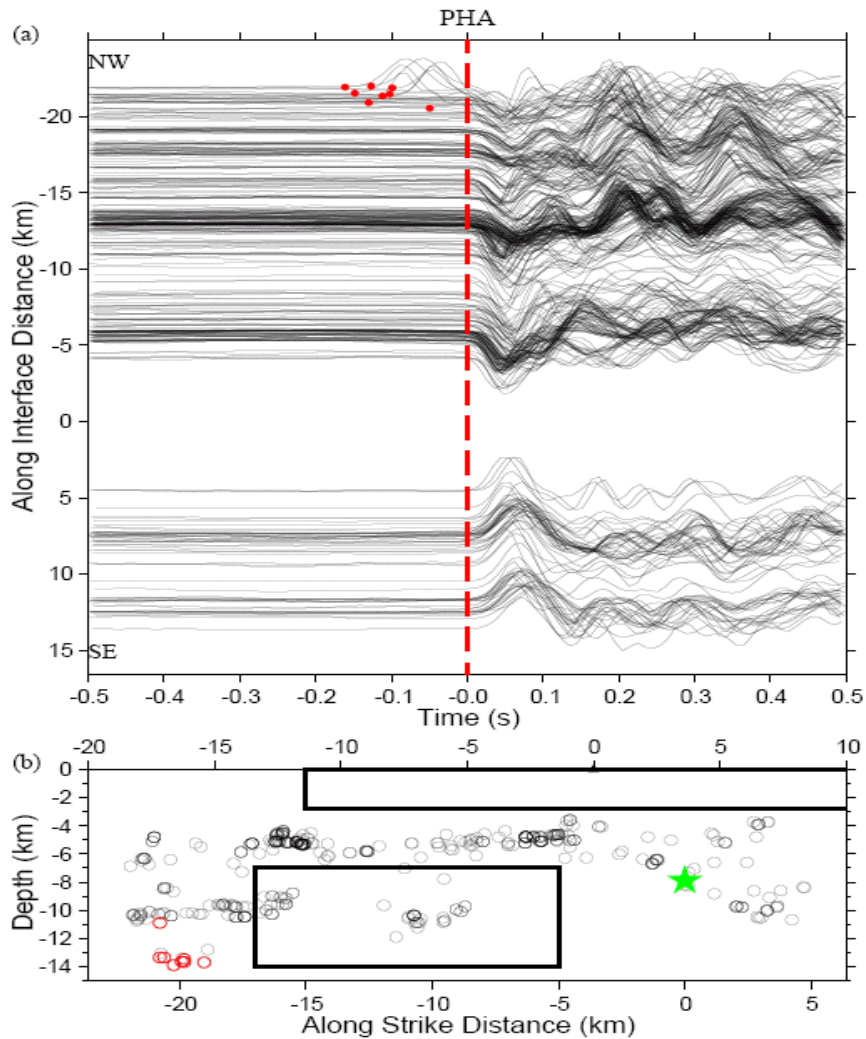


Figure 1.12. (a) Vertical displacement seismograms recorded at the HRSN station PHA located SW of the fault. Waveforms with first motions opposite to the polarities predicted from right-lateral focal mechanisms are marked by red dots. (b) The seismicity with corresponding waveforms shown in (a) along the 139.2° strike. Events with abnormal first motions in (a) are shown with red circles. Other symbols are the same as Figure 1.5.

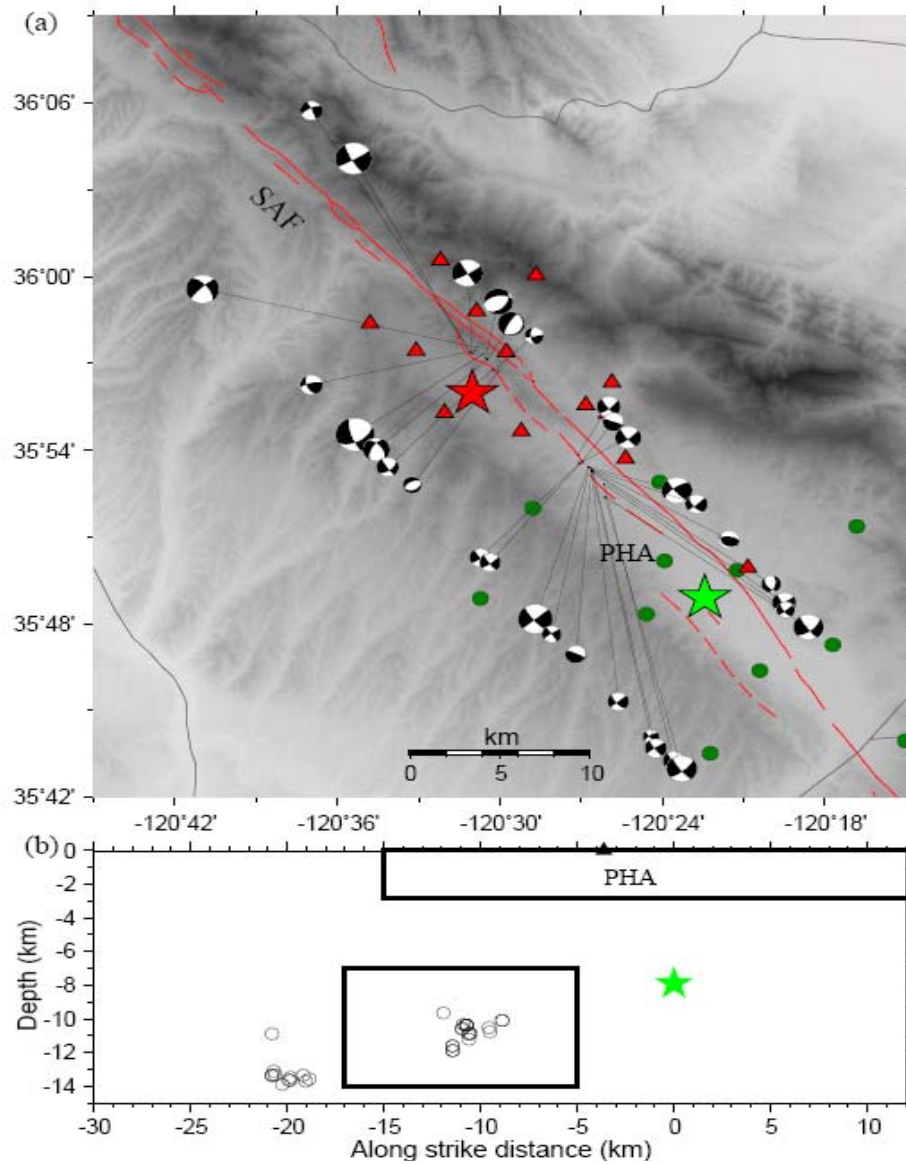


Figure 1.13. Focal mechanism solutions of selected events from the "suspected" region with reversed velocity contrast and the events marked in Figure 1.12 with red circles. Other symbols are the same as Figure 1.5. The focal mechanism solutions are obtained from the Northern California Earthquake Data Center.

1.8 Discussion

We conducted a comprehensive imaging of the existence and average properties of sharp velocity contrast interfaces along the Parkfield section of the SAF using FZHW and direct P waves. Clear FZHW are observed only for stations on the NE side of the

fault, indicating that the crustal block to the SW of the fault has generally higher seismic velocity than the block to the NE. In addition, we found clear along-strike variations of the velocity contrast along the SAF (Figure 1.8). In the NW part of our study region, and around MM near the epicenters of the 1934 and 1966 M6 events, the velocity contrast is fairly strong (5-10%) and the bimaterial interface extends to the bottom of seismogenic zone (Figures 1.5, 1.9a). On the other hand, around GH near the epicenter of the 2004 M6 Parkfield earthquake the velocity contrast is either absent or very small (0-2%), especially in the top 7 km and in the region to the SE of GH (Figures 1.9b, 1.10, and 1.11).

Our results are generally consistent with the regional geological setting that the Salinian granite on the SW side of the fault has a faster seismic velocity than the Franciscan rock and Great Valley sequence on the NE side. Previous local tomography results also show that the SAF around Parkfield has a clear velocity contrast that varies along the SAF strike (e.g. Figure 1.2c and Figure 1.6 in Eberhart-Phillips and Michael 1993). We note that the velocity contrasts around MM obtained from previous tomographic results (e.g., Thurber et al. 2006) are on the order of 10-30%, which is larger than the range of 5-10% inferred from this study. The difference may be related to the fact that the tomographic images involve rock volumes that extend some distance away from the fault, and may hence be influenced by off-fault structures, while the imaging based on FZHW apply more strictly to the fault interface itself. It is also possible that the along-strike spatial averaging of FZHW as they propagate through regions with different velocity contrasts may reduce the obtained contrast values. The third possibility could be due to the fact that the existing damage zone along the fault interface (e.g., Li et al., 2006)

might reduce the value of velocity contrast. However, this explanation has to be justified by the depth extent of damage zone (e.g., Chapter 3). If the depth extent of damage zone is above the active seismogenic zone as suggested from some studies (Ben-Zion et al., 2003), it might not affected the estimated velocity contrast.

The geological observation of mafic igneous rocks (Figure 1.14), local seismic tomography results (Figure 1.2), and local gravity map (Figure 1.15) all indicate the existence of high-velocity rocks on the NE side of the fault near GH (Eberhart-Phillips and Michael 1993; McPhee et al. 2004; Thurber et al. 2006). Some of these studies suggest that the seismic velocity of these rocks on the NE side may exceed that of the predominantly faster rock to the SW of the fault (Figure 1.2c), producing a locally reversed velocity contrast across the SAF. Unfortunately, the locations of the seismicity and stations on the SW side of the fault limit our ability to confirm the existence of a sharp reversed velocity contrast across the SAF in that area. We may infer that the high-velocity rock on the NE side of the SAF near GH probably does not touch the SWFZ, which is outlined by the active seismicity, at seismogenic depth, and the rocks adjacent to SWFZ on both sides probably have the same seismic velocities in that region.

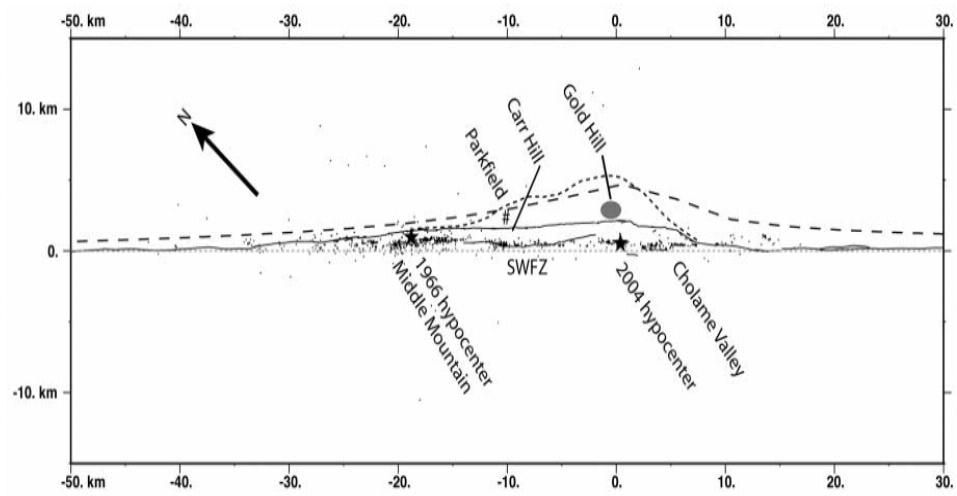


Figure 1.14. Location of high-velocity mafic igneous rocks exposed on the northeast side of SAF near Gold Hill is marked as a gray ellipse near the epicenter of the 2004 M6 Parkfield event (from Simpson et al. 2006).

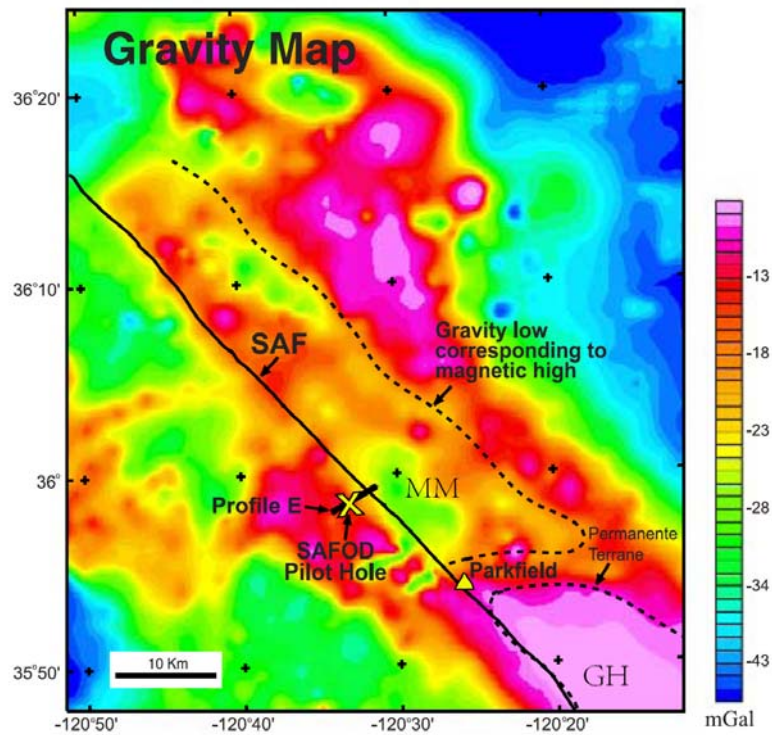


Figure 1.15. Regional Isostatic gravity map near Parkfield with MM (Middle Mountain) and GH (Gold Hill). Modified from McPhee et al. (2004).

The along-strike variations of the velocity contrast observed in this study are consistent with geological and geophysical results on the evolution of the SAF in this region. Detailed geological studies have found mafic igneous rocks exposed at GH on the NE side of the main SAF surface trace, which may correspond to the high-velocity body imaged by previous tomography studies (e.g. Eberhart-Phillips and Michael 1993; Thurber et al. 2006). These rocks have similar characteristics to those exposed at the Eagle Rest Peak about 150 km to the SE, and hence were likely transported to GH (e.g. Sims 1993) by the movement of the Pacific plate. Simpson et al. (2006) suggested that the presence of these rocks on the “wrong” side of the SAF is consistent with progressive northeastward bending of the SAF and development of a new fault interface (e.g. SWFZ) with time around Parkfield. This could move rocks that were previously on the SW (i.e. overall faster) side of the fault to the NE side of the “new” fault interface. Because the largest warp of the fault traces is near GH (Figure 2 of Simpson et al. 2006), we should expect that the fault interface near GH has a smaller velocity contrast than that near MM. This is supported by our observations. The multiple shifts of the active traces of the SAF near GH (Dibblee et al. 1999) could also offset the newly-developing active fault in that area (SWFZ) away from a sharp bimaterial interface. The high-velocity rock on the NE side of the main SAF near GH appears to be seismically inactive at present (e.g. Simpson et al. 2006; Thurber et al. 2006).

Our observations of clear along-strike variations of the velocity contrast along the SAF offer, along with the above discussion, an explanation for the mixed propagation directions of the M6-type Parkfield earthquakes (Harris and Day 2005; Ben-Zion 2006). Since the velocity contrast around MM is large and positive (with the SW side being fast

and the NE side being slow), the preferred propagation direction for earthquakes nucleating in that region is to the SE. The 1934 and 1966 events had hypocenters around the MM region, and were associated with propagation directions to the SE, which is consistent with the preferred rupture direction generated by the bimaterial effects (e.g. Weertman 1980; Shi and Ben-Zion 2006; Ampuero and Ben-Zion 2008). The 2004 M6 earthquake nucleated near GH with a near-zero velocity contrast in the active seismic fault (i.e., the SWFZ) and perhaps a reversed contrast across the main SAF (e.g. Thurber et al. 2006). Thus, in contrast to the region further to the north, the region around the hypocenter of the 2004 event is not expected to produce a preferred propagation direction to the SE. Instead, the discussed local structural complexities would probably dominate the nucleation and propagation of earthquake ruptures near GH.

Our results on the reduction in the strength of the velocity contrast across the SAF near GH also provide a dynamic arrest mechanism for the M6 Parkfield events. This is because the amplitude of the dynamic changes of normal stress along a bimaterial interface increases (e.g. Ben-Zion and Andrews 1998; Ranjith and Rice 2001; Ben-Zion and Huang 2002) with increasing degree of the velocity contrast (at least up to about 30-40% contrast of S wave velocities). Thus, earthquakes that nucleate near MM will encounter during their propagation to the SE increasing frictional strength, due to the diminishing dynamic bimaterial reduction of normal stress associated with the decreasing velocity contrast in the SE section. Similarly, earthquakes that nucleate near GH will encounter with continuing propagation to the NW increasing frictional strength, due to the growing dynamic increase of normal stress at the rupture tip produced by the increasingly pronounced velocity contrast (with slower NE side) in the NW section.

Additional details on the differences between the velocity contrasts across the SAF in the MM and GH regions can be obtained by performing a joint inversion of FZHW and direct P waves for dissimilar layered velocity structures on the opposite sides of the fault in these locations (Ben-Zion et al. 1992; Lewis et al. 2007). This is left for a future work.

CHAPTER 2

VELOCITY CONTRAST ALONG THE CALAVERAS FAULT FROM ANALYSIS OF FAULT ZONE HEAD WAVES GENERATED BY REPEATING EARTHQUAKES

Summary

The work in this chapter is published in Zhao and Peng (2008). We systematically investigate the velocity contrast along the Calaveras fault that ruptured during the 1984 Morgan Hill earthquake using fault zone head waves (FZHW) that refract along the fault interface. We stack waveforms in 353 sets of repeating clusters, and align the peaks or troughs of the direct P waves assuming right-lateral strike-slip focal mechanisms. The obtained velocity contrasts are 2–3% and 12–14% NW and SE of station CCO, respectively. The FZHW and the fault plane outlined by the relocated seismicity SE of CCO are more complicated than those NW of CCO. The results can be explained by a relatively simple and sharp fault interface in the NW, and a complicated fault structure with a presence of a low-velocity zone in the SE. The along-strike variations in the strength of the velocity contrast are consistent with surface geological mapping and recent 3D tomography studies in this region.

2.1 Introduction

As was described in the previous chapter, differential elastic properties are common across faults, resulting in well-defined biomaterial interfaces. An accurate determination of the fault interface properties at seismogenic depth can be important for

various aspects of earthquakes and fault dynamics (e.g., Ben-Zion 2001), and better quantification of earthquake locations and focal mechanisms (e.g., Hardebeck et al. 2007). In this work, we show clear evidence of FZHW along the central portion of the Calaveras fault that ruptured during the 1984 M6.2 Morgan Hill earthquake (Figure 2.1), and use them to quantify the along-strike variations of the fault interface properties. This section of the fault juxtaposes the Franciscan complex (fast) in the NE side and a sequence of marine sediments (slow) in the SW side deposited mostly during the Cretaceous (Page 1984). Franciscan complex rock is a subduction zone complex consisting of a melange of marine sedimentary rocks and ultramafic bodies. These ultramafic bodies include serpentinite blocks of the Coast Range Ophiolite (Graymer et al., 1995; Manaker et al., 2005). Seismic tomography studies in this region have found 6–14% of P-wave velocity contrast that extends to at least 5 km depth (Michael 1988; Thurber et al. 2007), consistent with the geological observations.

More than 40% of the recorded seismicity in the aftershock zone of the Morgan Hill mainshock belongs to repeating earthquakes (Peng et al. 2005). Since repeating earthquakes rupture almost the same fault patch, they generate nearly identical waveforms. We take advantage of the abundant repeating earthquakes in the study region, and stack waveforms in each repeating cluster to enhance the signal-noise ratio (SNR) and the confidence levels of the FZHW identification. In the next section, we briefly describe the method to identify repeating clusters. In section 2.3, we present the detailed procedures of stacking and aligning waveforms. The results are shown in Section 2.4 and are discussed in Section 2.5.

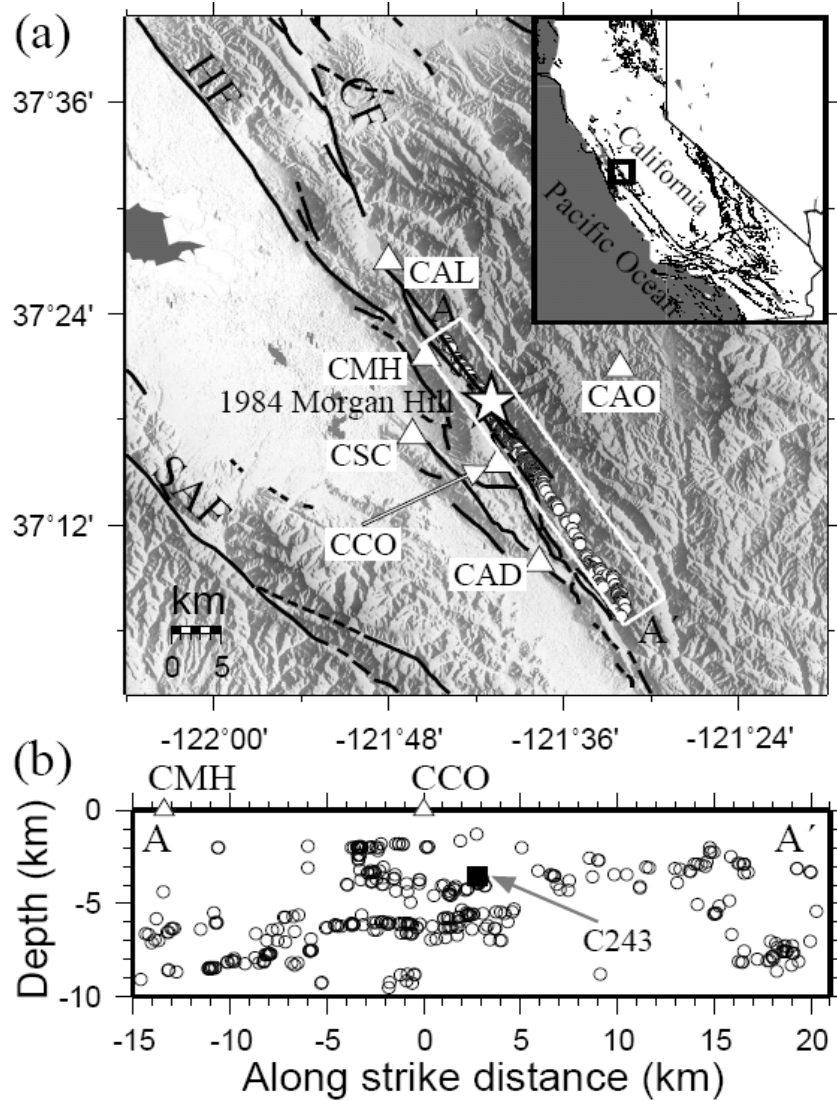


Figure 2.1. (a) Location of the central section of the Calaveras fault in California. Dark lines denote nearby faults. The circles denote the 353 repeating clusters employed in this study. The star marks the epicentral location of the 1984 Morgan Hill mainshock. Triangles denote six stations in the NCSN. Shaded background indicates topography with white being low and dark being high. The inset shows the map of California with the box corresponding to the study area. SAF, San Andreas fault; CF, Calaveras fault; HF, Hayward fault. (b) The centroid locations of 353 repeating clusters in the cross-section map along the Calaveras fault (1460 strike). Waveforms generated by events in cluster C243 (the sold black square) are shown in Figure 2.2.

2.2 Repeating Earthquake Identification

We identify repeating clusters in the study region using 7857 earthquakes relocated by Schaff et al. (2002). The detailed procedure is as follows. We first compute the inter-event distances for all earthquake pairs along and perpendicular to the fault strike of 146° . The source radius of each event is estimated from its catalog magnitude, based on a moment-magnitude relationship (Abercrombie 1996) and a circular crack model (Eshelby 1957) with a nominal 3-MPa stress drop. Two events are considered as a pair if their inter-event distance along the fault strike is less than the source radius of the larger event. Next, we organize the event pairs into clusters using the equivalency class (EC) algorithm (Press et al., 1986). We do not include those events with inter-event distances perpendicular to the fault strike larger than the source radius. Using the above criteria, we identify a total of 353 repeating clusters, with at least five events in each cluster.

We note that the number of identified repeating clusters depends on the assumed model parameters (e.g., the constant stress drop value and the circular crack model) and other selection criteria. However, since our main goal of using repeating clusters is to stack waveforms that are highly similar to enhance the SNR and confidence levels of FZHW identification, using slightly different parameters will not change the overall features of the waveform stacks and our main conclusions.

2.3 Waveform Stacking and Alignment

This study employs seismic data recorded by surface stations in the Northern California Seismic Network (NCSN). Each station has a high-gain, short-period, vertical-component sensor, and records at 100 samples/s. The FZHW are the first arriving phases

at locations on the slower block with normal distance to the fault (Ben-Zion 1989) less than a critical distance x_c given by Equation (1.1). Using a nominal distance r of 10 km, and an average velocity contrast of 10% from previous tomography studies (Michael 1988; Thurber et al. 2007), the critical distance x_c is about 5 km. For the six NCSN stations that are within 15 km of the Calaveras fault (Figure 2.1), only stations CCO and CMH are within the critical distances on the slow side (SW) of the fault to record FZHW as the first arriving phases.

Prior to the analysis, we remove the mean and trend of each trace, and apply a zero-phase high-pass filter with a corner at 1 Hz to suppress long-period noise. Next, we select a reference trace that has the highest similarity with others in each repeating cluster, and remove those traces with cross-correlation coefficient to the reference smaller than 0.8, or the SNR smaller than 2. We then normalize the amplitude of each trace by its maximum value, and linearly sum all the traces after aligning with the reference trace to obtain a single stack in each cluster (Figure 2.2).

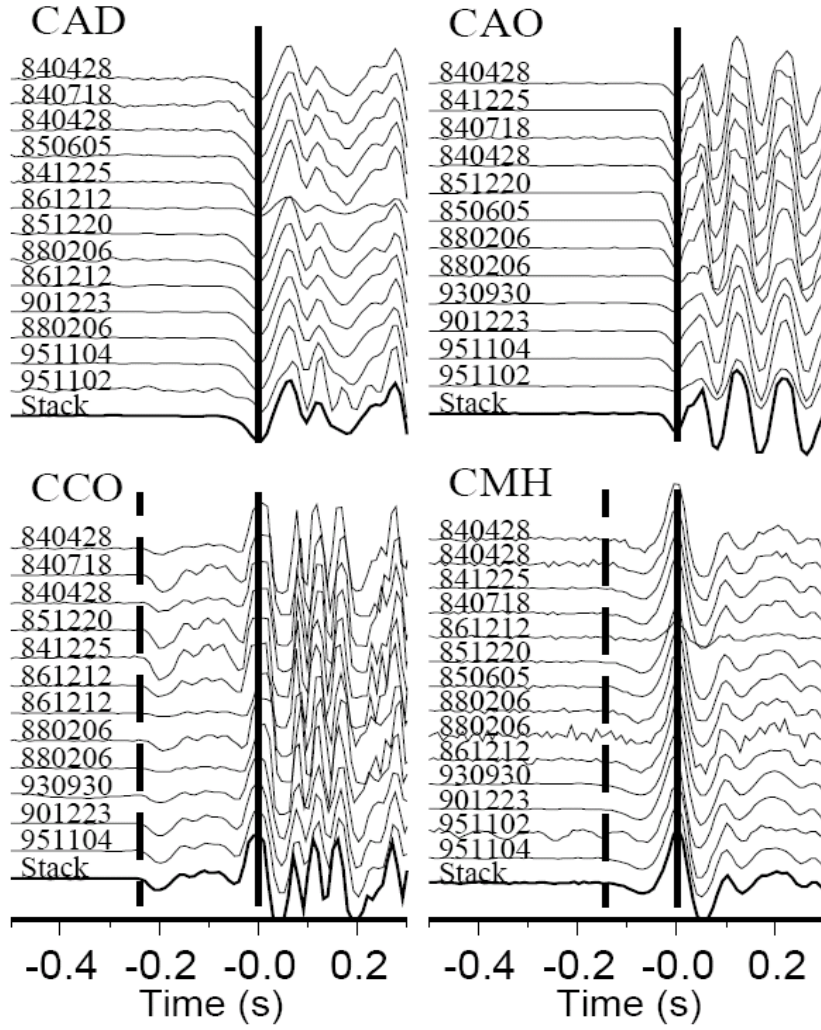


Figure 2.2. Vertical-component seismograms around the P arrivals generated by events in cluster C243 and recorded by four stations. The dashed and solid vertical lines mark the arrivals of FZHW and direct P waves, respectively. The bottom trace (thick line) is a simple stack of normalized individual traces at each station by aligning with the P waves. The occurrence time of each event (2 digit year, month and day) is shown on the left of each trace.

Next, we align the peaks or troughs of the stacked direct P waves (Figure 2.3), assuming right-lateral fault mechanisms for all clusters. This is justified by the fact that the majority of the microseismicity in the Morgan Hill rupture zone have strike-slip focal mechanisms on near-vertical planes (Michael 1988; Schaff et al. 2002). We also use the

first motion polarity from other NCSN stations to confirm the radiation patterns. After aligning the P waves, we manually pick the arrival times of the FZHW by comparing with the waveform stacks of nearby clusters.

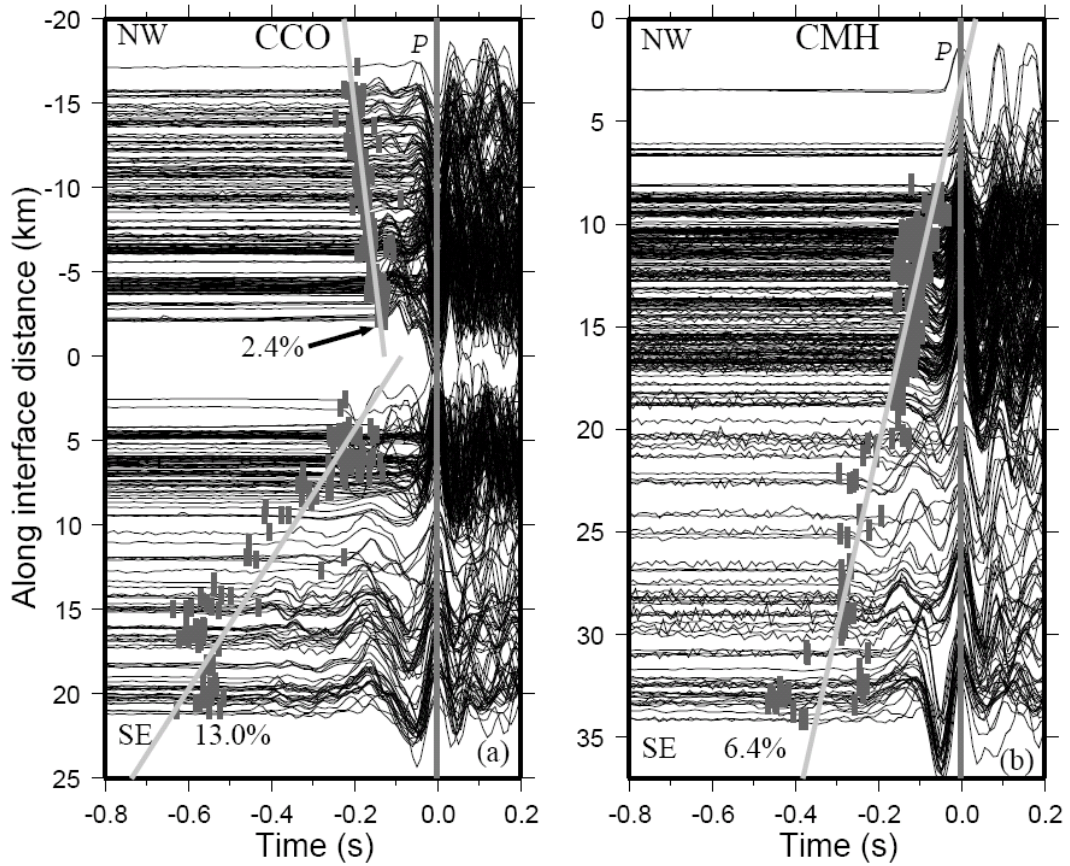


Figure 2.3. (a) Stacked traces at station CCO showing the moveout of the FZHW. The vertical-axis is the along fault-interface distance between the centroid location of each cluster and station CCO along the Calaveras fault (146° strike). The P arrivals are aligned with their peaks or troughs depending on the relative locations of clusters to station CCO, assuming right-lateral strike-slip focal mechanisms. Short vertical bars mark the fault zone head wave arrivals. The gray lines mark the slope of moveout by the least-squares fitting of the head wave picks. The corresponding velocity contrasts with an average P wave velocity of 5 km/s are marked. (b) Stacked traces at station CMH showing the moveout of the head waves. All symbols are the same as (a).

After picking of the FZHW phases, we obtain a total of 308 (2181 events) and 312 (2126 events) stacked traces for stations CCO and CMH, respectively. We dropped

45 traces for station CCO, and 41 traces for station CMH, because the data are severely clipped, or the stations are outside the critical distances x_c for some nearby events. We also checked the waveforms and found no clear FZHW recorded at other four stations, CAO, CAL, CAD, and CSC, since they are either on the fast side (SE), or beyond the critical distance to record FZHW as first arrivals.

2.4 Variations of Velocity Contrast Along Strike and Depth

The stacked waveforms and FZHW arrivals are shown in Figure 2.3 for stations CCO and CMH. Clear head waves are recorded at both stations with motion polarities opposite to those of the direct P waves. The time difference (Δt) between the FZHW and the direct P waves, or moveout, increases with distance along the fault interface r , indicating the existence of a sharp velocity contrast in this region. We find that the FZHW moveout SE of station CCO has a larger slope than that to the NW, suggesting a possible change of velocity contrast along the fault strike. In addition, the moveout to the NW follows a linear trend, and the head wave signals are relatively simple. In comparison, the moveout to the SE is more scattered, and the head wave signals are more complicated. The moveout and head wave signals at station CMH also show similar changes at a distance of ~ 20 km (near station CCO), consistent with the patterns observed at CCO.

The P wave velocity contrast $\Delta\alpha$ can be estimated from the slope of the differential arrival time Δt and the along-interface distance r as Equation (1.2). Assuming $\alpha = 5$ km/s based on the average velocity model used in Schaff et al. (2002), we obtain from least-squares fitting average velocity contrast $\Delta\alpha/\alpha$ to the NW and SE of CCO of

2.4±0.1% and 13.0±0.5%, respectively. The $\Delta\alpha/\alpha$ value is 5.6±0.2% for station CMH. If we separate the data for CMH for $r \leq 20$ km and $r > 20$ km, the obtained $\Delta\alpha/\alpha$ are 3.3±0.2% and 6.3±0.9%, respectively.

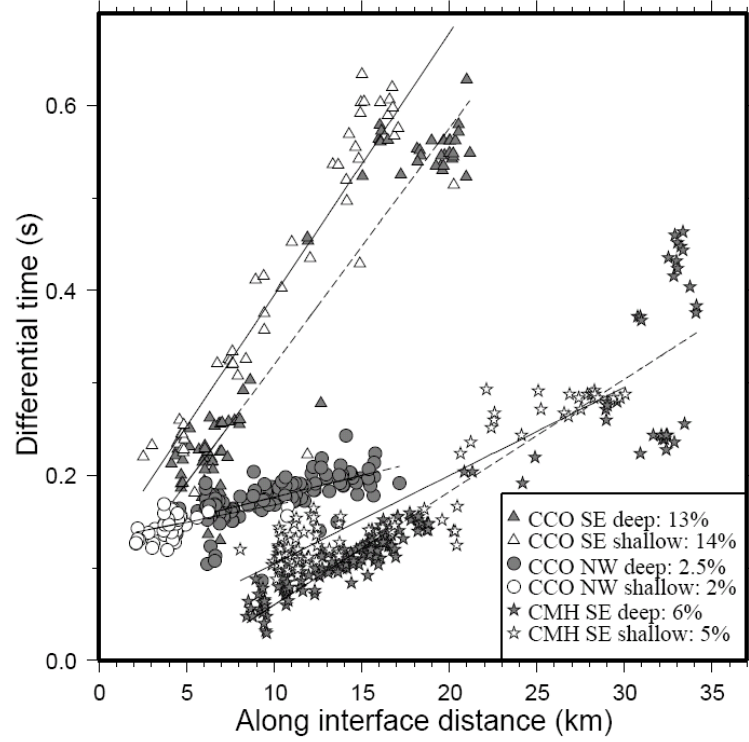


Figure 2.4. Differential arrival times between FZHW and direct P waves versus the along fault-interface distances for stations CCO and CMH. The data points are divided into shallow (depth ≤ 4 km) and deep (depth > 4 km) groups. The solid and dashed lines are least-squares fittings for shallow and deep groups, respectively. The velocity contrasts for different groups are shown on the bottom right.

To quantify the depth dependence of the velocity contrasts, we divide the clusters according to their average hypocentral depths as shallow (depth ≤ 4 km) and deep (depth > 4 km) groups, and fit the data points in each group separately (Figure 2.4). The obtained $\Delta\alpha/\alpha$ for the shallow and deep groups NW of CCO are relatively small and similar. The velocity contrast for shallow clusters SE of CCO is slightly larger than that for the deep clusters, while the pattern is the opposite for station CMH. However, the

difference is probably not significant due the relatively large fitting errors. The obtained $\Delta\alpha/\alpha$ for station CMH is between the average $\Delta\alpha/\alpha$ values NE and SW of station CCO. In summary, there is some depth dependence of velocity contrast, with slightly larger values in the shallower crust (depth ≤ 4 km) for station CCO. But the dominant variations of the imaged velocity contrasts are along-strike.

2.5 Discussion

The existence of the FZHW indicates a sharp material interface along the Calaveras fault. The time difference Δt between the FZHW and the direct P waves can be used to document the along-strike and down-dip variations of the strength of the material contrast. Our results are summarized in Figure 2.5 in map and cross-section views. The velocity contrast NW of station CCO is $\sim 2\text{-}3\%$, and the head wave signals are relatively simple. This is consistent with a well-defined fault structure outlined by the microseismicity (Schaff et al. 2002), indicating a simple and sharp fault interface that extends to the bottom of the seismogenic depth in that segment. In comparison, the velocity contrast SE of station CCO is $\sim 12\text{-}14\%$, and the head wave signals are complicated with many phases between the FZHW and the direct P waves. The existence of such complicated FZ phases suggests a thick transition zone between the two sides of the fault (McGuire and Ben-Zion 2005). In addition, the seismicity in the SE is relatively diffuse, and the surface expression of the Calaveras fault does not coincide with the fault interface inferred from the earthquake locations (Michael 1988; Schaff et al. 2002). These evidence suggest the existence of a low-velocity zone SE of station CCO that extends to the depth of a few kilometers in the SW (slow) side of the fault.

The obtained variations in the strength of the velocity contrasts along the Calaveras fault using FZHW are consistent with surface geology and recent 3D tomography studies in this region. A surface geological map shows an apparent change of rock types along the Calaveras fault near station CCO (Page 1984). The surface trace cuts through the Franciscan Complex NE of CCO, resulting in a well-defined fault interface and a small velocity contrast. In comparison, the fault SE of CCO juxtaposes a low-velocity marine sedimentary rock in the SW side and the faster Franciscan Complex in the NE side. Several 3D tomography studies also indicate an apparent low-velocity body south of CCO, down to a depth of ~5 km (Michael 1988; Thurber et al. 2007). This low-velocity body is also inferred from the head wave analysis in this study, and is likely corresponding to the surface expression of the sedimentary layer in the SW side of the Calaveras fault.

A detailed 3D high-resolution image of the FZ properties in this region can be obtained by traveltimes inversions and waveform modeling of the FZHW and direct P waves (e.g., McGuire and Ben-Zion 2005; Lewis et al. 2007). This will be pursued in a follow up study. Our results demonstrate that stacking waveforms generated by repeating clusters provides an effective tool for increasing the SNR and confidence levels of FZHW identification, while reducing the total numbers of analyzed waveforms from several thousands to a manageable number of several hundreds. The sensitivity of FZHW to the changes of bimaterial interface properties along the fault strike indicates that head waves provide a high-resolution tool for imaging fault zone properties at seismogenic depth.

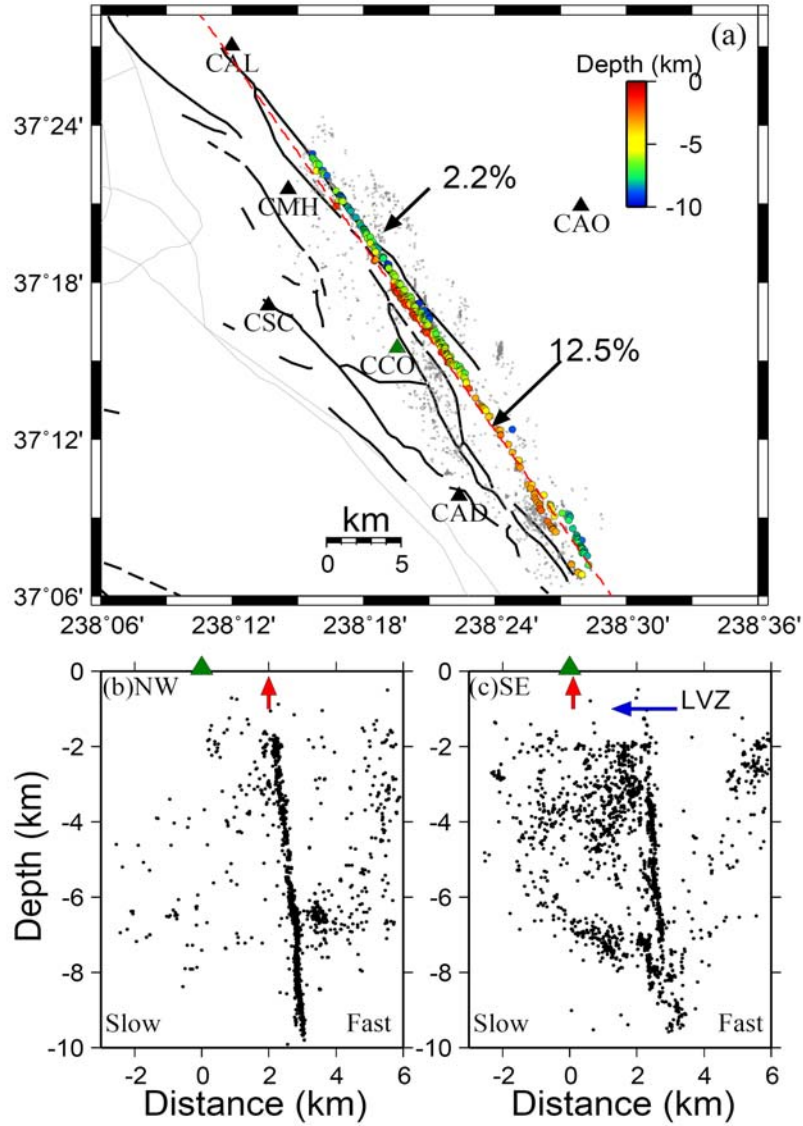


Figure 2.5. Schematic summary of the results from the traveltime analysis of FZHW at stations CCO and CMH. (a) Map view of the Calaveras fault (CF) with the entire relocated seismicity by color dots with color denoting different depth ranges from Schaff et al. (2002) and the 353 repeating clusters employed in this study (solid black circles). The estimated velocity contrasts in the NW and SE sections are labeled with the arrows. Dark lines denote nearby faults. (b) Cross-section view perpendicular to the strike of the fault (146°) with projection of the all earthquakes (black dots) NW of station CCO. The green triangle and red arrow mark the projected locations of CCO and the surface trace of the Calaveras fault. (c) Cross-section view for all earthquakes SE of station CCO. The inferred low-velocity zone (LVZ) is marked by a vertical blue arrow.

CHAPTER 3

VELOCITY CONTRAST ALONG THE CALAVERAS FAULT FROM ANALYSIS OF FAULT ZONE HEAD WAVES GENERATED BY REPEATING EARTHQUAKES

Summary

The work in this chapter is published in Zhao and Peng (2009). We systematically investigate spatial variations of temporal changes and depth extent of damage zones along the Calaveras fault that ruptured during the 1984 Morgan Hill earthquake by the waveform analysis of 333 sets of repeating earthquakes. We use a sliding window waveform cross-correlation technique to measure travel time changes in waveforms generated by each repeating cluster. We find clear travel time delays in the S- and early S-coda waves for events immediately after the Morgan Hill mainshock. The amplitudes of the time delays decrease logarithmically with time since the mainshock, indicating a time-dependent recovery (healing) process following the abrupt co-seismic temporal changes. The largest temporal changes are observed at station CCO that is the closest to the rupture zone of the Morgan Hill mainshock. The time delays at this station are larger for clusters in the top 6 km, and decrease systematically at larger depth. In comparison, the time delays observed at other 5 stations are much smaller, and do not show clear relationship with hypocentral depth. We suggest that the temporal changes at these 5 stations mostly occur in the top few hundred meters of the near-surface layers, while the temporal changes at station CCO is likely associated with the damage zone around the Calaveras fault that is well developed in the top few kms of the upper crust. Our results

are consistent with the inference of a widespread damage and nonlinearity in the near-surface layers associated with strong ground motions of nearby large earthquakes, and localized damages and flower-type structures around active faults based on previous studies of fault zone structures and recent 3D numerical simulations.

3.1 Introduction

Measuring temporal changes around active fault zones (FZs) has been a long-sought goal in seismological community for many decades (Whitecomb et al. 1973; Aki and Chouet 1975; Poupinet et al. 1984; Aki 1985; Jin and Aki 1986; Crampin et al. 1990; Vidale and Li 2003; Schaff and Beroza 2004). A better understanding of the temporal evolution of FZ properties during earthquake cycles has important implications for many aspects of earthquake physics, including long-term evolutions of FZ structures, earthquake and fault interaction, and seismic hazard mitigation. In the last twenty years, many studies have succeeded in documenting temporal changes in the upper crust associated with the occurrences of large earthquakes, using repeating microearthquakes (Poupinet et al. 1984; Schaff and Beroza 2004; Rubinstein and Beroza 2004a, 2004b, 2005, 2007; Li et al. 2006; Peng and Ben-Zion 2006; Taira et al. 2008), repeatable controlled sources (Vidale and Li 2003; Nishimura et al. 2005; Li et al. 2006), spectral ratio methods (Sawazaki et al. 2006, 2009; Karabulut and Bouchon 2007; Wu et al. 2009a, 2009b), and seismic interferometry (Wegler and Sens-Schönfelder 2007; Brenguier et al. 2008a, 2008b; Ohmi et al. 2008; Wegler et al. 2009; Xu and Song, 2009). Their results generally show clear reduction of seismic velocities (Schaff and Beroza 2004; Rubinstein and Beroza 2004a, 2004b, 2005; Rubinstein et al. 2007a; Peng and Ben-Zion 2006), waveform coherencies (Baisch and Bokelmann 2001), or increase of

attenuation (Chun et al. 2004) during strong ground motions of nearby large earthquakes. The observed temporal change is most likely caused by widespread damages in the near surface layer and around active FZs associated with the strong ground motion and/or dynamic ruptures of nearby large earthquakes (e.g., Rubinstein and Beroza 2004a; Li et al. 2006; Peng and Ben-Zion 2006; Ma 2008). The observed co-seismic temporal changes, typically on the order of a few percent or less, are generally followed by logarithmic recoveries on the time scales of several months to years, indicating healing or re-strengthening processes of the damaged FZ rocks or near-surface layers (e.g., Vidale and Li 2003; Rubinstein and Beroza 2004a, 2004b; Peng and Ben-Zion 2006).

One of the outstanding questions in studying temporal changes in the upper crust is the depth extent of the damage zone. Here we use the term “damage zone” to represent the layer that have experienced significant fracturing or other types of damages in material strength during large earthquakes, resulting in clear temporal changes in seismic properties. A related term is “fault zone (FZ)”, which represent highly fractured low-velocity layers surrounding a fault interface (e.g., Ben-Zion and Sammis 2003). As mentioned above and will be discussed further below, both active FZs and near-surface layers are two likely candidates of damage zones formed due to the occurrence of nearby large earthquakes (e.g., Ma 2008). Indeed, recent studies based on repeating earthquakes have shown that the coseismic velocity reduction is mostly confined in the top 100-200 m of the near-surface layers (Rubinstein and Beroza 2005; Peng and Ben-Zion 2006). This observation is generally consistent with the laboratory observations and numerical simulations that nonlinear elasticity decreases with increasing compressive stress (i.e., depth) (Zinszner et al. 1997; Johnson and Jia 2005; Ma 2008; Finzi et al. 2009). In

comparison, other studies have shown that the coseismic temporal changes near active FZs could occur at much greater depth in the seismogenic zone (Schaff and Beroza 2004; Li et al. 2006; Rubinstein et al. 2007) or near the brittle-ductile transition zone (Taira et al. 2008). Hence, it is still not clear how to put these different observations together into a coherent picture of temporal changes in the upper crust associated with the occurrence of nearby large earthquakes.

Recently, Ma (2008) presented a unifying interpretation of both observations by simulating 3D dynamic rupture propagation on a vertical strike-slip FZ based on a pressure-dependent yield criterion in the upper crust. Because the yield stress depends on the confining pressure, the yielding occurs more easily near the surface than at depth. His simulation produces widespread damage zones away from the active FZ with a thickness of a few hundred meters or less, and a flower-type structure around active faults with broad damage zone in the top few kilometers of the crust and highly localized damage at depth. This explains both the near-surface damage and FZ damage at depth as observed in previous studies. A similar flower-type structure is obtained by Finzi et al. (2009), who performed 3D numerical simulations in a seismogenic upper crust governed by a continuum brittle damage framework. These numerical simulations suggest that the damages in the near surfaces and within FZ at depth could be observable through seismic observations, and are likely existing in the both regions.

Reliable detection of temporal changes generally requires collocated seismic sources (i.e., repeating earthquakes or artificial sources), so that the observed changes in travel times or waveform coherencies are mainly attributed to temporal changes in the medium, rather than spatial variations in the seismic sources (e.g., Peng and Ben-Zion

2005, 2006). In addition, many repeating sources at different depth are needed to better constrain the spatial variations and depth extent of the damage zone. In this study, we use more than 300 repeating clusters occurred along the central Calaveras fault in northern California to study temporal changes and depth extent of the damage zone associated with the occurrence of the 1984 Morgan Hill earthquake with a local magnitude (M_L) of 6.2. The repeating earthquakes occurred at the depth range of 1 to 10 km, and the corresponding waveforms are recorded by stations at variable distances from the rupture zone, allowing us to place a tight constraint on the spatial and depth extent of the damage zone.

Schaff and Beroza (2004) have used repeating earthquakes from this region to quantify temporal changes associated with the 1984 Morgan Hill earthquake. Our study is largely motivated by their success, but differs from that of Schaff and Beroza (2004) in the following aspects. First, Schaff and Beroza (2004) examined a wide region surrounding the rupture zones of the 1984 Morgan Hill earthquake and the 1989 Loma Prieta earthquakes based on waveforms generated by about 20 repeating clusters. In comparison, we focus on the immediate vicinity of the fault segment that ruptured during the 1984 Morgan Hill earthquake and used more than 300 repeating clusters to provide a better constraint on the spatial and depth extent of the damage zone. In addition, we use slightly different techniques to compute the time delays and quantify temporal changes. As will be shown below, our results are largely compatible with those from Schaff and Beroza (2004) and other recent studies (Rubinstein and Beroza 2004a, 2004b; Rubinstein et al. 2007; Li et al. 2006; Peng and Ben-Zion 2006), and confirm the aforementioned 3D numerical simulations on near-surface and FZ damages and the depth extent of the

damage zone (Ma 2008; Finzi et al. 2009). In the next section we first describe the steps to identify repeating earthquakes in our study region. In Section 3.3 we provide the detailed analysis procedure to measure temporal changes from waveforms of repeating earthquakes. The results are shown in Section 3.4 and discussed in Section 3.5.

3.2 Background And Repeating Cluster Identification

The Calaveras fault is one of the most active branches of the San Andreas Fault (SAF) system in northern California. It has generated at least 14 earthquakes with $M > 5$ since 1850 (Oppenheimer et al. 1990; Manaker et al. 2005), with the most recent event near Alum Rock on 2007/10/31 with a moment magnitude (M_w) of 5.6. The largest event was the $M_L 6.2$ 1984/04/24 Morgan Hill earthquake that ruptured the central portion of the Calaveras fault (Bakun et al. 1984) (Figure 3.1). Numerous aftershocks of the Morgan Hill mainshock were well recorded by the Northern California Seismic Network (NCSN) since then.

Using waveform cross-correlation and a double-difference method (Waldhauser and Ellsworth 2000), Schaff et al. (2002) relocated the seismicity along the central Calaveras fault around the rupture zone of the 1984 Morgan Hill earthquake. They found that earthquakes in this region are highly clustered in space and form repeating clusters. Using this relocated catalog, in the previous chapter, we identify 353 sets of repeating clusters (with at least 5 events in each cluster) around the rupture zone of the 1984 Morgan Hill earthquake. However, this identification procedure was solely based on the magnitude difference and overlapping rupture areas, and did not take into account waveform similarities. To further improve the quality of the obtained repeating clusters,

we add another constraint based on waveform similarities, which has been proven to be effective in discriminating repeating clusters at short inter-event distances (e.g., Nadeau et al. 1995; Menke 1999; Schaff et al. 2002; Templeton et al. 2008, 2009).

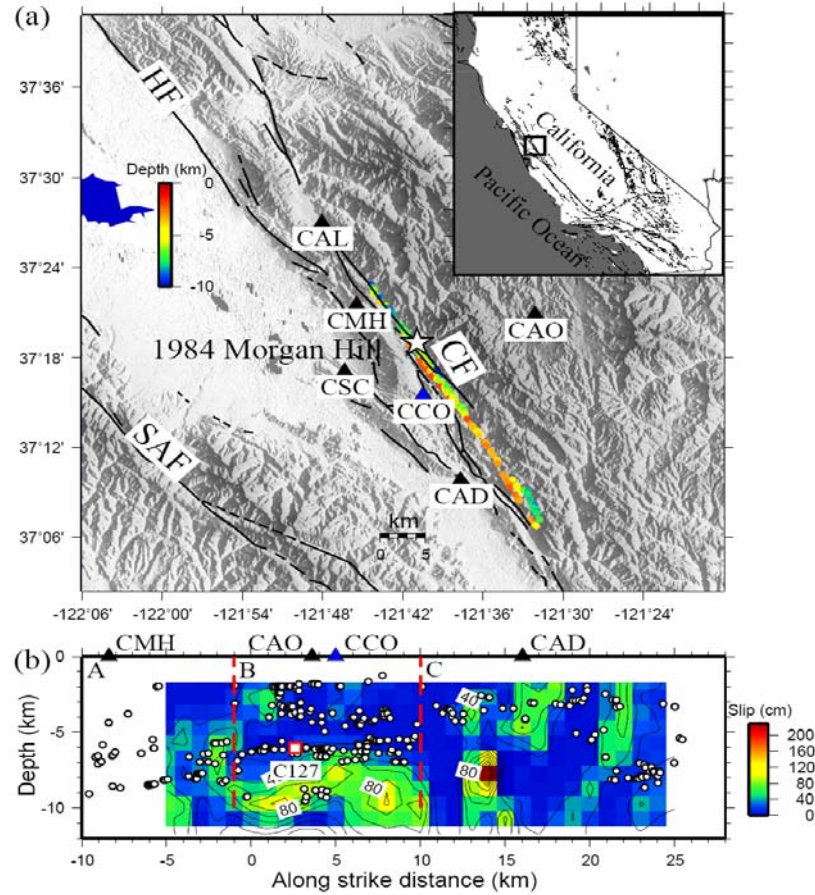


Figure 3.1. (a) Location of the central section of the Calaveras fault in northern California. Dark lines denote nearby faults. The circles denote the 333 repeating clusters identified in this study with color denoting their depths. The star and solid triangles mark the epicentral location of the 1984 Morgan Hill mainshock and six stations used in this study, respectively. Shaded background indicates topography with white being low and dark being high. The inset shows the map of California with the box corresponding to the study area. SAF, San Andreas fault; CF, Calaveras fault; HF, Hayward fault. (b) The centroid locations of 333 repeating clusters in the cross-section map along the Calaveras fault with the strike of 146°. The background color denotes the slip distribution of the Morgan Hill mainshock (Beroza and Spudich 1988). Waveforms generated by events in cluster C127 (the solid white square) are shown in Figure 3.4. The seismicity are separated into 3 segments (A-C) divided by red dashed lines to investigate the spatial pattern of temporal changes observed at station CCO, which are shown in Figures 3.8 and 3.9.

Our criteria of identification of repeating clusters generally follow those of previous studies (e.g., Nadeau et al. 1995; Waldhauser and Ellsworth 2002; Waldhauser and Schaff 2008; Lengliné et al. 2009). We require that each event pair within the same cluster has a magnitude difference of less than 1, 50% overlapping of rupture areas with the assumption of a circular crack model (Eshelby 1957) and a nominal 3-MPa stress drop, and minimum median waveform cross-correlation coefficients of 0.9. The first two criteria are the same as used in Zhao and Peng (2008). To calculate the similarity of every event-pair, we use vertical-component seismograms (100 samples per second) for all events listed in Schaff et al. (2002) and recorded by the short-period stations in the NCSN. A 1-20 Hz band-pass filter is applied to all the data. For each station, we only use events with hypocenter distances less than 50 km and the signal to noise ratio (SNR) larger than 5. Next, we compute the waveform correlation coefficients within a 3-s time window between all possible event-pairs. The 3-s time window starts 1 s before the predicted direct P arrival using a 1-D velocity model in central and northern California (Waldhauser et al. 2004). We then compute the median value of correlation coefficients between two events with at least three recording stations, and use it as a measure of similarity for these two events. Within each repeating cluster, we drop any event if the median value of similarities between this event and the rest is less than 0.9. After the preceding procedure, we identify a total of 333 repeating clusters (~2650 events) with at least 5 events in each cluster. The relative locations and waveforms for all clusters are visually inspected to ensure the co-location of each cluster (Figures 3.2, 3.4a). The largest event has a coda-duration magnitude (M_d) about 2.8.

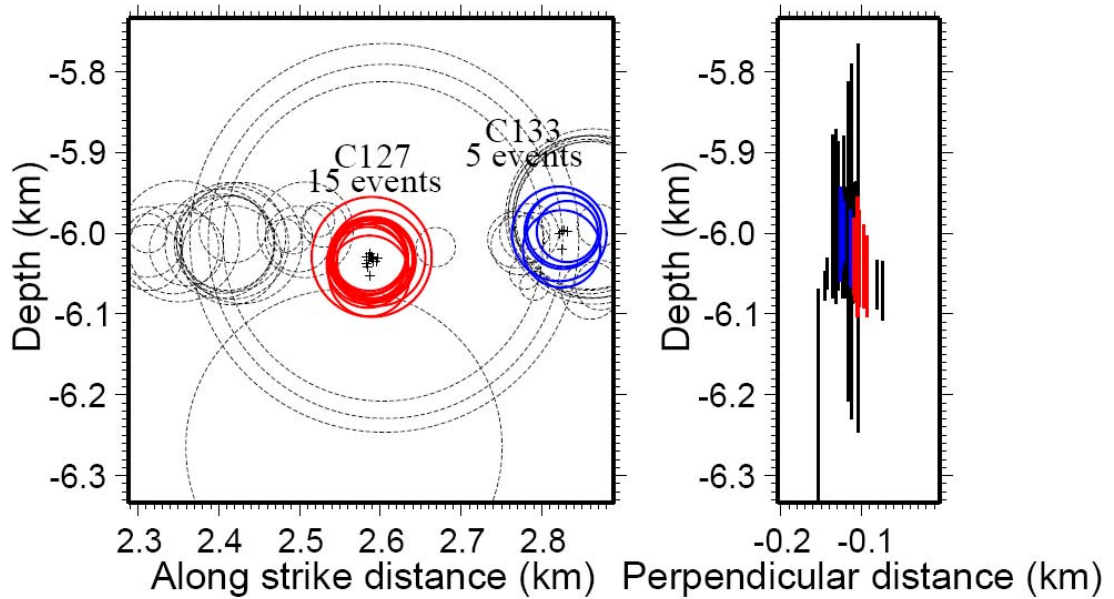


Figure 3.2. Cross-section views of 15 events within cluster C127 and its nearby cluster C133 (with 5 events) marked by the red and blue circles, respectively, from the (a) along-strike direction and (b) normal direction to the strike of the Calaveras fault. The source radius of each event is estimated from its catalog magnitude, based on a moment-magnitude relationship, with a circular crack model (Eshelby 1957) assuming a 3-MPa stress drop.

The locations of the repeating clusters obtained from this study are largely consistent with those from previous studies (Rubin 2002; Peng et al. 2005) with partially overlapping regions (Figure 3.3). The locations are slightly different as compared with those from another recent study in the same region (Templeton et al. 2009). The primary reason is that Templeton et al. (2009) identified repeating clusters based solely on waveform similarities without earthquake relocations. Hence, the disagreement is largely reflecting the intrinsic difference between earthquake locations from standard NCSN and relocated catalogs. The relocation algorithm (Waldhauser and Ellsworth 2000) use additional information from waveform similarity and relative arrival times of *P* and/or *S* phases among a group of events other than absolute arrival time from individual event in

conventional earthquake location methods. As a result, relocated catalogs generally provide more accurate relative locations of microearthquake than traditional ones (Waldhauser and Ellsworth 2000).

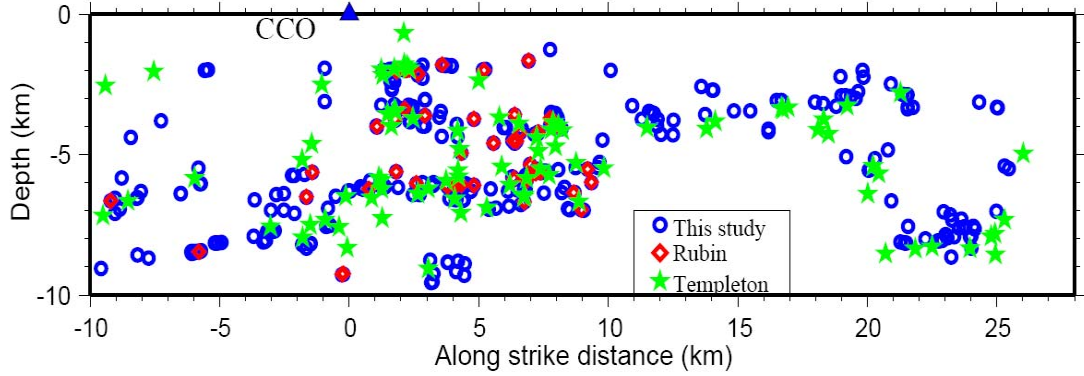


Figure 3.3. Comparison of centroid locations of repeating clusters from our study (blue open circles), Rubin (2002) (red open diamonds), and Templeton et al. (2009) (green asterisks) in the cross-section view along the Calaveras fault.

3.3 Analysis Procedure

We measure time delays for 6 stations around the rupture zone of the 1984 Morgan Hill mainshock (Figure 3.1a). The analysis procedure generally follows that of Niu et al. (2003) and Peng and Ben-Zion (2006). First, we remove the mean values and trends and apply a band-pass filter at 1-20 Hz to all traces. Next, we select seismograms with a minimum SNR of 5, and choose a reference trace for each station-cluster pair. Since most clusters do not have events before the mainshock, the waveform corresponding to the last event in each station-cluster pair is chosen to be the reference trace. Many previous studies have observed a logarithmic recovery of the coseismic damage to the pre-mainshock level (Vidale and Li 2003; Peng and Ben-Zion 2006; Sawazaki et al. 2006, 2009), indicating that the postseismic recovery mostly occurs within the first few months. Hence, we use the reference trace as a proxy for the pre-

mainshock level, assuming that the co-seismic changes have fully recovered to the pre-mainshock level over ~ 10 years. It is worth pointing out that such assumption is not valid if rocks have experienced permanent damages that cannot be completely recovered to the postseismic stage (e.g., Schaff and Beroza 2004). In this case, using the last event as the reference would result in lower co-seismic changes than those by using the event before the mainshock as the reference.

We note that the locations of stations CAD and CCO have been changed by about 14 m at December 1992 and 130 m at April 1996, respectively (<http://www.ncedc.org/ftp/pub/doc/ncsn/ncsn.stations>). After carefully checking the results from these two stations, we find that temporal changes estimated from CCO could be contaminated due to such change in the station location. Thus, for this station, we only analyze seismic data recorded prior to April 1996. Finally, we align all other traces to the reference trace by cross-correlating a 1-s time window that is 0.2 s before the corresponding picked P arrivals. We also require that all other traces have a minimum correlation coefficient of 0.8 with the reference trace.

After the above preprocessing steps for each station-cluster pair, a sliding window waveform cross-correlation technique (Niu et al. 2003; Peng and Ben-Zion 2006) is used to measure travel-time differences $\tau(t)$ and de-correlation index $D(t)$ (defined as one minus the maximum cross-correlation coefficient between two events) of subsequent traces to the reference trace in each station-cluster pair (Figure 3.4). The time window is 1-s long, sliding 2 s before and 15 s after aligned P arrivals, with sliding interval of 0.1 s in each step. A cosine taper is applied to each time-window with 10% of the entire width to reduce the Gibbs' phenomenon (Niu et al. 2003; Peng and Ben-Zion 2006). To

increase the precision of measured time delays, we linearly interpolate the band-pass-filtered vertical seismograms from 100/s to 10,000/s before calculating the travel-time differences and de-correlation indexes. Figure 3.4 shows an example from Cluster 127 recorded at station CCO. The measured travel time differences are mostly positive, corresponding to reductions in seismic velocities, and the overall amplitudes of time delays decrease with time since the mainshock (Figure 3.4). The de-correlation indexes also show similar patterns after the mainshock. In this study, we only use travel-time differences to quantify the temporal variations of seismic velocity in the study region.

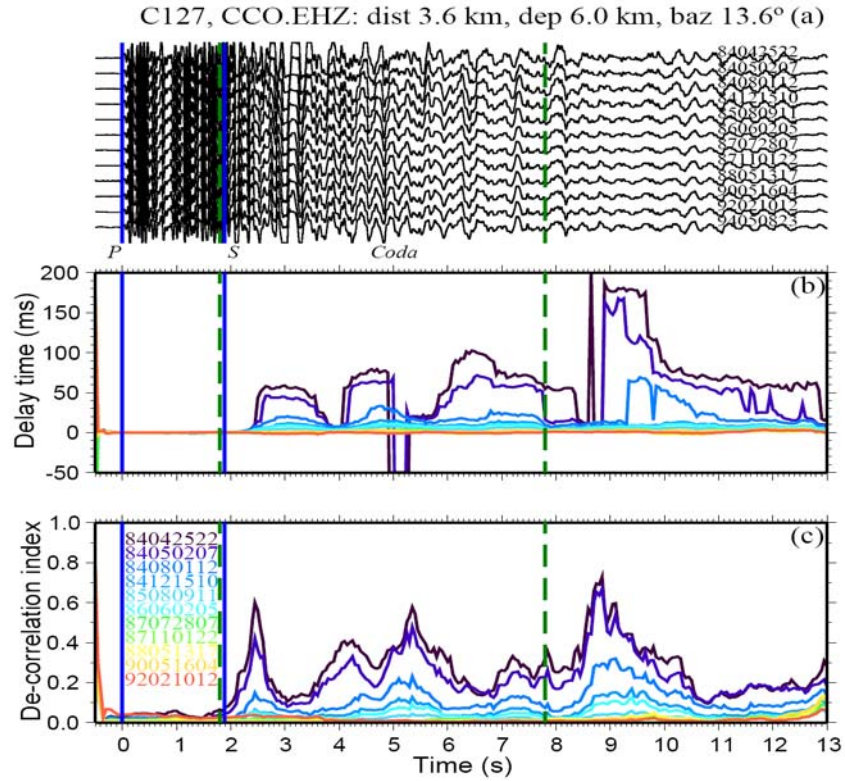


Figure 3.4. (a) Vertical-component seismograms generated by the 15 events in cluster C127 and recorded by station CCO. Seismograms are aligned by P waves at 0 s. Calculated (b) delay time $\tau(t)$ and (c) de-correlation coefficients. The green vertical dashed lines denote the 6-second time window with 0.1 second before direct S waves, which is used to compute the median delay time. The event ID members are marked on the panels (a) and (c), consisting of the occurrence time of corresponding event (2-digit-year, 2-digit-month, 2-digit-day, and 2-digit-hour).

For each station-cluster pair, we use the median value of the calculated time delays within a 6-s time window to quantify the travel time changes relative to the reference trace. We do not fit the slope of the measured time delays, as was done in some previous studies (e.g., Poupinet et al. 1984; Schaff and Beroza 2004; Rubinstein et al. 2007), because we find that in most cases time delay does not increase monotonically with the travel time (e.g., Figure 3.4b). In addition, our synthetic tests in Appendix A (Chapter 3.6) have shown that the median value could be used as a better parameter to quantify the depth dependence of temporal changes than the slope. We compute the median, instead of the mean value to avoid potential contaminations from glitches in the travel time delays (mostly due to low SNR). The 6-s time window is 0.1 s before the manually picked direct S arrival (Figure 3.4), so that it contains both direct S and early S coda waves. Including early S coda wave helps to stabilize our results at each station, because of the averaging effect due to superposition of scattered waves from all the possible azimuths and paths (Aki 1969). In addition, the travel time differences in the early S-coda waves are generally much larger than those in the direct S waves (e.g., Schaff and Beroza 2004; Rubinstein et al. 2004a; Peng and Ben-Zion 2006), allowing us to better quantify the difference in each event-station pair. We do not include the late S coda waves mainly because of the diminishing SNR with increasing travel time. We note that the time delays calculated in this study reflect the changes of the differential arrival times between S and P waves, because of the alignment of P arrivals in the previous steps. In reality, several studies have observed temporal changes in the P waves, although the values are much smaller than for the S waves (Schaff and Beroza 2004; Li et al. 2006).

Hence, the obtained temporal changes are probably lower bounds (Rubinstein and Beroza 2004a; Peng and Ben-Zion 2006).

Figure 3.5 shows the median time delay of two repeating clusters versus the lapse time since the mainshock for station CCO. The median time delays generally follow a linear decay trend with the logarithmic lapse time, consistent with previous studies (e.g., Peng and Ben-Zion 2006). Therefore we linearly fit the trend with a least-squares method for each station and calculate the slope of the postseismic recovery (Figure 3.5). We also find clear increase of time delays at most stations on 1986/03/31, which corresponds to the occurrence time of a local magnitude (M_L) 5.7 event near Mt. Lewis in this region (Zhou et al. 1993). This event is the largest earthquake occurred within 50 km after the 1984 Morgan Hill earthquake. To avoid potential contaminations in the time delays from this event, we only fit the data before its occurrence time (Figure 3.5). The decay of time delays might also be fitted by other functions, such as an exponential function. Since the physical mechanism of recovery is still unclear, it is difficult to determine which function is the best to be used to fit the trend. In addition, the main purpose of fitting is to qualify the recovery rate in this study, different fitting functions should not provide inconsistent results in this sense. Then we plot the median time delay of every event versus the lapse time since the mainshock for the six stations in Figure 3.6.

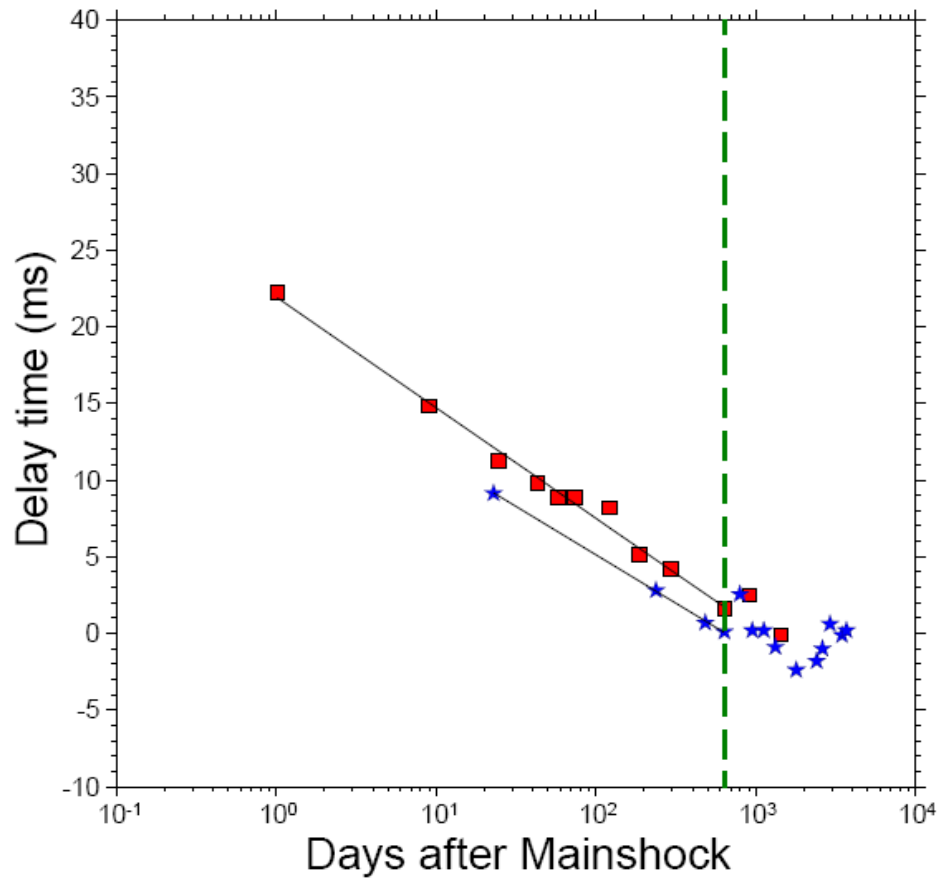


Figure 3.5. An illustration of median delay time from two repeating clusters marked as red squares and blue stars, respectively, plotted against the logarithmic elapsed time since the 1984 Morgan Hill earthquake recorded at station CCO. Two lines represent least-squares fits to the data for each cluster, respectively. The green dashed vertical line marks the occurrence times of a local 1986 $M_L 5.7$ event.

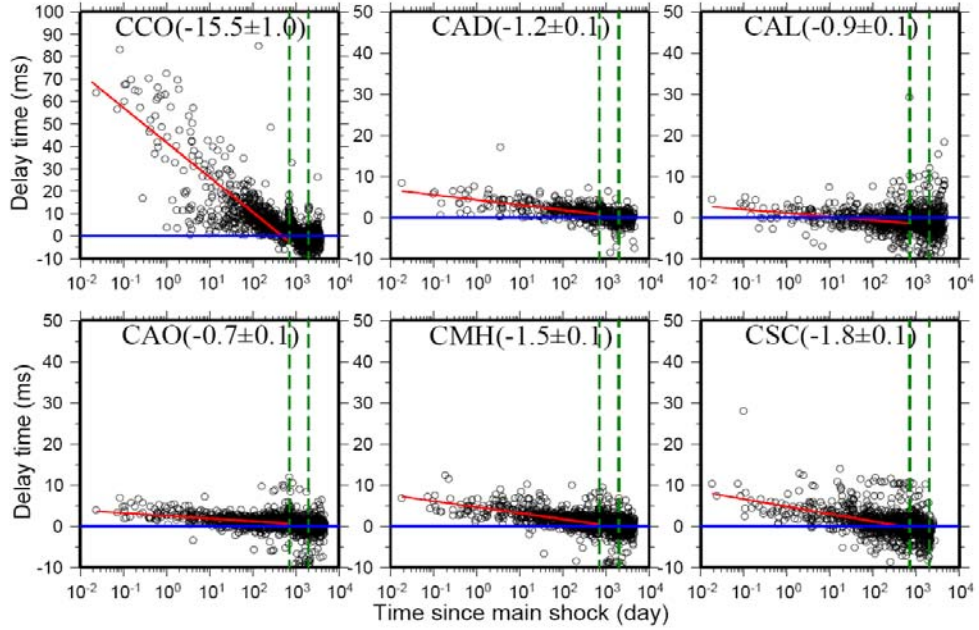


Figure 3.6. Median delay time plotted against the logarithmic elapsed time since the 1984 mainshock for the vertical-component seismograms recorded at the 6 stations. The red line in each panel represents a least-squares fit to the data. Two green dashed vertical lines mark the occurrence times of a local 1986 $M_L 5.7$ event and the 1989 Loma Prieta earthquake, respectively.

3.4 Spatial Variations Of Temporal Changes

3.4.1 General Observations

Because most clusters do not have events before the Morgan Hill mainshock, we use the slope of least-squares fitting and time delays at 24 hrs (one day) after the mainshock (i.e., computed from the slope and intercept at one day of the least-squares fitting) as a proxy for the co-seismic changes. Although the temporal changes are much larger during and immediately after the mainshock (e.g., Sawazaki et al. 2006, 2009; Wu et al. 2009a, 2009b), we do not have enough repeating events within this period, especially at larger depth, to provide a better constraint. As shown in Figure 3.6, all 6 stations have positive coseismic temporal changes, corresponding to reductions of

seismic velocities in this region. However, their amplitudes are quite different. The largest temporal change is shown at station CCO, with a slope of ~ -15 ms per decade change in time and time delay of ~ 40 -70 ms at one day after the mainshock. In comparison, the values at other 5 stations (i.e., CAL, CSC, and CMH, CAO and CAD) are much smaller, with slopes of ~ -1 ms/decade and time delays of less than 10 ms. Figure 3.6 also shows that the time delays at the 5 stations generally follow the logarithmic recovery trends without significant deviation, indicating a weak dependence of time delays on the locations of repeating clusters. In comparison, the time delay measurement at station CCO is more scattered than that for other 5 stations.

To further illustrate this, we plot in Figure 3.7 the time delays at one day after the mainshock from the least-squares fitting for each repeating cluster versus its depth. We find no systematic relationship between the time delays and the hypocentral depths for those 5 stations. In comparison, we find that the time delays at CCO are scattered in the top 6 km, but weakly decrease from 6 to 10 km. The overall correlation coefficient (CC) between the time delays and depths is 0.36. If we select only events below 6 km, the CC value is 0.51. Although both values are relatively low, we can rule out the probability of random occurrence at 95% confidence level.

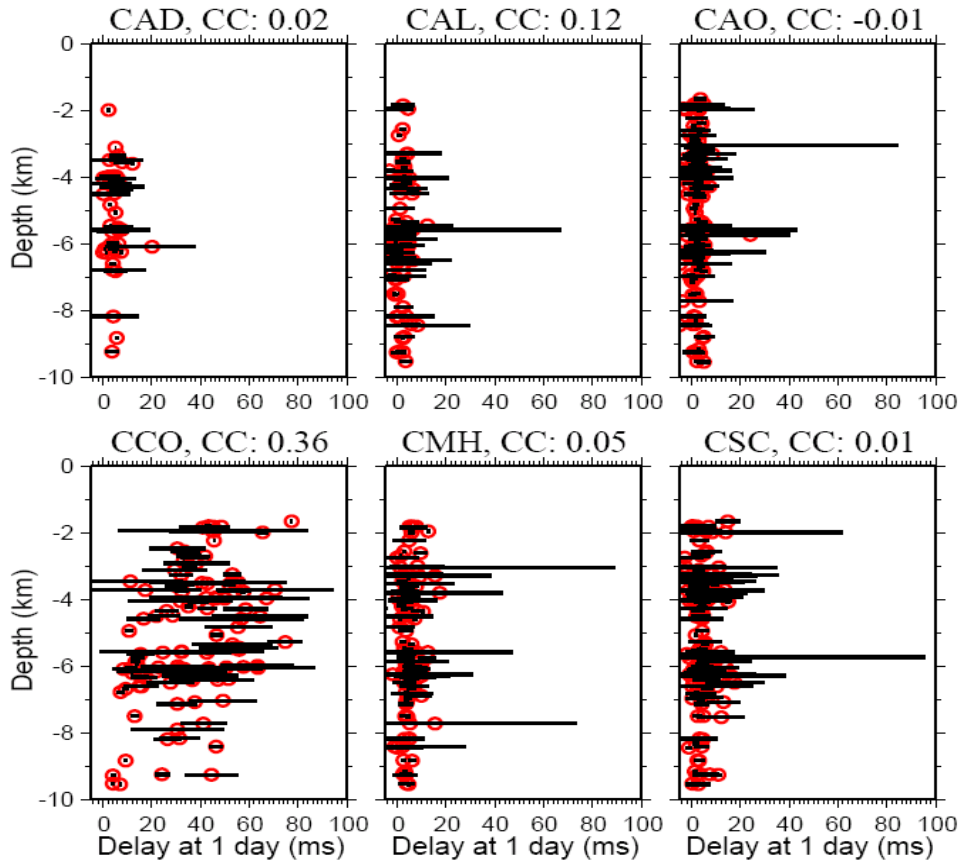


Figure 3.7. Delay-time at one day after the 1984 mainshock versus depths of events. The delay-time is calculated from least-squares fitting for corresponding repeating cluster with at least 3 events occurred between the 1984 mainshock and the 1986 event (see the text for details). The black horizontal lines mark the error of least-squares fitting from the corresponding events. Station name and correlation coefficient between delay-time and depths are labeled on the top of corresponding panel.

3.4.2 Possible Regions of Temporal Changes

To better understand the physical processes corresponding to the observed temporal changes, it is important to constrain the regions where temporal changes have occurred. The temporal changes could arise from source regions, propagation paths, and in the near-surface layers beneath the station (e.g., Rubinstein and Beroza 2004a; Peng and Ben-Zion 2006; Rubinstein et al. 2007a). If the temporal changes are mainly from the source region (i.e., immediately around the repeating clusters at seismogenic depth), we

would expect the time delays calculated from different stations for the same repeating cluster to be similar. If the temporal changes are mostly accumulated along the propagation paths, the observed time delays for a given station could vary systematically depending on the locations of repeating clusters. When the ray path between the station and repeating cluster is along or cut across a damage zone during propagation, such as an active FZ that is further damaged during the mainshock, we would expect to observe large temporal changes. On the other hand, if the seismic ray does not sample the damage zone, the observed temporal change would be much smaller. Finally, if most temporal changes are accumulated in the near surface layers, the observed time delays at a given station should be similar and do not have a strong dependence on the ray paths (i.e., the locations or the depths of the repeating clusters).

As shown in Figures 3.6 and 3.7, the time delays for the 5 stations (CAL, CSC, and CMH, CAO and CAD) are relatively small and we find no systematic correlation between the time delays and the hypocentral depths. Hence, we infer that the time delays are mostly accumulated in the near-surface layers beneath the 5 stations, which is also consistent with previous studies in this region (Schaff and Beroza 2004; Rubinstein and Beroza 2004a, 2004b). On the other hand, the time delays at CCO are much larger and show clear scatter around the fitted line (Figure 3.6) and systematic variations with hypocentral depth (Figure 3.7). These observations indicate that the temporal changes are not just accumulated in the near-surface layers, but also along the ray paths at larger depth. In the following section, we focus only on the measurements at station CCO and further quantify the path and depth dependence effects.

3.4.3 Depth Extent of the Damage Zone around Station CCO

To verify whether time delays at CCO are path dependent, we first divide the entire repeating clusters into 3 segments according to their along-strike distances to CCO (Figure 3.1b). We find some variations in the time delays for different segments (Figure 3.8). The coseismic changes and decay rates for segments to the NW (Segment A) and SE (Segment C) sides of CCO are about the same with less scatter. The most complicated feature is from Segment B, which is directly beneath station CCO with its along-strike distance from -1 to 10 km. The decay rates in Segment B appear to follow several different trends. Similar to Figure 3.7, we also plot the delay times at one day after the 1984 mainshock for each repeating cluster at these 3 segments (Figure 3.9). In Segment A, the clusters satisfying our criteria all occurred at the depth range of 6-9 km, and hence the delay times do not show clear variations with depth. In segment C, there is a weak increase of delay times from 2.5 to 4 km. After that, the delay times remain more or less constant. In segment B, the delay times show large variations in the top 6.5 km, and decrease significantly below 6.5 km, much clearer than the general patterns shown in Figure 3.7.

Finally, we divide the Segment B into 4 zones based on their hypocentral depths (Figure 3.10). Again we find a clear depth dependence of temporal changes. The largest coseismic change is from the shallow zone (0 to 5 km at depth) with a slope of -17.4 ms/decade, and the values decrease for deeper zones. In addition, the time delays for each zone generally follow a linear trend by visual inspection, except for Zone 3, which appears to have multiple distinct trends. In Zone 3, the slope of the higher decay trend is close to that of the shallow segment (i.e., Zone 1), whereas the slope of the lower decay trend is close to that of the deep segment (i.e., Zone 4). However, we can not find a clear

boundary at which depth the damage ceases (i.e., the slope is zero or near zero), which indicates a possible spatial variation of damage zones along the fault.

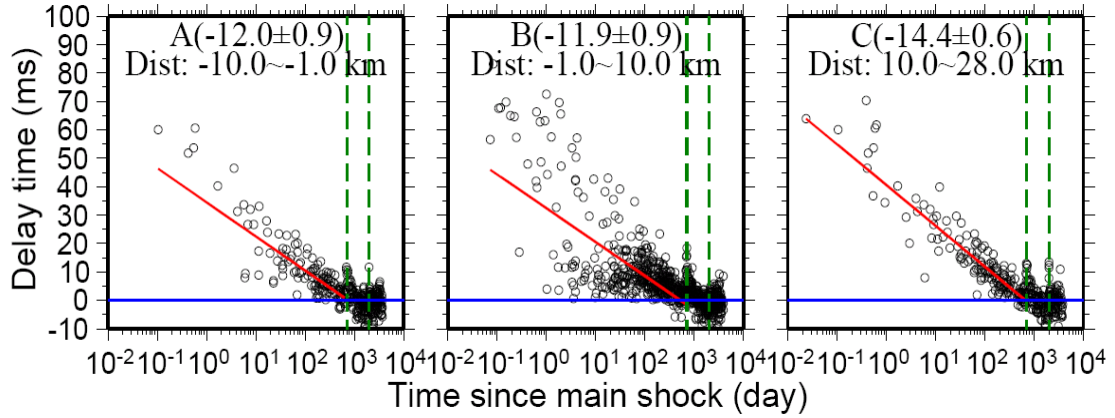


Figure 3.8. Median delay time plotted against the logarithmic elapsed time after the 1984 Morgan Hill earthquake for the vertical-component seismograms recorded at station CCO from three segments marked in Figure 1b. The along-strike distance of the corresponding segment is labeled within each panel. Other symbols are the same as Figure 3.6.

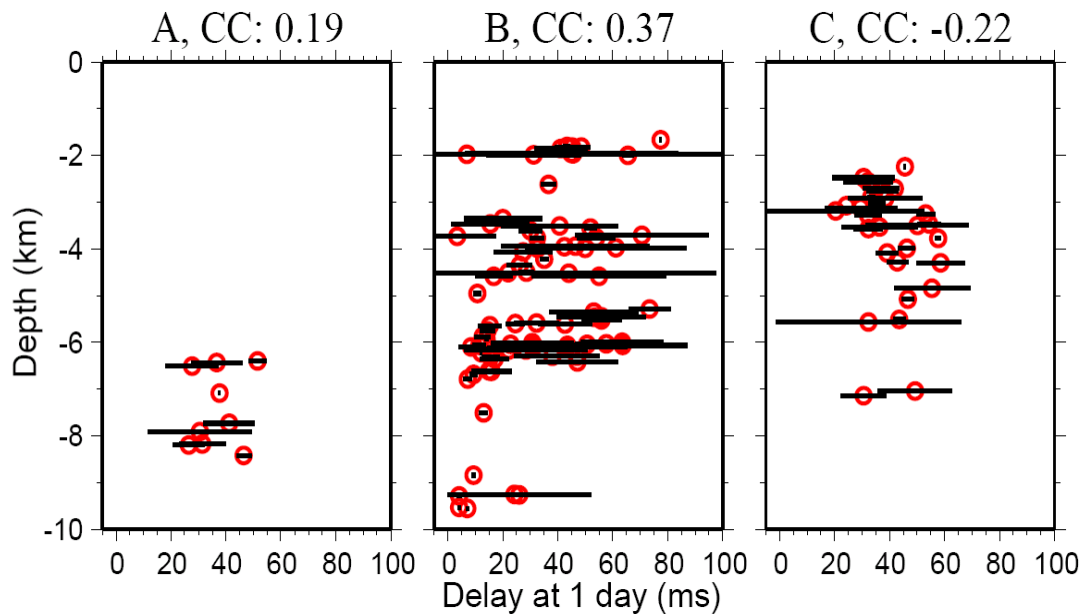


Figure 3.9. Delay-time at one day after the 1984 mainshock versus depths of events recorded at station CCO from different segments (Figure 3.1b). Other symbols are the same as Figure 3.7.

3.5 Discussions

In this study, we investigated the spatial variations and depth dependence of temporal changes along the central segment of the Calaveras fault that ruptured during the 1984 Morgan Hill earthquake. Clear temporal changes have been observed immediately after the mainshock, associated with increasing arrival times in the direct S and early S coda waves. The observed time delays systematically decrease with logarithmic time since the mainshock. Such time-dependent recovery is likely related to the healing processes of damaged FZ rocks or near-surface layers as inferred from many previous studies (Vidale and Li 2003; Schaff and Beroza 2004; Peng and Ben-Zion 2006). We also found clear spatial variations in the observed temporal changes. The largest temporal changes are found at station CCO that is the closest to the rupture zone of the Morgan Hill mainshock. In addition, the temporal changes are larger in the top 6 km and decrease systematically at larger depth. Due to the close proximity of the CCO station to the rupture zone of the Morgan Hill mainshock, we suggest that the observed temporal changes are related to the low-velocity damage zone around the Calaveras fault. In comparison, the temporal changes at the other 5 stations are much smaller, and do not show clear relationship with hypocentral depth. We infer that the observed temporal changes at these 5 stations mostly occur on the top few hundred meters of the near-surface layers, consistent with previous studies in this region (Schaff and Beroza 2004; Rubinstein and Beroza 2004a, 2004b).

Similar to previous studies (e.g., Rubinstein and Beroza 2004a; Peng and Ben-Zion 2006), we invoke nonlinear site response to explain the relatively small temporal changes at the 5 stations. Laboratory simulations and field observations have shown the

reductions of both shear-wave velocity and amplification effects in shallow soil layers due to the nonlinear elastic behavior under large shear strains (Beresnev and Wen 1996; Johnson et al. 1996; Sawazaki et al. 2006). In this situation, considerable seismic energy is consumed to create new fractures and open existing cracks, which in turn effectively reduce the seismic velocity (Schaff and Beroza 2004; Rubinstein and Beroza 2004a; Peng and Ben-Zion 2006), and increase attenuation (Chun et al. 2004) during strong ground motions. Because the nonlinearity is generally prohibited with increasing confining pressure, the co-seismic damage and temporal changes are likely constrained at shallow depth, consistent with the observed patterns (Figures 3.6 and 3.7) for these 5 stations. The interpolated time delay 15 minutes (0.25 hour) after the mainshock is about 5-10 ms. If we assume that the damage zone is confined in the top 200 m of the shallow layer with an average S-wave velocity of 1.0 km/s, the estimated minimum coseismic S-wave velocity drop near these 5 stations is about 2.5%-5%, which is compatible with the observation of Schaff and Beroza (2004) in the same region.

In comparison, the temporal changes observed at station CCO are much larger and show weak dependence with hypocentral depth. The rock unit at station CCO is Knoxville Formation (Rubinstein and Beroza 2004a), which is the lowest part of the Great Valley Sequence deposited during late Jurassic to early Cretaceous. It is mainly dark, greenish and gray shale with sandstone interbeds and could locally include conglomeratic sandstone in the lower part (Graymer et al. 1994). Phillips and Aki (1986) studied the local site amplification in central California using the decay of coda waves, and found that stations with large positive site amplification factor also observed strong velocity changes after the 1979 Coyote Creek earthquake immediately south of our study

region (Poupinet et al. 1984). This is consistent with the aforementioned explanation that the velocity changes for most stations are caused by temporal changes in local site effects. Rubinstein and Beroza (2004a) also used the correlations between the coda amplification factors and the observed temporal changes to argue for the existence of widespread nonlinear strong ground motion. We note, however, that the coda amplification factor for CCO is only about -0.9 (Phillips and Aki 1986; Rubinstein and Beroza 2004a), which is not expected to generate large seismic velocity drop near this station. In summary, we suggest that temporal changes observed at station CCO are likely accumulating at larger depth, rather than in the near-surface layer alone.

The synthetic calculation in Appendix A showed that for a station inside a FZ with uniform thickness and co-seismic reduction of FZ velocities, the observed median time delay increases systematically with increasing depth, while the slope of the time delay remains near constant. To explain the decrease of time delay with increasing depth at station CCO, we need to place most of the sampled temporal changes in the top few kms of the FZ (Figure 3.11). A common FZ structure as inferred from previous seismic refraction measurements and 3D tomographic studies is a wedge-shape model that is wider in the top few kms and narrower at larger depth (e.g., Cormier and Spudich, 1984; Blümling et al., 1985; Mooney and Colburn 1985; Mooney and Ginzburg, 1986; Michael 1988). Such a wedge-shape FZ model (i.e., Figure 3.11) is also consistent with a hierarchical flower structure as inferred from recent observations of FZ trapped waves (e.g., Rovelli et al., 2002; Ben-Zion et al. 2003; Peng et al. 2003; Lewis et al. 2005; Cochran et al., 2009), near-fault crustal anisotropy (Cochran et al. 2003, 2006; Peng and Ben-Zion 2004; Zhang et al. 2007), and geological studies of strike-slip FZs (e.g.,

Sylvester, 1988; Rockwell and Ben-Zion 2007). Below we attempt to use such wedge-shape FZ model to explain the observed temporal changes in this study.

The Calaveras fault, like many other active plate-boundary faults (e.g., Ben-Zion and Sammis 2003), is characterized by localized belts of damage zones that have considerably lower elastic moduli than the surrounding rocks (Mooney and Colburn 1985; Spudich and Olsen 2001). The inferred low-velocity FZ in this region has a width of about 1-2 km at surface (Blümling et al., 1985), and extends to the depth of approximately 5 km (Michael 1988). Such low-velocity FZ is likely a cumulative effect due to faulting related damages during major earthquakes such as the 1984 Morgan Hill mainshock, and probably long-term creeps localized in the shallow crust (Templeton et al. 2009). Cormier and Spudich (1984) computed synthetic seismograms based on a wedge-shaped low-velocity zone around the Calaveras fault, and found clear focusing of seismic ray within the wedge, consistent with the observations of local amplification within the FZ in previous studies.

Station CCO is about 80 meters to a mapped Holocene-active fault at surface (measured from USGS Quaternary-active fault map of San Francisco Bay area), and is about 2 km from the main strand of the Calaveras fault interface as inferred from the surface projection of the active seismicity (Figures 3.1 and 3.10). Clear FZ head waves (Zhao and Peng 2008) and possible signals of FZ trapped waves (e.g., Figure 3.4) are observed at station CCO, indicating that this station is very close to the Calaveras FZ. We suggest that the observed temporal changes at station CCO are mostly confined in the wedge-shaped low-velocity zone as inferred from previous seismic refraction measurements (Blümling et al., 1985; Mooney and Colburn 1985) and 3D tomographic

studies (Michael 1988). Because of the intrinsic weakness, its close distance to the dynamic rupture of the 1984 Morgan Hill mainshock, and the focusing effects within the wedge, the Calaveras FZ beneath CCO probably experience strong shaking and large dynamic stresses during the mainshock, resulting in further damages in material strength and subsequent recoveries. In addition, because the wedge-shaped damage zone is most prominent at shallow depth, seismic rays from repeating earthquakes in the top few kms of the fault provide an adequate sampling of the damage zone, resulting in a large time delay. In comparison, seismic rays for deeper clusters could have a significant portion sampling the less-damaged host rock before reaching the station CCO. Hence, the observed time delay is much smaller than those at shallower depth.

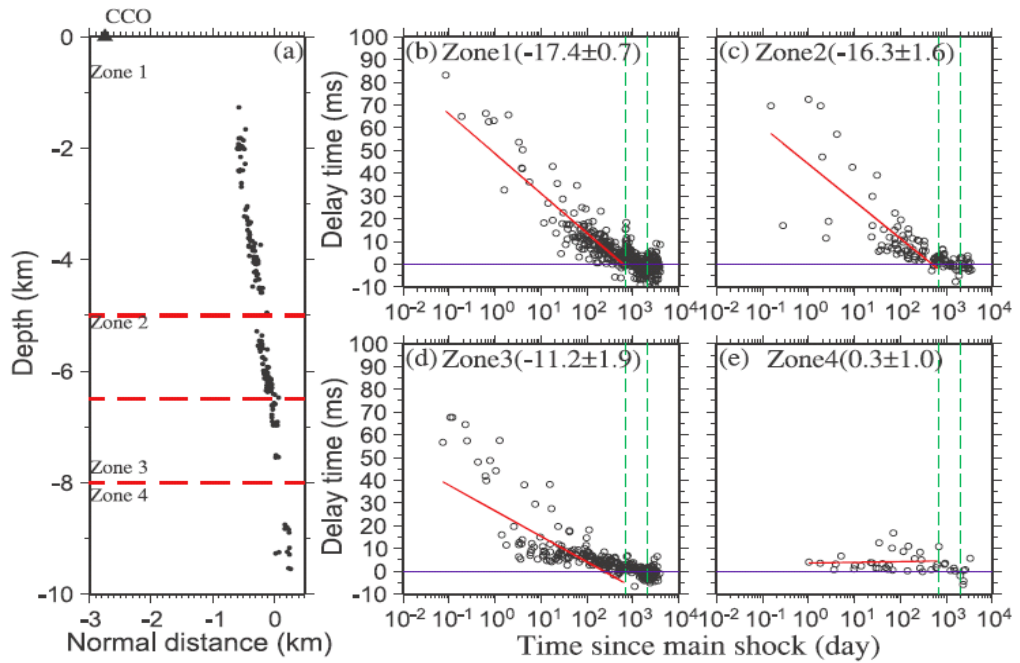


Figure 3.10. (a) Cross-section views of seismicity in Segment B perpendicular to the strike of the fault. The along-strike distance of these seismicity are from 1 to 10 km. The seismicity is further divided into 4 zones based on the depths range (red dashed lines). (b)-(e) Median delay time for the S coda waves plotted against the logarithmic elapsed time after the 1984 Morgan Hill earthquake for the vertical-component seismograms recorded at station CCO from different segments (Figure 3.10a). Other symbols are the same as Figure 3.6.

In this study, we found that the inferred damage zone around CCO is most prominent in the top 5-6 km, and the degrees of damage decrease systematically at larger depth. Hence, the observed temporal changes are largely accumulating above the mainshock rupture patches at the depth range of 6-8 km beneath station CCO, as obtained from kinematic slip inversions (Beroza and Spudich 1988). Previous studies have suggested that the propagating crack tip of an earthquake rupture could induce large dynamic stress and generate significant damages around the ruptured FZ (Li et al. 2006; Ma 2008). However, our results inferred a rather small temporal change around the ruptured region at depth (e.g., Figure 3.10).

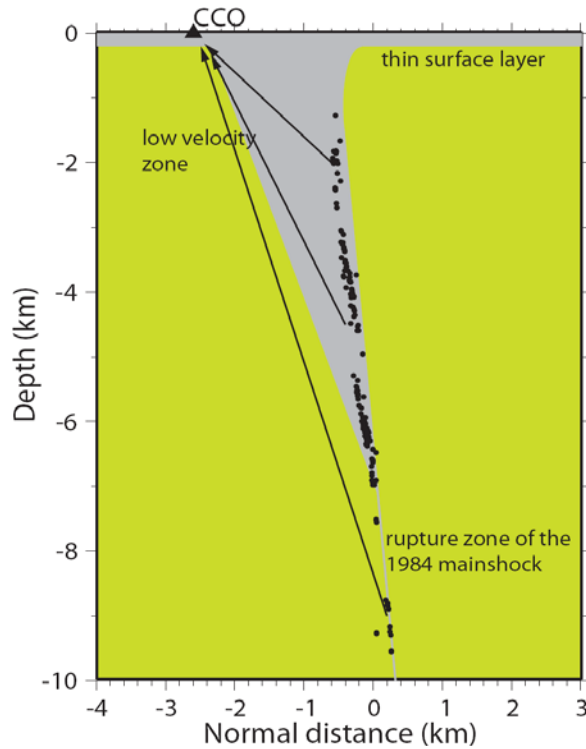


Figure 3.11. A schematic diagram showing the damage zone adjacent to the Calaveras fault near station CCO. The damage zone is marked by the gray color, consisting of a shallow surface layer and a deep low-velocity zone extending to about 6 km at depth. The black dots and arrows denoted the seismicity and ray paths, respectively.

A potential bias of small temporal changes at larger depth (e.g., 8-10 km) is the lack of repeating earthquakes in this depth range, especially in the first few hours immediately after the mainshock, and a few years afterwards (e.g., Figure 3.10). The lack of early repeating aftershocks could be explained by a delayed response of postseismic creep at larger depth (e.g., Peng and Zhao 2009), while the lack of late repeating aftershocks is likely due to the diminishing strain rate and postseismic shallowing of the brittle-ductile transition zone at depth (e.g., Schaff et al. 2002; Rolandone et al. 2004; Kaneko and Lapusta, 2008). To rule out such bias, we have chosen to extrapolate the time delays to 1 day after the mainshock so that there are enough data points at larger depth to provide constraints. While the lack of late repeating aftershocks may lower the coseismic changes, such effect is minor because the majority of the co-seismic change is recovered in the first few months due to the logarithmic dependence of time. The only exception is if permanent damages occurred coseismically (e.g. Schaff and Beroza 2004), the extrapolated 1-day time delays would be lower bound estimate of the true co-seismic changes. In addition, we only fit the data before the occurrence of the Mt. Lewis earthquake in 1986/03/31, when the majority of the deep cluster ends. Hence, we argue that the observed depth-dependent effects are unlikely to be purely caused by less sampling points at larger depth, but rather represent a genuine feature of damage suppression with increasing depth.

An alternative explanation is that large coseismic changes do occur below 6 km, due to the close proximity of the rupture zone at 6-8 km. However, the temporal changes are not sampled adequately by the deep clusters for the following reasons. First, as mention before, the seismic rays from the deep clusters could leave the deep FZ that is

highly damaged, propagate mainly in the less damaged host rocks, and finally bend towards the FZ to be recorded at station CCO. In addition, if the damage zone is so highly localized at seismogenic depth (e.g. Ma 2008) that the width of the damage zone is much smaller than the wavelength of the seismic waves, such localized damages may not be detected (Wu et al. 2008). Another possibility is that the coseismic damages at 6 km and larger depth recover faster in the first few hours because of the higher confining pressure at larger depth (Finzi et al. 2009), leaving small temporal changes to be observed at later times. Unfortunately, our repeating cluster is derived from the relocated catalog of Schaff et al. (2002) with many early aftershocks (and presumably repeating aftershocks) missing in the first few hours after the mainshock (Peng et al. 2006, 2007). Hence, at present we do not have enough temporal resolutions to favor or rule out such possibility. A systematic search of missing repeating aftershocks immediately after the mainshock (e.g., Peng and Zhao 2009; Lengliné et al. 2009) may help to provide important constraints on whether large co-seismic changes and fast post-seismic recovery occur at larger depth or not.

In addition to the distances to and depth within the active FZ, the rupture direction of the 1984 mainshock could also play an important role in controlling the observed temporal changes. It is well known that radiated seismic energy is concentrated in the rupture direction due to the so-called directivity effect. Because the rupture direction of the 1984 Morgan Hill earthquake is to the SE (Bakun et al. 1984), we expect larger ground motions and hence larger temporal changes for station in that direction. For example, stations CAL, CSC, and CMH are all close to active FZs, but the observed temporal changes are not as large as that of CCO, which could be due to the fact that

these stations in not in the rupture direction of the Morgan Hill mainshock, and hence experienced relatively small strong ground motions. Station CAD is in the rupture direction, but is relatively far from the Calaveras fault as compared with station CCO. Overall, our observations are consistent with the previous inferences that the stations with large temporal changes are generally close to the rupture zone of the mainshock, and have experienced large co-seismic strong ground motions (Schaff and Beroza 2004; Rubinstein and Beroza 2004a, 2004b; Rubinstein et al. 2007; Peng and Ben-Zion 2006).

As mentioned before, recent 3D dynamic rupture simulations have produced widespread damages in the near-surface layers and localized flower-like damage zones around active FZs at depth (Ma 2008; Finzi et al. 2009). The flower-type structure is a direct result of damage suppression due to increasing confining pressure with depth. Ma (2008) also suggested that widespread near-surface damages are mainly caused by strong seismic waves, and the narrow damage zone at depth is mainly induced by dynamic stresses associated with the rupture front. Another recent study based on InSAR images has shown a clear subsidence of the surface after the 2003 Bam earthquake in Iran (Fielding et al. 2009). They suggested that postseismic subsidence/compaction is likely associated with the healing processes in the shallow FZ that is co-seismically damaged during the mainshock. In this study, we found that the temporal changes at the other 5 stations away from the Calaveras fault that ruptured during the Morgan Hill earthquake are mainly constrained in the near-surface layers, while at station CCO we attributed the observed temporal changes to the damage zone associated with the Calaveras fault at larger depth. Hence, our observations are generally consistent with these recent numerical simulations (Ma 2008; Finzi et al. 2009) and geodetic observations (Fielding et al. 2009).

We note that the co-seismic damages and recovery processes observed in this study are associated with a single mainshock. Over the geological time scales, such repeated damages and healing processes may produce permanent changes inside active faults, and hence could play an important role in the evolutions of the FZ structures (e.g., Ben-Zion and Sammis 2003; Ma 2008; Finzi et al. 2009; Cochran et al. 2009) and near-surface layers. Such permanent change, however, may be a very subtle signal for one or a few mainshocks. Repeating earthquakes throughout the earthquake cycle (or at least before and after the mainshock) are needed to detect such changes (e.g. Schaff and Beroza 2004).

In summary, our observations are consistent with the widespread damages in the top few hundred meters of the shallow crust (Rubinstein et al. 2004a, 2005; Peng and Ben-Zion 2006), and localized temporal changes in and around active FZs at seismogenic depths (Schaff and Beroza 2004; Li et al. 2006; Rubinstein et al. 2007; Taira et al. 2008). These results also support the numerical simulations of widespread damages in the near surface and localized damages around active FZs at depth (Ma 2008; Finzi et al. 2009). Recent studies have also shown that shaking induced damages may offer an explanation for dynamic triggering of earthquakes (Johnson and Jia 2005), and generations of high-frequency extreme ground motions in the near surface layers (Fischer et al. 2008; Sleep and Ma 2008). Hence, systematic observations of temporal changes from repeating earthquakes not only provide additional evidence of widespread nonlinearity during strong ground motions, but also offer new insight into the long-term evolutions of FZ structures and interactions of earthquakes and faults.

3.6 Appendix: Estimation of Temporal changes of a three-media fault model using synthetic seismograms

To evaluate the ability of inferring the depth extent of the damage zone, we measure temporal changes from synthetic seismograms generated by SH-type dislocations at different depths inside a low-velocity FZ layer (Figure 3.A1) sandwiched between a half space (HS). We use the 2D analytical solution of Ben-Zion and Aki (1990) and Ben-Zion (1998) to calculate the synthetic waveforms. The initial FZ model parameters are: FZ width $W = 100$ m, S-wave velocities in the FZ and the half space $\beta_{\text{FZ}} = 1.5$ km/s and $\beta_{\text{HS}} = 3.0$ km/s, and quality factors in the FZ and the half space $Q_{\text{FZ}} = 50$ and $Q_{\text{HS}} = 1000$. The densities of rocks are set to be 2.7 g/cm^3 for different layers. The station is placed in the middle of the FZ at the free surface (i.e., 50 meters to the left boundary of the FZ). The shear dislocation sources are placed along the left boundary of the FZ from 1 to 10 km at depth with inter-event spacing of 1 km (Figure 3.A1). To simulate the velocity reduction inside the FZ, we change β_{FZ} to be 1.4925 km/s (i.e., 0.5% reduction) and keep $\beta_{\text{HS}} = 3.0$ km/s to be the same.

We use the same procedure as described in Section 3.3 to measure temporal changes for events at different depths (Figure 3.A2), except slight difference in the following two parameters. First, we first band-pass filtered the seismograms at 1-10 Hz, rather than 1-20 Hz, in order to remove potential high-frequency noise generated by the synthetic code. In addition, we use 0.5-s time window, instead of 1-s window to measure the temporal changes. The primary reason is that the duration of the synthetic FZ trapped waves is less than 1 s for events at depth smaller than 3 km. Hence, a smaller time window is needed to quantify the subtle changes in the time delays.

the slope measured from the time delays tends to be a constant value for those deeper events. It is interesting to note that most slopes (from events deeper than 2 km) are less than 0.5% and decrease with depths. This is because that the measured slopes reflect a combined effect of velocity reduction within the FZ (0.5%) and the host rocks (0%). As an event occurs deeper, more seismic energy will travel through the host rocks, efficiently decreasing measured velocity reduction (i.e., slope). This observation is similar to those found by Haney et al. (2009) for small velocity changes within volcanic conduits. Because the median delay times increase systematically with depth, while the slopes do not, we conclude that median delay-time values provide a better way to infer the relationship between temporal changes and hypocentral depths.

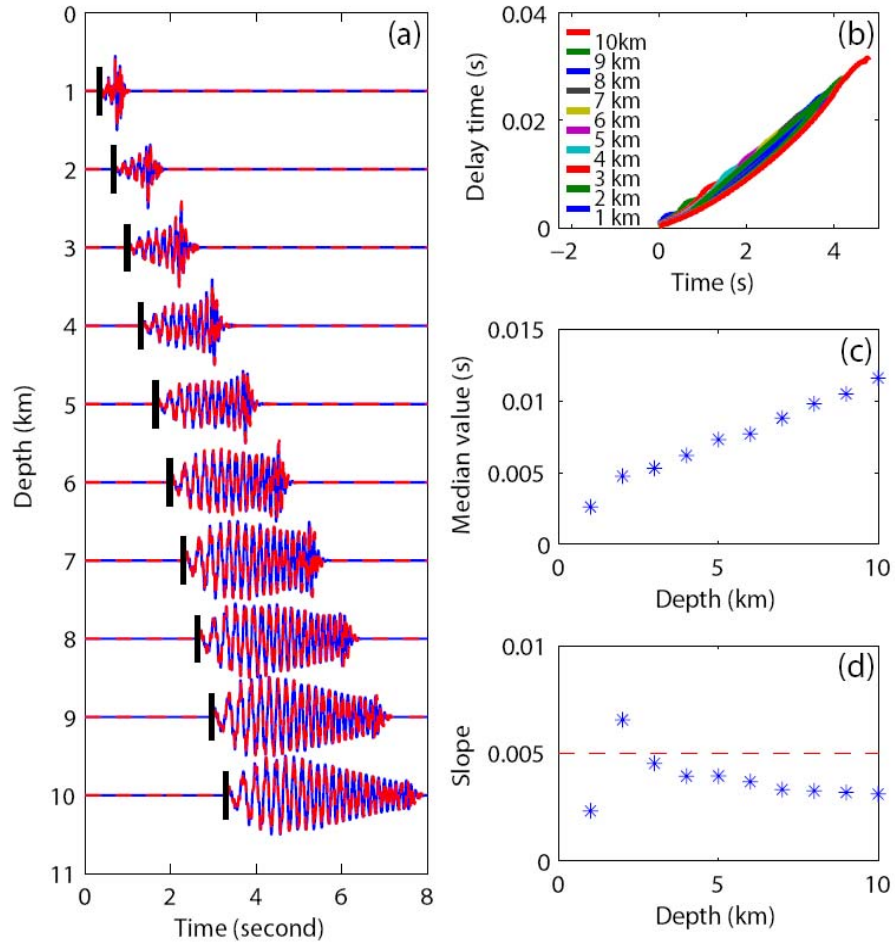


Figure 3.A2. (a) Synthetic waveforms generated at different depths. Original traces and seismograms after velocity-reduction in the fault zone are marked by the blue solid lines and red dashed lines, respectively. The first arrivals of S-waves arrival are marked by the black vertical lines. (b) Calculated delay-time $\tau(t)$ of events at different depths. All traces are aligned relative to the first arrivals of S-waves of the corresponding waveforms. (c) Median values of calculated delay-time $\tau(t)$ in (b) vs. depths. The median values are calculated from a time-window ranging from the first S-arrival to the end of FZ trapped waves. (d) The calculated slopes of delay-time $\tau(t)$ in (b) vs. depths. The slope is calculated at a 0.7-s time window starting from first S-arrivals. The horizontal red dashed line marks the theoretical value of slope in case of homogeneous velocity-reduction of 0.5%.

CHAPTER 4

DETECTING REMOTELY TRIGGERED TEMPORAL CHANGES AROUND THE PARKFIELD SECTION OF THE SAN ANDREAS FAULT

Summary

The work in this chapter is published in Zhao et al. (2010b). Detecting temporal changes in fault zone properties at seismogenic depth has been a long-sought goal in the seismological community for many decades. Recent studies based on waveform analysis of repeating earthquakes have found clear temporal changes in the shallow crust and around active fault zones associated with the occurrences of large nearby and teleseismic earthquakes. However, repeating earthquakes only occur in certain locations and their occurrence times cannot be controlled, which may result in inadequate sampling of the interested regions or time periods. Recent developments in passive imaging via auto- and cross-correlation of ambient seismic wavefields (e.g. seismic noise, earthquake coda waves) provide an ideal source for continuous monitoring of temporal changes around active fault zones. Here we conduct a systematic search of temporal changes along the Parkfield section of the San Andreas Fault by cross-correlating relatively high-frequency (0.4-1.3 Hz) ambient noise signals recorded by 10 borehole stations in the High Resolution Seismic Network. Using both stretch/compressed and moving-window cross-correlation techniques to measure the delay time and the decorrelation-index between the daily Noise Cross-Correlation Functions (NCCFs), we find clear temporal changes in the median seismic velocity and decorrelation-index associated with the 2004 M6.0 Parkfield

earthquake. We also apply the same procedure to the seismic data around four regional/teleseismic events that have triggered non-volcanic tremor in the same region, but failed to find any clear temporal changes in the daily NCCFs. The fact that our current technique can detect temporal changes from the nearby but not regional and teleseismic events, suggest that temporal changes associated with distance sources are very subtle or localized so that they could not be detected within the resolution of the current technique ($\sim 0.2\%$).

4.1 Introduction

As was described in Chapter 3, measuring temporal variations within active fault zones (FZs) has important implications for many aspects of earthquake physics. Many early studies of temporal changes based on travel times from natural earthquakes or scattering properties of coda waves were generally not convincing, mostly because of the mixing of spatial variations in the source with actual temporal changes occurring in the medium (e.g., Liu et al 2004; Peng and Ben-Zion 2005). Recent studies based on waveform analysis of repeating earthquakes or repeatable controlled sources have found clear temporal changes of seismic velocities in shallow surface layers and around active FZs associated with the occurrences of nearby major earthquakes (e.g. Poupinet et al. 1984; Li et al. 1998, 2006; Matsumoto et al. 2001; Vidale and Li 2003; Niu et al. 2003, 2008; Schaff and Beroza 2004; Rubinstein and Beroza 2004a, b, 2005; Peng and Ben-Zion 2006; Rubinstein et al. 2007a; Silver et al. 2007; Taira et al. 2008; Chao and Peng 2009; Zhao and Peng 2009).

While these studies mostly focus on temporal changes caused by earthquakes in the near field (i.e., within 1-2 fault rupture length), a recent study based on waveform

analysis of repeating earthquakes has observed clear temporal changes around the Parkfield section of the San Andreas fault (SAF) induced by the dynamics stresses from the surface waves of the 2004 M_W 9.2 Sumatra and the 1992 M_W 7.3 Landers earthquakes (Figure 4.1, Taira et al. 2009). They suggested that large earthquakes like the 2004 Sumatra earthquake could produce a global change of the Earth's fault systems, and such temporal changes may explain long-range and temporal clustering of global seismicity (e.g. Kanamori 1977; Mogi 1979; Parsons 2002). This is also consistent with recent observations of remotely triggered earthquakes (e.g. Hill et al. 1993; Gomberg et al. 2001, 2004; Hough and Kanamori 2002; Prejean et al. 2004; Hill and Prejean 2007; Velasco et al. 2008; Peng et al. 2010) and non-volcanic tremor (Miyazawa and Brodsky 2008; Gomberg et al. 2008; Miyazawa et al. 2008; Rubinstein et al. 2007b, 2009; Peng and Chao. 2008; Peng et al. 2008, 2009; Guilhem et al. 2010) following the occurrences of large shallow earthquakes. In particular, several recent studies have found that many large regional and teleseismic events in the past ten years, including the 2004 Sumatra earthquake, have triggered clear tremor around the Parkfield section of the SAF (Peng et al. 2008, 2009; Guilhem et al. 2010). It is still not clear whether other large earthquakes besides the Sumatra event also cause temporal changes around Parkfield.

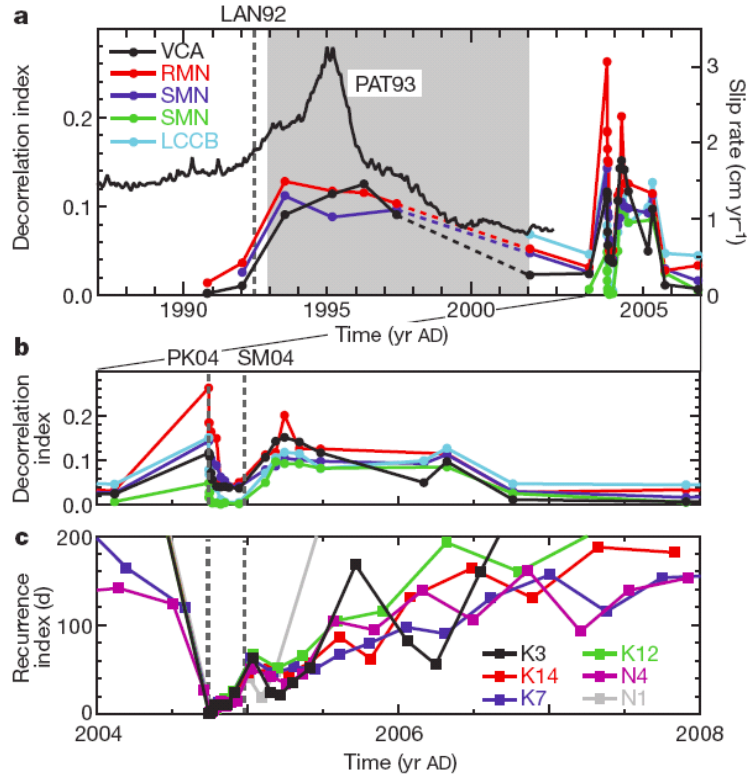


Figure 4.1. Changes of decorrelation index of repeating clusters in the Parkfield section of the SAF after the 2004 great Sumatra earthquake (from Taira et al. 2009).

Recently, Johnson and Jia (2005) performed laboratory dynamic experiments on granular media, and found that seismic waves could reduce the shear modulus and weaken the fault further, resulting in triggered brittle failure. Their results suggested that dynamically weakened FZ could produce both triggered seismic activity and temporal changes in material properties that are in principle observable through seismic methods. Because repeating earthquakes only occur in certain locations and their occurrence times cannot be controlled, this may result in inadequate or poor sampling of the interested regions or time periods. The aforementioned Sumatra case (Taira et al. 2009) is rather unique because of the occurrence of the 2004 M_w 6.0 Parkfield earthquake, which has changed the occurrence pattern of many set of repeating clusters (Lengliné and Marsan

2009) and hence provide enough sampling points around the subsequent Sumatra earthquake. However, repeating earthquakes may not be enough to detect temporal changes associated with other teleseismic events that occurred either before or long after the 2004 Parkfield earthquake.

Recent developments in passive imaging via auto- and cross-correlating of ambient seismic wavefields provide an exciting opportunity for mapping spatio-temporal variations of the Earth's properties with unprecedented temporal and spatial resolutions (e.g. Sabra et al. 2005a, b, 2006; Shapiro et al. 2005; Gerstoft et al. 2006; Sens-Schönfelder and Wegler 2006; Brenguier et al. 2008a, 2008b; Ohmi et al. 2008; Wegler et al. 2009; Xu and Song 2009; Chen et al. 2009; Cheng et al. 2010). The basic idea is that cross-correlation or deconvolution of diffuse seismic wavefields (e.g., ambient seismic noises, earthquake coda waves) recorded at two stations results in the Empirical Green's Function (EGF) between them (Figure 4.2). Because ambient wavefields exist at all the time in many regions, they provide an ideal source for continuous monitoring of the temporal changes of material properties in the upper crust. However, for most applications, the actual ambient vibration fields recorded on the structure of interest will likely be not fully diffuse. In this case, there is no formal guarantee that the NCCF, or the EGF, would yield an unbiased estimate of the actual Green's Function. But if the goal is to just passively monitor the Earth's properties using this cross-correlation technique (e.g. for FZ monitoring), then the only condition is the relative temporal stability of the ambient noise source, even if the NCCF waveform differs from the actual Green's Function (Hadziioannou et al. 2009).

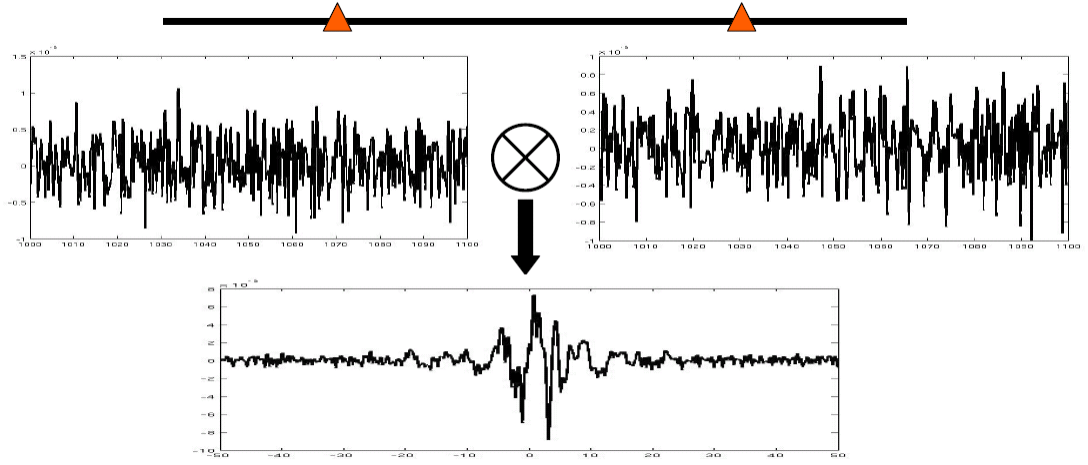


Figure 4.2. An illustration of ambient noise cross-correlation technique. Two segments of seismic noises are recorded at two stations marked as red triangles. The cross-correlation of these two noise records results in empirical Green function at the bottom.

Recently, Brenguier et al. (2008b) applied this technique to the Parkfield region and detected a clear reduction of seismic velocities in the Parkfield section of the SAF associated with the 2003 M_W 6.5 San Simeon and the 2004 M_W 6.0 Parkfield earthquakes. Motivated by their success, here we apply the same technique to examine the temporal changes associated with several large regional and teleseismic events that have triggered tremor around Parkfield (Peng et al. 2008, 2009; Guilhem et al. 2010). Because we expect that the temporal changes associated with teleseismic events would be subtle and probably transient, we use slightly higher frequency bands (0.4-1.3 Hz) that are more sensitive to subtle changes, and do not use the 30-day smooth window as was done in the previous study (Brenguier et al. 2008b). We also apply the same technique around the 2004 Parkfield earthquakes to prove its effectiveness. In the next two sections, we first introduce the analysis procedure to compute the daily EGF, followed by the methods to measure temporal changes. The results are presented in Section 4.4 and further discussed in Section 4.5.

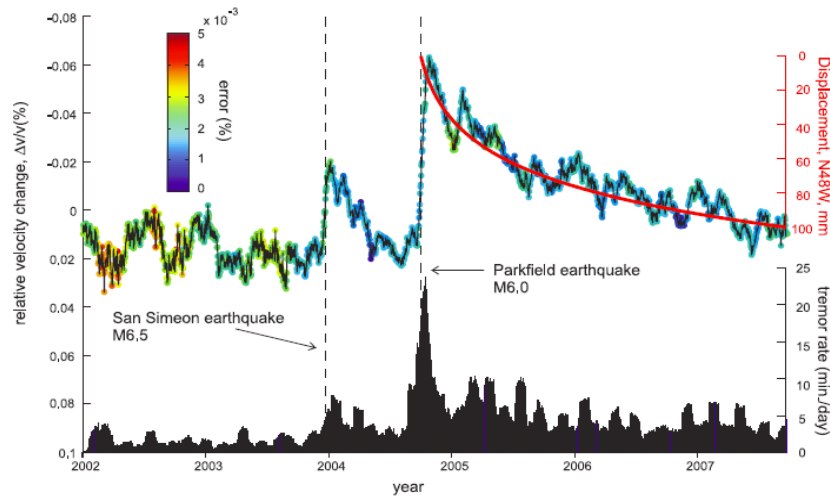


Figure 4.3 Seismic velocity changes, surface displacements from GPS, and tremor activity near Parkfield. The red curve represents the postseismic fault-parallel displacements along the San Andreas Fault as measured by a GPS station near Parkfield (from Brenguier et al. 2008b).

4.2 Data and Analysis Procedure

The SAF is a right-lateral strike-slip fault that extends approximately 1200 km along the boundary between the Pacific and the North American plates. The Parkfield section of the SAF straddles the transition between the creeping segment of the fault to the NW and the locked segment to the SE (Figure 4.4). This region is well instrumented and studied, mostly due to the Parkfield Earthquake Prediction Experiment project (Bakun and Lindh 1985) and the recent San Andreas Fault Observatory at Depth (SAFOD) experiment (Hickman et al. 2004). In this work, we use the continuous seismic data recorded at the High Resolution Seismic Network (HRSN) around the Parkfield section of the SAF to compute the daily EGF. The HRSN is composed of 13 borehole stations with depth ranges from about 60 to 600 meters below the surface, and is recorded in continuous mode since 2001. We use the 20 samples/s data recorded at the 10 borehole stations (excluding JCSB, VARB, and GHIB). Stations JCSB and VARB have different

instrument response with the remaining stations. In addition, the computed EGFs between station GHIB and the other stations are not very stable, probably because of the relatively large inter-station distance that is perpendicular to the noise propagation direction from the coastline (Sabra et al. 2005a). Hence, we only focus on the rest 10 stations that are located nearby with the same instrument response. Although the examined frequency range (0.4-1.3 Hz) is slightly below the corner frequency of the instrument response (~ 2 Hz), we did not correct the instrument response to avoid producing artifacts from the deconvolution procedure.

In this study we focus on the four regional and teleseismic events that have triggered tremor in the same region (Peng et al. 2008, 2009; Guilhem et al. 2010). These include the 2002 M_w 7.9 Denali Fault, 2005 M_w 7.2 Mendocino, 2007 M_w 8.1 Kuril Island, and 2009 M_w 6.9 Baja California earthquakes. These events are chosen because they produce among the largest peak ground velocities (PGVs) in the study region (Guilhem et al. 2010). In addition, we also examine data around the 2004 Parkfield earthquake to test the robustness of our method.

The analysis procedure generally follows that of Brenguier et al (2008b) and is briefly described here. First, we obtain the seismic data recorded at those 10 seismic stations at least one month before and after the occurrence date of these 5 events. The continuous records are then cut into one-day-long data, and band-pass filtered from 0.4 to 1.3 Hz. This frequency band is close to the frequency range of the P-wave seismic noise in the Parkfield region driven by distant ocean winds (Zhang et al. 2009), and is slightly higher than that of the typical microseism band of 0.1-0.2 Hz and the range of 0.1-0.9 Hz used by the previous study (Brenguier et al. 2008b). We choose the slightly higher

frequency range because of their relative stability within a short time range (Zhang et al. 2009) and their potential of detecting subtle temporal changes with short inter-station distances.

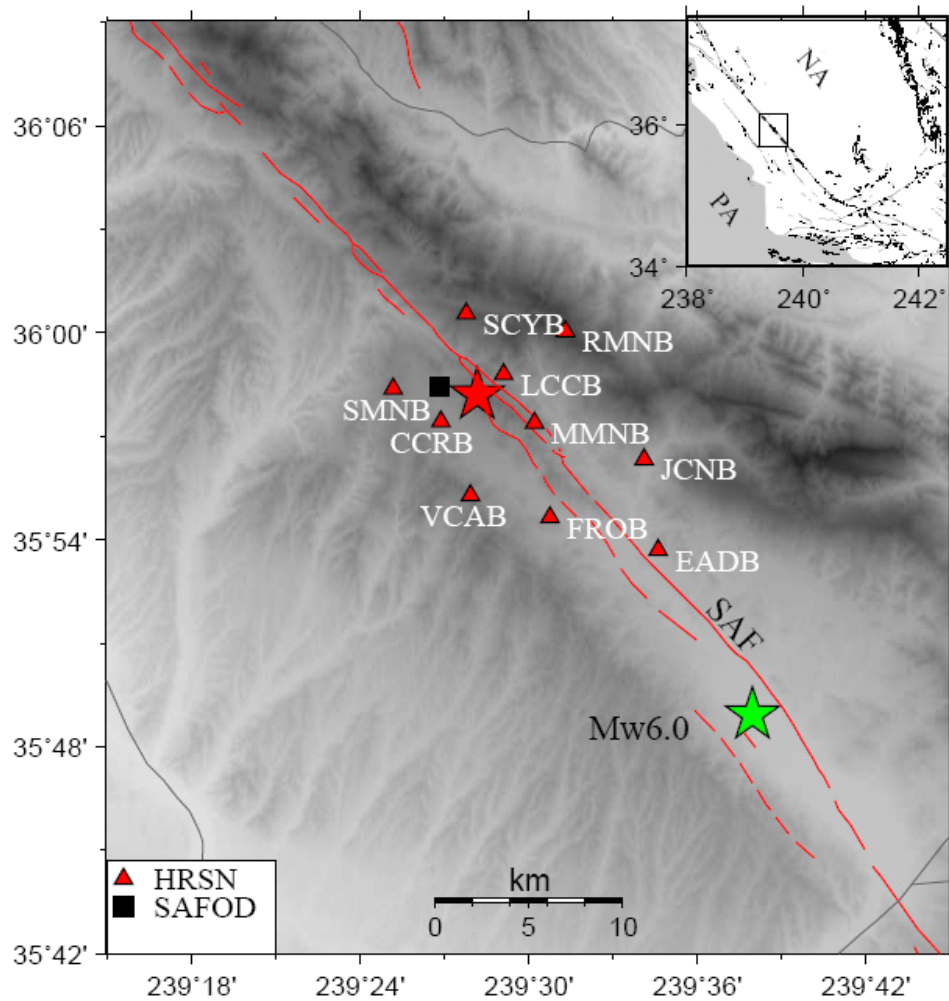


Figure 4.4. A map of the Parkfield section of the San Andreas Fault (SAF). The epicenters of the 1966 and 2004 M6 Parkfield earthquakes are marked with red and green stars, respectively. The red lines denote surface traces of faults. Red triangles mark the locations of 10 seismic stations of High Resolution Seismic Network (HRSN) used in this study. The background is shaded topography with white being low and dark being high. The inset shows the area on a map of California. SAF: the main San Andreas fault; NA: North American Plate; PA: Pacific Plate; SAFOD: San Andreas Fault Observatory at Depth.

After the filtering process, we use a constant threshold to reduce the effect of large events and spurious instrument noises. The threshold at each station is calculated as the median value of the standard deviations of the daily-long seismic records within two months for each event. Any data point with amplitude larger than the threshold was assigned the threshold value. We also tested different values of the threshold and found that the obtained daily EGFs are not very sensitive to such choice. Next, we compute the Fast Fourier Transform (FFT) of the daily-long seismic records. Then we equalize the amplitudes of spectrum to be ones while keep their phases in the frequency domain, which is also named as “whitening” spectrum (Breguier et al. 2008a, 2008b). Finally, we cross-correlate the whitened spectrum between all possible station pairs in the frequency domain and then compute the inverse FFT to obtain the daily EGF in the time domain. Figure 4.5 illustrates an example of daily EGFs between stations CCRB and MMNB one month before and after the 2004 Parkfield earthquake. Except a few days, the obtained daily EGFs show high similarity up to 20 s, suggesting that they are stable enough for measuring temporal changes.

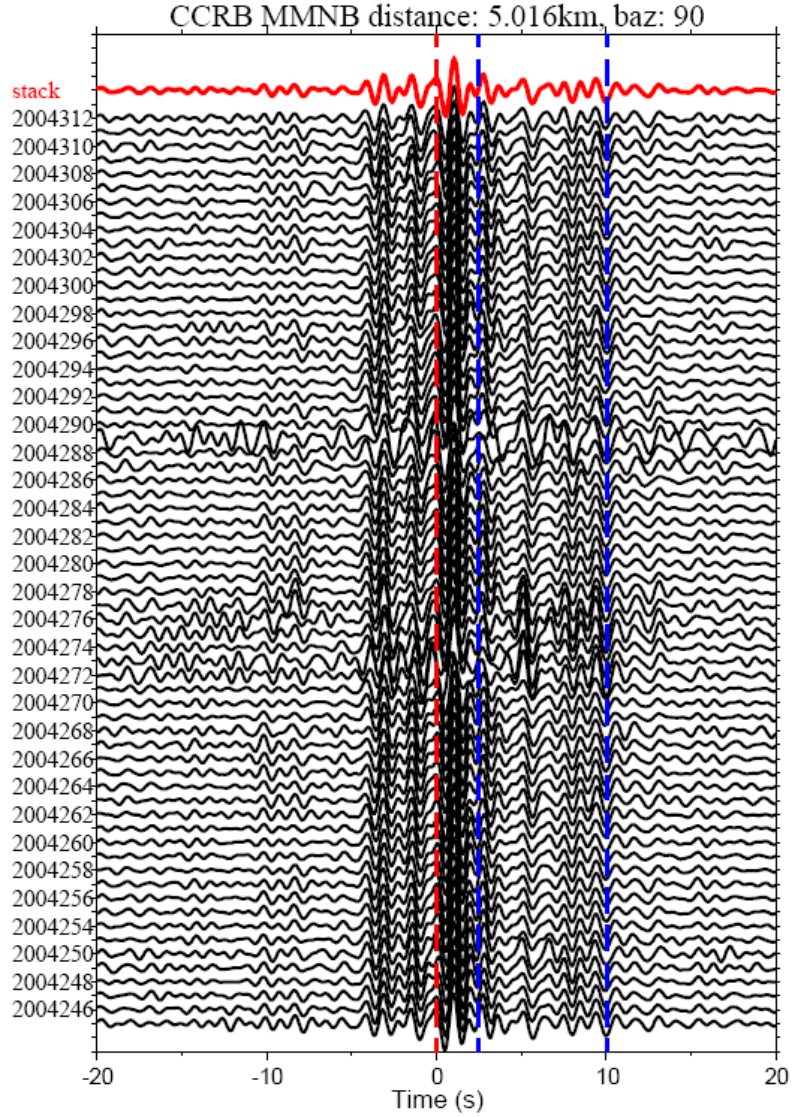


Figure 4.5. Waveforms of the daily Empirical Green Functions (EGFs) between the station pair CCRB and MMNB before and after the 2004 M6 Parkfield earthquake. The corresponding date of waveforms is labeled in the left (4-digit-year, 3-digit-Julian day) and the stacked reference trace is shown on the top in red. The vertical red dashed line and two vertical blue lines mark the time zero and time window to calculate the temporal changes, respectively. Inter-station distance and azimuth are labeled on the top.

4.3 Measuring Temporal Changes from EGFs

To simplify the next analysis step, we consider the two-month daily EGFs around each target event as an individual group. For a pair of stations within each group, we first

stack all daily EGFs and use that as the reference trace (Figure 4.5). Next, we measure the subtle changes between these daily EGFs and the reference within a fixed time window (Wegler et al. 2009). The beginning of each time window is set to be $\pm l / v$, where l is the inter-station distance and v is the assumed seismic velocity, and the plus and minus signs correspond to the positive and negative time axis, respectively. The velocity is set to be 3 km/s, which is slightly lower than the direct P-wave velocity in this region (Zhang et al. 2009). In this way, the direct arrivals of the EGFs, which is more affected by seasonal variations (Breguier et al, 2008b), are not included in measuring temporal changes.. The length of the time window is determined based on a data-adaptive method using the correlation index d for a pair of stations as

$$d = \frac{(\sum s(t))^2}{N \sum s^2(t)}, \quad (4.1)$$

where $s(t)$ is the daily EGF, and N is the total number of daily EGFs. A large correlation index corresponds to time window with high waveform similarity and large Signal-to-Noise Ratio (SNR). In this study, we choose the time window with the correlation index d larger than 0.95.

After selecting the time window for each station pair, we employ two methods to measure the temporal changes. The first method treats the daily EGF as the stretched or compressed version of the reference waveform (Poupinet et al. 1984; Snieder et al. 2002; Breguier et al. 2008b; Wegler et al. 2009). The percentage of seismic velocity change is calculated from the slope of time delay/advance (dt) vs. time (t) as

$$dv / v = -dt / t. \quad (4.2)$$

Following Wegler et al (2009), each daily EGF was stretched and compressed using a grid search with 10,000 trials between -3% and 3% to estimate the parameter dv/v from Equation (4.2). For each trial of the grid search, we computed the correlation coefficient R between the reference trace and the stretched or compressed daily EGF in the fixed time window as discussed before. The best-fitting velocity change is assigned to be the one associated with the largest R (Figure 4.6). Finally, we compute the median value from all possible station pairs (with a minimum of 10 pairs) for each day and use it as a measure of velocity change in our study region.

In the second method, we apply a sliding window waveform cross-correlation technique (Niu et al. 2003; Peng and Ben-Zion 2006; Zhao and Peng 2009) to measure the de-correlation index $D(t)$ (defined as one minus the maximum cross-correlation coefficient between two events) of the daily EGF to the reference trace (Figure 4.7). The sliding window is 1-s long starting from -40 s to 40 s with sliding interval of 0.1 s in each step. A cosine taper is applied to each window with 10% of the entire width to reduce the Gibbs' phenomenon (Niu et al. 2003; Peng and Ben-Zion 2006). Next, we compute the median value of the de-correlation index (MDI) within the time window for each station pair. Similar to the estimation of the velocity changes in the first method, the median value of the MDI from all station pairs is used to quantify the temporal changes on that day.

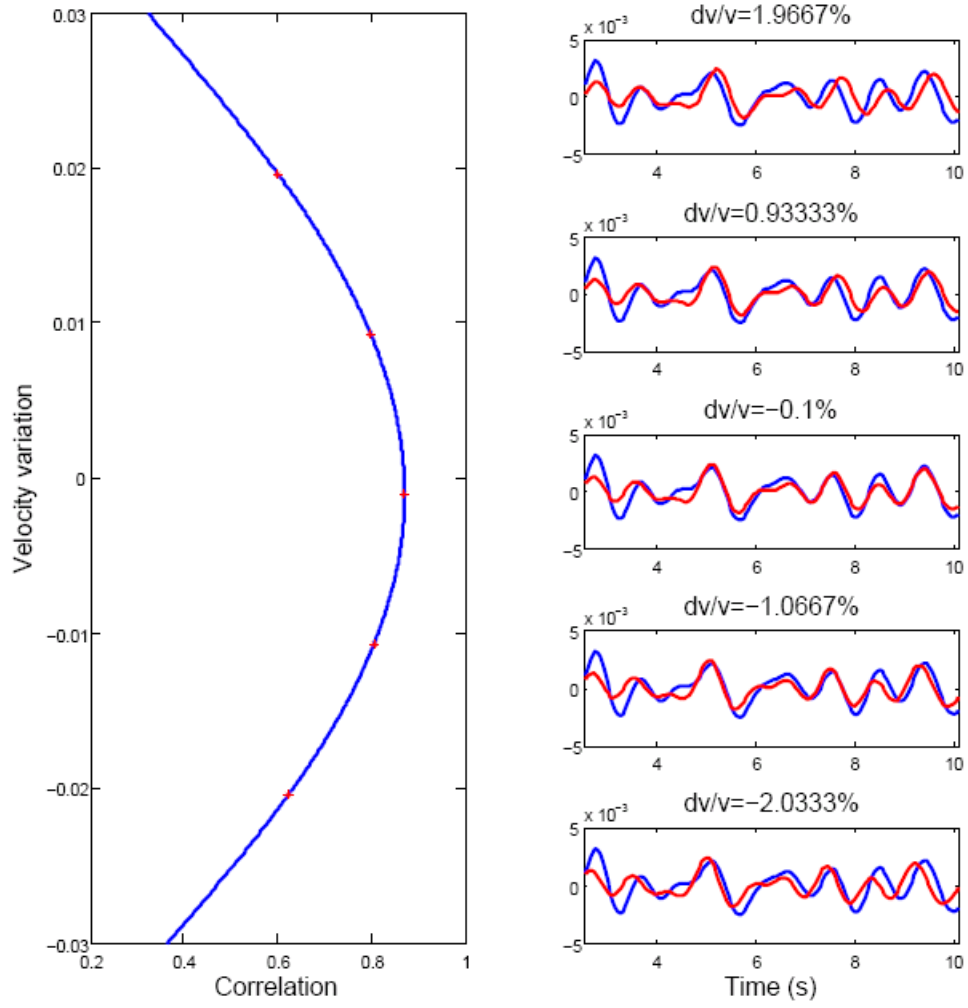


Figure 4.6. An illustration of the stretch/compression method for the seismic trace within the time window on date 2004270 as shown in Figure 4.5. The correlation value between the reference and each stretched/compressed daily EGF is plotted on the left. Blue traces on the right are the reference trace and the red ones represent the stretched or compressed version of daily EGF with the corresponding percentage shown on the top of each panel.

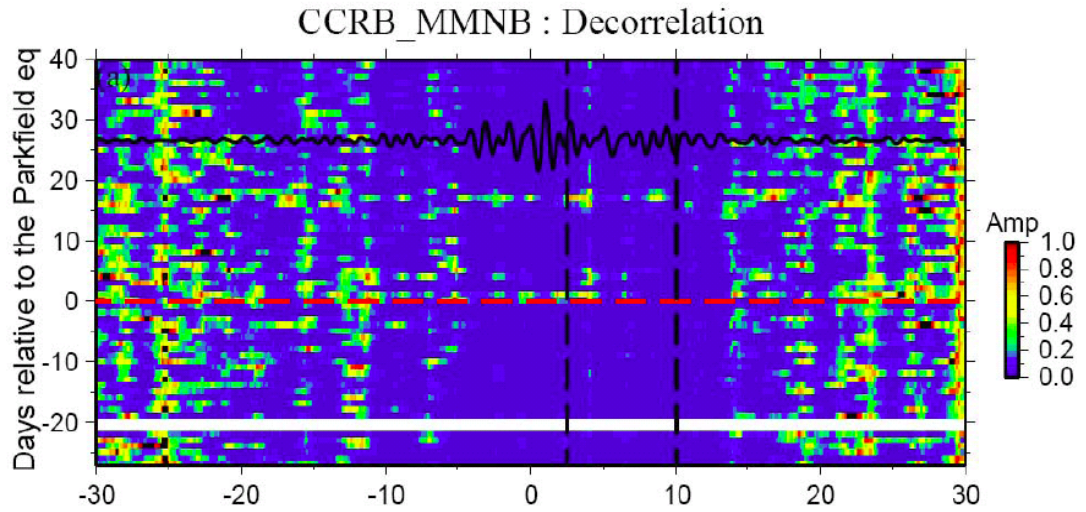


Figure 4.7. An illustration of the de-correlation index method for daily EGFs between the station pair CCRB and MMNB around the 2004 Parkfield earthquake. The colored background shows the de-correlation index of daily EGF with horizontal in time (second) and vertical in dates. The reference trace is shown on the top in black color. Two vertical dashed black lines mark the time window and horizontal red line denotes the occurrence date of the 2004 Parkfield earthquake.

4.4 Results

The median velocity changes and MDIs are plotted at the corresponding day for detecting temporal changes associated with each target event. Figure 4.8 shows the result for the 2004 M6 Parkfield earthquake. Clear reduction of seismicity velocity (up to -0.7%) is observed immediately after the 2004 mainshock, followed by a faster recovery in the first few days and a smaller recovery at later times. The results from the median MDIs also show a sudden increase immediately after the Parkfield mainshock. However, the MDIs recover to the pre-mainshock within the next 1-2 days, faster than the recovery of the seismic velocity changes. In both cases, the largest change is shown not at the same day as the Parkfield mainshock, mostly likely because the mainshock occurred later on that day (2004/09/28 17:57 UTC). Hence the averaged temporal changes on that day are

smaller than the following day. In addition to the co-seismic changes associated with the Parkfield mainshock, there is also a clear change in both the velocity change and de-correlation indexes around 18 days after the mainshock. We have examined nearby and global seismicity, local tremor activity (Nadeau and Guilhem 2009) and precipitation, but failed to find any correlation with the changes at this time.

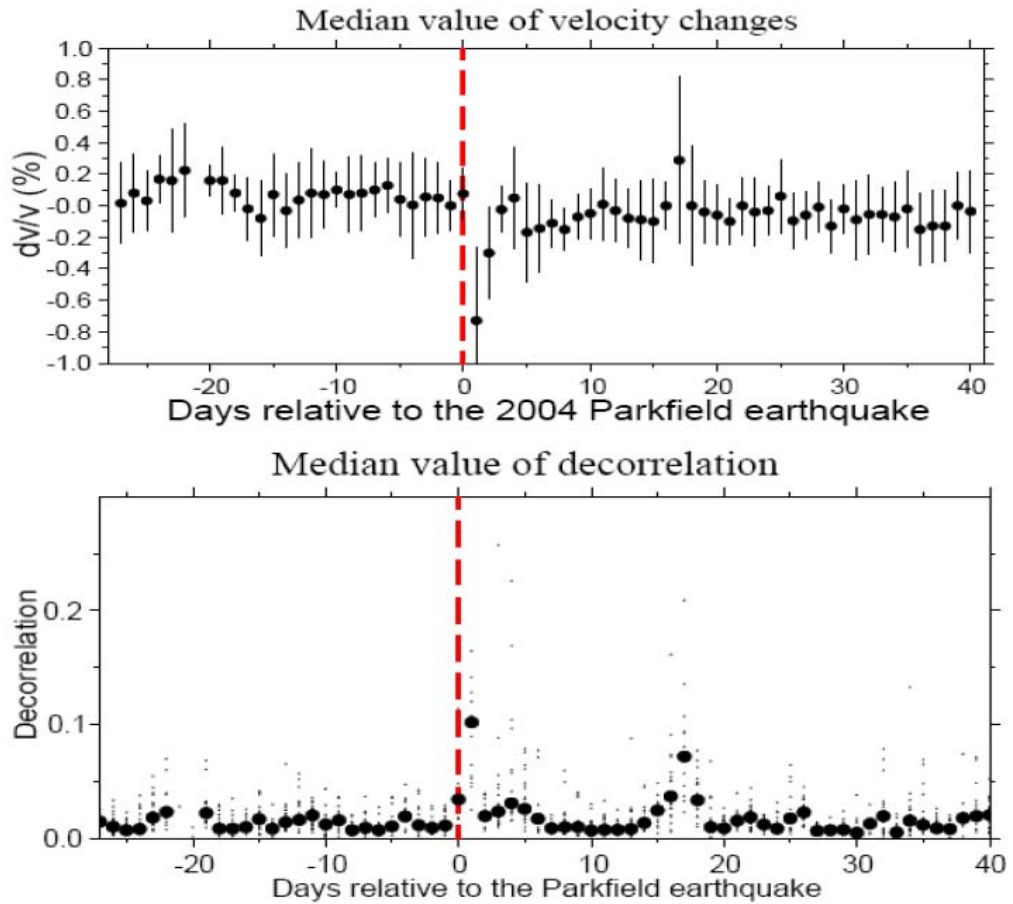


Figure 4.8. (a) Median velocity changes between all possible station pairs versus the occurrence dates relative to the 2004 M6 Parkfield earthquake (the red dashed line). The vertical short black lines represent the median absolute deviations (MAD) of each measurement. (b) Median value of de-correlation index versus the occurrence dates relative to the 2004 M6 Parkfield earthquake. The small black triangles and large black dots mark the de-correlation index from all possible station pairs and their median values for each date, respectively. In both panels, we did not show the daily median values if the available number of station pairs is less than 5 on that day.

Figure 4.9 shows the median velocity changes associated with four regional and teleseismic events that have triggered tremor in the study region. The obtained results show strong fluctuations of velocity changes, especially for the 2002 Denali earthquake, which might be caused by the relatively low SNR before an increase of the pre-amplification gain for the HRSN in 2003 (Brenguier et al. 2008b). In addition, no clear temporal changes in the median velocity changes are observed during the occurrence of these regional and teleseismic events using the stretched method. The median MDI shows a subtle increase around or immediately after the 2002 Denali, 2005 Mendocino, and 2009 Baja California events (Figure 4.10). However, similar or even larger changes are observed at other times in each case. Hence, we conclude that the results obtained from the two methodologies in this article did not reveal any clear and systematic changes associated with these regional and teleseismic events.

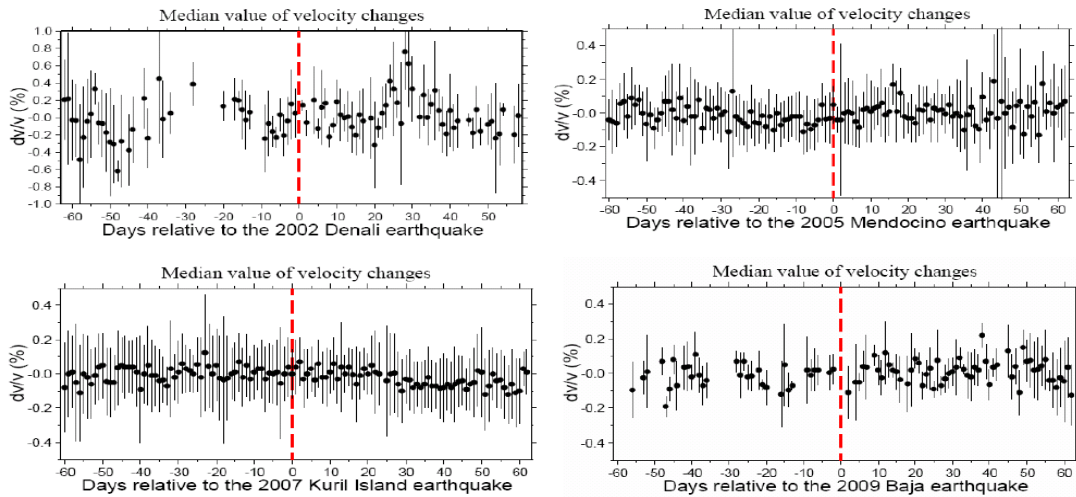


Figure 4.9. Temporal changes in the median velocity changes associated with the four regional/teleseismic events. The name of corresponding event is labeled on the x-axis. Other symbols are the same as Figure 4.8a.

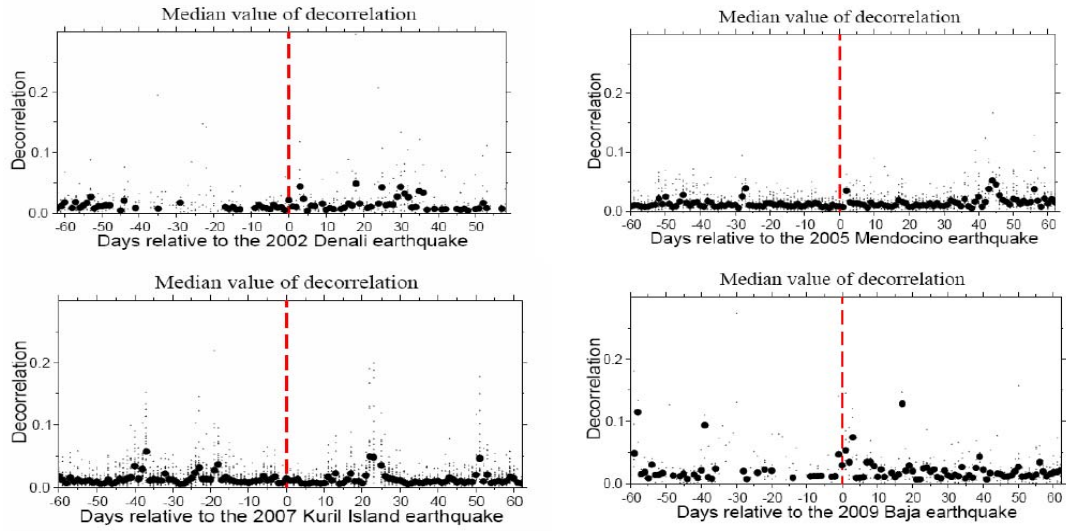


Figure 4.10. Temporal changes in the median de-correlation indexes associated with the four regional/teleseismic events. The name of corresponding indexes is labeled on the x-axis. Other symbols are the same as Figure 4.8b.

4.5 Discussions

In this study, we applied the recent developed noise cross-correlation technique to detect temporal changes around the Parkfield section of the SAF associated with four regional and teleseismic events that have triggered tremor in the same region. However, within the resolution of the current technique, which is $\sim 0.2\%$ based on the average error estimate of the velocity changes, we were unable to detect any clear changes associated with these regional and teleseismic events. There are two possible explanations for such ‘negative’ results. One is that these events are too far to cause any temporal changes. The second is that temporal changes did occur, but are undetected by the current technique. We favor the second explanation for the following reasons.

First, recent studies based on spectral ratio analysis between borehole and surface strong ground motion recordings have shown that modest ground motions on the order of a few tens of gal or less (dynamic strain on the order of 10^{-5}) is able to cause small but

observable temporal changes in the shallow crust, resulting in nonlinear site response (Wu et al. 2010; Rubinstein 2010). The peak ground velocities associated with these regional and teleseismic events are in the range of 0.1–1 cm/s, which correspond to the dynamic strain of 3×10^{-7} – 3×10^{-6} , slightly smaller than the aforementioned threshold for nonlinear ground motion. However, nonlinear effects have been identified in laboratory studies of geomaterials under strains as low as 10^{-8} (TenCate et al. 2004). These results suggest that the regional and teleseismic events could have the potential of causing nonlinear response and small temporal changes in the shallow crust. Other supporting evidence includes hydrological responses (i.e., changes of water table and surface water flows) and eruptions of volcanoes/geysers associated with large nearby and teleseismic earthquakes (e.g., Roeloffs 1998; Manga and Brodsky 2006; Manga and Wang 2007; Wang et al. 2009). Among these studies, Roeloffs (1998) reported coseismic water level rises in a well near Parkfield, California, in response to three local and five distant earthquakes. The changes generally last for days or weeks, and were suggested to be the consequence of increase of coseismic pore pressure near the well. Brodsky et al. (2003) proposed that strong shaking from nearby earthquakes, or large surface waves from teleseismic events, may unclog pre-existing fractures in the shallow crust, resulted in increasing permeability and fluid flow. Finally, as mentioned before, Taira et al. (2009) have found clear changes of deep scatterer and FZ strength associated with the 2004 Sumatra earthquake based on abundant repeating earthquakes in the same region. All these studies support our inference that large regional and teleseismic events could cause temporal changes around active FZs.

To test the robustness of the technique, we also applied it to the 2004 Parkfield mainshock and found clear temporal changes in both the seismic velocities and de-correlation indexes. This is consistent with recent studies in the same region based on waveform analysis of repeating earthquakes (Rubinstein and Beroza 2005; Li et al. 2006; Taira et al. 2008), repeatable control sources (Li et al. 2006), receiver functions (Audet 2010), and noise cross-correlation technique (Brenguier et al. 2008b). However, the reduction in seismic velocity in our study ($\sim 0.8\%$) is larger than that measured from Brenguier et al. (2008b) ($\sim 0.06\%$), but less than those ($\sim 1-4\%$) from repeating earthquakes (e.g., Li et al. 2006). The difference with Brenguier et al. (2008b) mainly stems from their use of 30-day stacking of the daily EGF, which could significantly smooth the co-seismic changes. Similarly, the value of 0.8% obtained in this study is from the 1-day average, while individual repeating earthquakes could sample larger temporal changes immediately after the mainshock.

The relationships between triggered earthquakes and tremor and triggered temporal changes are still not clear at this stage. The fact that our current technique can detect temporal changes from the nearby but not regional and teleseismic events, suggest that temporal changes associated with regional and teleseismic events could be very small, i.e., less than the detection ability of our current technique ($\sim 0.2\%$). This sensitivity can be improved by enhancing the spatial directivity of this cross-correlation process. Indeed, variations in locations of noise sources could result in the change of waveforms of EGFs (Marzorati and Bindi 2008), which could be mapped into temporal changes in the medium. To overcome this problem, many studies use the seismic noise records up to tens of days to balance the distribution of noise sources (e.g., Brenguier et al. 2008b; Xu

and Song 2009). However, this procedure will apparently reduce the resolution of detected temporal changes. Future investigations are planned to assess the use of array analysis (e.g., Rost and Thomas 2002) to select noise sources coming from certain regions before computing EGFs.

It is worth pointing out that most of the triggered tremor did not occur around Parkfield where most of the HRSN stations are located, but further south near Cholame and north in the creeping section of the SAF (Peng et al. 2009). Hence, the station coverage may not be ideal to detect temporal changes associated with the triggered activity. It is also possible that temporal change is localized in certain regions (e.g., high fractural densities or high-fluid pressures). Because we computed the median value of the velocity changes and the de-correlation indexes, this procedure is most sensitive to uniform changes in the medium and could average out potential localized changes. In this case, focusing on the change of a particular phase, similar to that of Niu et al. (2003) and Taira et al. (2009), could help to identify the localized temporal changes induced by these regional and teleseismic events.

In addition, the depth resolution of the observed temporal changes from the ambient noise studies is not well understood (Brenguier et al. 2008b; Xu and Song 2009; Sleep 2009). Based on the correlations between the temporal changes, non-volcanic tremor and afterslip, Brenguier et al. (2008b) proposed that the temporal changes associated with the 2004 Parkfield earthquake are related to postseismic relaxation in the deeper part of the FZ and surrounding region. In comparison, Sleep (2009) suggested that the temporal changes observed by Brenguier et al. (2008b) could also be explained by the rock damage in the near surface layers (e.g., Rubinstein and Beroza 2005). Systematic

studies of the sensitivity kernels of the obtained NCCFs (e.g., Pacheco and Snieder 2006) and the frequency dependent effects of the temporal changes (e.g., Xu and Song 2009) could help to provide further constraints on the depth extent of the observed temporal changes. Finally, it is possible is that the temporal changes is transient, and only occur during the large-amplitude waves, followed by near-instantaneous recovery (e.g. Wu et al. 2010). If so, one has to rely on highly repeatable controlled sources (e.g., Niu et al. 2008) to provide enough temporal samplings before and after the passage of the large-amplitude surface waves.

Cross-correlation of seismic noises has become a useful tool for monitoring temporal changes around active FZs and volcanic regions (e.g., Brenguier et al. 2008a, 2008b). Although our current analysis procedure does not identify any clear temporal changes around the Parkfield section of the SAF associated with four regional and teleseismic events, we feel that with future development it still has the potential of detecting weak temporal changes associated with distant sources.

RECAPITULATION

This thesis aimed at imaging bimaterial interfaces and detecting temporal variations of FZ properties from systematic analyses of large seismic data sets recorded along two active strike-slip faults in California. In the first part of this thesis (Chapters 1 and 2), clear FZHWs are observed along the Parkfield section of SAF and the central Calaveras fault, indicating the existing of sharp velocity contrasts along fault interfaces. Chapters 3 and 4 focus on studying temporal changes of the FZ properties associated with large nearby earthquakes and teleseismic events using repeating earthquakes (Chapter 3) and ambient noises cross-correlation technique (Chapter 4).

The results clearly demonstrate that major strike-slip faults are characterized by well-defined bimaterial interface imbedded within a wedge-shaped low-velocity zone (e.g. Ben-Zion and Sammis 2003). The fault interface likely extends at least to the bottom of the seismogenic zone, as inferred from the persistent moveout of FZHW with depth. In addition, clear along-strike variations of velocity contrasts are found in both regions, and the obtained first-order velocity contrasts are generally consistent with surface geology and 3D seismic tomography. The existence of such variations in bimaterial interface may provide important clues on segmentations and rupture directivities of large earthquakes on mature strike-slip faults (e.g. Ben-Zion 2006).

In comparison, the regions that show clear velocity reductions following nearby large earthquakes are most prominent in the top few kilometers around active FZs and in the top few hundred meters away from the FZs. The result is consistent with the hierarchical wedge-shape FZ structure as inferred from recent seismic refraction

experiments (Blümling et al. 1985; Mooney and Colburn 1985), tomography studies (e.g., Michael 1988), FZ trapped waves (Rovelli et al. 2002; Ben-Zion et al. 2003; Peng et al. 2003), and near-fault crustal anisotropy (Cochran et al. 2003, 2006; Peng and Ben-Zion 2004; Liu et al. 2008; Zhang et al. 2007). Such a wedge-shape low-velocity zone is expected to produce significant local amplification effects (Cormier and Spudich 2001; Spudich and Olsen 2001; Rovelli et al. 2002). Hence it is more susceptible for further damages in material strength from strong shakings of nearby large earthquakes, resulting in larger time delays as observed from repeating earthquakes. This positive feedback between the formations of damage zones and structures of FZs together with preferred rupture directions inferred from bimaterial fault interfaces (Ben-Zion 2001; 2006) could provide important information for seismic hazard mitigation.

In addition to large earthquakes in the same fault, clear increase of delay time was found following the 1986 Mt. Lewis earthquake and the 1989 Loma Prieta earthquake, suggesting that strong shakings from large earthquakes at regional distances could also produce damages in the shallow crust and within active FZs. Recent observations of remote triggering of tremor and seismicity (e.g. Hill and Prejean 2007) indicate alternative ways to perturb a FZ even with quite small dynamic stresses, which has been long ignored by seismological community due to limitation of high-quality dataset. Availability of huge-volume continuously-recorded digital seismograms in the recent years provides a great opportunity for seismologists to detect subtle temporal changes around active FZs. Using cross-correlations of ambient seismic noises, Brenguier et al. (2008b) suggests a relation between the reductions of seismic velocity and coseismic damage at shallow FZ and stress changes at depth after large local earthquakes. Chapter 4

extends their work but focusing on subtle temporal changes around the Parkfield section of the SAF caused by large distant earthquakes. The technique successfully detected temporal changes associated with the 2004 Parkfield earthquake, but no clear changes were found for 4 regional and teleseismic events that have triggered tremor in the same region. It is likely that temporal changes associated with distance sources are very subtle or localized so that they could not be detected within the resolution of the current technique ($\sim 0.2\%$). Further studies are needed to improve the stability and resolution of this technique so that it can be applied to provide long-term monitoring of active FZs and volcanoes.

REFERENCES

- Abercrombie, R.E., 1996. The magnitude-frequency distribution of earthquakes recorded with deep seismometers at Cajon Pass, southern California, *Tectonophysics*, 261, 1–7.
- Adams, G.G., 1995. Self-excited oscillations of two elastic half-spaces sliding with constant coefficient of friction, *J. Appl. Mech.*, 62, 867–872.
- Aki, K., 1969. Analysis of seismic coda of local earthquakes as scattered waves, *J. Geophys. Res.*, 74, 615–631.
- Aki, K., 1985. Theory of earthquake prediction with special reference to monitoring of the quality factor of lithosphere by the coda method, *Earthq. Pred. Res.*, 3, 219 – 230.
- Aki, K. and Chouet, L.B., 1975. Origin of coda waves: Source, attenuation, and scattering effects, *J. Geophys. Res.*, 80, 3322 – 3342.
- Aki, K. and Richards, P.G., 2002. *Quantitative Seismology* (second edition), University Science Books, Sausalito, CA.
- Ampuero, J.-P. and Ben-Zion, Y., 2008. Cracks, pulses and macroscopic asymmetry of dynamic rupture on a bimaterial interface with velocity-weakening friction, *Geophys. J. Int.*, 173 (2), 674–692, doi:10.1111/j.1365-246X.2008.03736.x.
- Andrews, D.J. and Ben-Zion, Y., 1997. Wrinkle-like slip pulse on a fault between different materials, *J. Geophys. Res.*, 102, 553–571.
- Audet, P. 2010. Short Note Temporal variations in crustal scattering structure near Parkfield California, using receiver functions, *Bull Seismol Soc Am*, 100, 1356–1362, doi: 10.1785/0120090299.
- Baisch, S. and Bokelmann, G.H.R., 2001. Seismic waveform attributes before and after the Loma Prieta earthquake: Scattering change near the earthquake and temporal recovery, *J. Geophys. Res.*, 106(B8), 16,323–16,337.

- Bakun, W.H. and Lindh, A.G., 1985. The Parkfield, California, earthquake prediction experiment, *Science*, 229, 619–624.
- Bakun, W.H., Clark, M.M., Cockerham, R.S., Ellsworth, W.L., Lindh, A.G., Prescott, W.H., Shakal, A.F. and Spudich, P., 1984. The 1984 Morgan Hill, California, earthquake, *Science*, 225, 288 - 291, doi: 10.1126/science.225.4659.288.
- Bakun, W.H., Aagaard, B., Dost, B., Ellsworth, W.L., Hardebeck, J.L., Harris, R.A., Ji, C., Johnston, M.J.S., Langbein, J., Lienkaemper, J.J., Michael, A.J., Murray, J.R., Nadeau, R.M., Reasenberg, P.A., Reichle, M.S., Roeloffs, E.A., Shakal, A., Simpson, R.W. and Waldhauser, F., 2005. Implications for prediction and hazard assessment from the 2004 Parkfield earthquake, *Nature*, 437, 969–974, doi: 10.1038/nature04067.
- Ben-Zion, Y., 1989. The response of two joined quarter spaces to SH line sources located at the material discontinuity interface, *Geophys. J. Int.*, 98, 213–222.
- Ben-Zion, Y., 1990. The response of two half spaces to point dislocations at the material interface, *Geophys. J. Int.*, 101, 507-528.
- Ben-Zion, Y., 1998. Properties of seismic fault zone waves and their utility for imaging low velocity structures, *J. Geophys. Res.*, 103, 12567-12585.
- Ben-Zion, Y., 2001. Dynamic ruptures in recent models of earthquake faults, *J. Mech. Phys. Solids*, 49, 2209–2244.
- Ben-Zion, Y., 2003. Appendix 2, Key Formulas in Earthquake Seismology, in *International Handbook of Earthquake and Engineering Seismology*, eds. W.H.K. Lee, H. Kanamori, P.C. Jennings, and C. Kisslinger, Part B, 1857-1875, Academic Press.
- Ben-Zion, Y., 2006. A comment on “Material contrast does not predict earthquake rupture propagation direction” by R. A. Harris and S. M. Day, *Geophys. Res. Lett.*, 33, L13310, doi:10.1029/2005GL025652.
- Ben-Zion, Y. and Aki, K., 1990. Seismic radiation from an SH line source in a laterally heterogeneous planar fault zone, *Bull. Seism. Soc. Am.*, 80, 971-994.

- Ben-Zion, Y. and Andrews, D.J., 1998. Properties and implications of dynamic rupture along a material interface, *Bull. Seismol. Soc. Am.*, 88, 1085–1094.
- Ben-Zion, Y. and Huang, Y., 2002. Dynamic rupture on an interface between a compliant fault zone layer and a stiffer surrounding Solid, *J. Geophys. Res.*, 107(B2), doi:10.1029/2001JB000254.
- Ben-Zion, Y. and Malin, P., 1991. San Andreas fault zone head waves near Parkfield, California, *Science*, 251, 1592–1594.
- Ben-Zion, Y. and Sammis, C.G., 2003. Characterization of fault zones, *Pure Appl. Geophys.*, 160, 677-715.
- Ben-Zion, Y., Katz, S. and Leary, P., 1992. Joint inversion of fault zone head and direct P arrivals for crustal structure near major faults, *J. Geophys. Res.*, 97, 1943–1951.
- Ben-Zion, Y., Peng, Z., Okaya, D., Seeber, L., Armbruster, J.G., Ozer, N., Michael, A.J., Baris, S. and Aktar, M., 2003. A shallow fault zone structure illuminated by trapped waves in the Karadere-Duzce branch of the north Anatolian fault, western Turkey, *Geophys. J. Int.*, 152, 699-717, doi: 10.1046/j.1365-246X.2003.01870.x.
- Beresnev, I.A. and Wen, K.-L., 1996. Nonlinear soil response—a reality?, *Bull. Seismol. Soc. Am.*, 86, 1964 - 1978.
- Beroza, G.C. and Spudich, P., 1988. Linearized inversion for fault rupture behavior: Application to the 1984, Morgan Hill, California, earthquake, *J. Geophys. Res.*, 93, 6275– 6296.
- Blümling, P., Mooney, W.D., and Lee, W.H.K., 1985. Crustal structure of the southern Calaveras fault zone, central California, from seismic refraction investigations, *Bull. Seismol. Soc. Am.*, 75(1), 193-209.
- Brenguier, F., Shapiro, N.M., Campillo, M., Ferrazzini, V., Duputel, Z., Coutant, O. and A. Nercessian, 2008a. Towards forecasting volcanic eruptions using seismic noise, *Nature Geoscience*, 1, doi:10.1038/ngeo104.
- Brenguier, F., Campillo, M., Hadziioannou, C., Shapiro, N.M., Nadeau, R.M., and Larose, E., 2008b. Postseismic Relaxation Along the San Andreas Fault at Parkfield from Continuous Seismological Observations, *Science*, 321, 1478 – 1481.

- Brietzke, G.B. and Ben-Zion, Y., 2006. Examining tendencies of in-plane rupture to migrate to material interfaces, *Geophys. J. Int.*, 167, 807–819, doi: 10.1111/j.1365-246X.2006.03137.x.
- Brietzke, G.B., Cochard, A., and Igel, H., 2007. Dynamic rupture along bimaterial interfaces in 3D, *Geophys. Res. Lett.*, 34, L11305, doi:10.1029/2007GL029908.
- Brietzke, G.B., Cochard, A. and Igel, H., 2009. Importance of bimaterial interfaces for earthquake dynamics and strong ground motion, *Geophys. J. Int.*, 178(2), 921-938.
- Brodsky, E.E., Roeloffs, E., Woodcock, D., Gall, I. and Manga, M., 2003. A mechanism for sustained ground water pressure changes induced by distant earthquakes, *J Geophys Res*, 108, doi:10.1029/2002JB002321.
- Brown, R.D., Jr., Vedder, J.G., Wallace, R.E., Roth, E.F., Yerkes, R.F., Castle, R.O., Waananen, A.O., Page, R.W., and Eaton, J.P., 1967. The Parkfield-Cholame, California, earthquakes of June–August 1966—Surface geologic effects, water-resources aspects, and preliminary seismic data, *U.S. Geol. Surv. Prof. Paper*, 579, 66 pp.
- Catchings, R.D., Rymer, M.J., Goldman, M.R., Hole, J.A., Huggins, R., and Lippus, R., 2002. High-resolution seismic velocities and shallow structure of the San Andreas fault zone at Middle Mountain, Parkfield, California, *Bull. Seismol. Soc. Am.*, 92, 2493-2503.
- Chao, K. and Peng, Z., 2009. Temporal changes of shear wave velocity and anisotropy in the shallow crust induced by the 10/22/1999 M6.4 Chia-Yi, Taiwan, earthquake, *Geophys. J. Int.*, doi: 10.1111/j.1365-246X.2009.04384.x.
- Chen, J., Froment, B., Liu, Q. and Campillo, M., 2009. Distribution of seismic velocity change associated with the May 12, 2008 M7.9 Wenchuan earthquake. *Eos Trans. AGU*, 90(52), Fall Meet. Suppl. Abstract S24A-01.
- Cheng, X., Niu, F., and Wang, B., 2010. Coseismic velocity change in the rupture zone of the 2008 M_W 7.9 Wenchuan earthquake observed from ambient seismic noise data, *Bull. Seismol. Soc. Am.* in press.
- Chun, K.-Y., Henderson, G.A., and Liu, J., 2004. Temporal changes in P wave attenuation in the Loma Prieta rupture zone, *J. Geophys. Res.*, 109, B02317, doi:10.1029/2003JB002498.1029/2003JB002498.

- Cochran, E.S., Vidale, J.E. and Li, Y.-G., 2003. Near-fault anisotropy following the Hector Mine earthquake, *J. Geophys. Res.*, 108, 2436, doi:10.1029/2002JB002352.
- Cochran, E.S., Li, Y.-G. and Vidale, J.E., 2006. Anisotropy in the shallow crust observed around the San Andreas Fault before and after the 2004 M6 Parkfield earthquake, *Bull. Seismol. Soc. Am.*, 96, S364-S375.
- Cochran, E.S., Li, Y.-G., Shearer, P.M., Barbot, S., Fialko, Y. and Vidale, J.E., 2009. Seismic and geodetic evidence for extensive, long-lived fault damage zones, *Geology*, 37, 315-318, doi: 10.1130/G25306A.1.
- Cormier, V.F. and Spudich, P., 1984. Amplification of ground motion and waveform complexities in fault zones: examples from the San Andreas and the Calaveras faults, *Geophys. J. R. Astron. Soc.*, 79, 135–152
- Crampin, S., Booth, D.C., Evans, R., Peacock, S., and Fletcher, J.B., 1990. Change in shear-wave splitting at Anza near the time of the North Palm Springs earthquake, *J. Geophys. Res.*, 95, 11197 – 11212.
- Dalguer, L.A. and Day, S.M., 2007. Asymmetric pulse-like rupture at bimaterial interface with slip-weakening friction model, *EOS Trans. AGU, Fall Meet. Suppl.*, 88(52), Abstract S14B–03.
- Dibblee, T.W., Graham, S.E., Mahony, T.M., Blissenbach, J.L., Mariant, J.J. and Wentworth, C.M., 1999. Regional geological map of San Andreas and related faults in Carrizo Plain, Temblor, Caliente and La Panza Ranges and vicinity, California: a digital database, *U.S. Geol. Surv. Open-File Rept.* 99-14, scale: 1: 125,000.
- Eberhart-Phillips, D. and Michael, A.J., 1993. Three-dimensional velocity structure, seismicity, and fault structure in the Parkfield region, central California, *J. Geophys. Res.*, 98, 15,737–15,758.
- Eshelby, J.D., 1957. The determination of the elastic field of an ellipsoidal inclusion, and related problems, *Proc. Roy. Soc.*, A241, 376–396.
- Fialko, Y., 2006. Interseismic strain accumulation and the earthquake potential on the southern San Andreas fault system, *Nature*, 441, 968–971.

- Fielding, E.J., Lundgren, P.R., Bürgmann, R. and Funning, G.J., 2009. Shallow fault-zone dilatancy recovery after the 2003 Bam earthquake in Iran, *Nature*, 458, doi: 10.1038/nature07817.
- Finzi, Y., Hearn, E.H., Ben-Zion Y., and Lyakhovsky, V., 2009. Structural properties and deformation patterns of evolving strike-slip faults: Numerical simulations incorporating damage rheology, *Pure Appl. Geophys.*, 166, 1537-1573, doi: 10.1007/s00024-009-0522-1.
- Fischer, A.D., Peng, Z., and Sammis, C.G., 2008. Dynamic triggering of high-frequency bursts by strong motions during the 2004 Parkfield earthquake sequence, *Geophys. Res. Lett.*, 35, L12305, doi:10.1029/2008GL033905.
- Fuis, G.S., Ryberg, T., Godfrey, N.J., Okaya, D.A., and Murphy, J.M., 2001. Crustal structure and tectonics from the Los Angeles basin to the Mojave Desert, southern California, *Geology*, 29, 15–18.
- Fuis, G.S., Clayton, R.W., Davis, P.M., Ryberg, T., Lutter, W.J., Okaya, D.A., Prodehl, C., Kohler, M.D., Hauksson, E., Murphy, J.M., Benthien, M.L., Baher, S.A., Thygesen, K., Simila, G. and Keller, G.R., 2003. Fault systems of the 1971 San Fernando and 1994 Northridge earthquakes, southern California: Relocated aftershocks and seismic images from LARSE II, *Geology*, 31(2), 171–174.
- Gerstoft, P., Sabra, K.G., Roux, P., Kuperman, W.A., and Fehler, M.C., 2006. Green's functions extraction and surface-wave tomography from microseisms in southern California, *Geophysics*, 71, SI23-SI31.
- Gomberg, J., Reasenber, P., Bodin, P. and Harris, R., 2001. Earthquake triggering by transient seismic waves following the Landers and Hector Mine, California earthquakes, *Nature*, 411, 462-466.
- Gomberg, J., Bodin, P., Larson, K. and Dragert, H., 2004. The fundamental process of earthquake nucleation by transient deformations revealed by the M7.9 Denali, Alaska earthquake, *Nature*, 427, 621-624.
- Gomberg, J., Rubinstein, J.L., Peng, Z., Creager, K.C. and Vidale, J.E., 2008. Widespread triggering of non-volcanic tremor in California, *Science*, 319, 173, doi:10.1126/science.1149164.

- Guilhem, A., Peng, Z., and Nadeau, R.M., 2010. High-frequency identification of non-volcanic tremor along the San Andreas Fault triggered by regional earthquakes, *Geophys. Res. Lett.*, in review.
- Graymer, R.W., Jones, D.L., and Brabb, E.E., 1994. Preliminary geologic map emphasizing bedrock formations in Contra Costa County, California: A digital database, U.S. Geol. Surv. Open-File Rept. 94-622.
- Graymer, R.W., Jones, D.L., and Brabb, E.E., 1995. Geology of the Hayward fault zone: A digital map database, U.S. Geol. Surv. Open-File Rept. 95-597, 16 pp.
- Haney, M.M., van Wijk, K., Preston, L.A., and Aldridge, D.F., 2009. Observation and modeling of source effects in coda wave interferometry at Pavlof volcano, *The Leading Edge*, 28, 554-560, doi: 10.1190/1.3124930.
- Hadziioannou, C., Larose, E., Coutant, O., Roux, P. and Campillo, M. 2009. Stability of Monitoring Weak Changes in Multiply Scattering Media with Ambient Noise Correlation: Laboratory Experiments, *J. Acoust. Soc. Am.*, 125(6), 3688-3695.
- Hardebeck, J.L., Michael, A.J., Brocher, T.M., 2007. Seismic velocity structure and seismotectonics of the eastern San Francisco bay region, California, *Bull. Seismol. Soc. Am.*, 97(3), doi: 10.1785/0120060032.
- Harris, R.A., 2004. A scientific hypothesis debunked by parkfield earthquakes – material contrasts and rupture directivity, *EOS Trans. Amer. Geophys. Union*, 85, S54B-08.
- Harris, R.A. and Day, S.M., 2005. Material contrast does not predict earthquake rupture propagation direction, *Geophys. Res. Lett.*, 32, L23301, doi:10.1029/2005GL023941.
- Hickman, S., Zoback, M.D. and Ellsworth, W., 2004. Introduction to special section: Preparing for the San Andreas Fault Observatory at Depth, *Geophys. Res. Lett.*, 31, L12S01, doi:10.1029/2004GL020688.
- Hill, D.P., et al., 1993. Seismicity remotely triggered by the magnitude 7.3 Landers, California, earthquake, *Science*, 260, 1617–1623.

- Hill, D.P. and Prejean, S.G., 2007. Dynamic triggering, in *Treatise on Geophysics*, 257–292, ed. Schubert G, Vol. 4: Earthquake Seismology, ed. Kanamori H, Elsevier, Amsterdam.
- Hough, S.E. and Kanamori, H., 2002. Source properties of earthquakes near the Salton Sea triggered by the 16 October 1999 M 7.1 Hector Mine, California, earthquake, *Bull. Seism. Soc. Am.*, 92, 1281-1289, doi: 10.1785/0120000910.
- Hough, S.E., Ben-Zion, Y. and Leary, P., 1994. Fault zone waves observed at the southern Joshua Tree earthquake rupture zone, *Bull. Seismol. Soc. Am.*, 84, 761–767.
- Jin, A. and Aki, K., 1986. Temporal change in coda Q before the Tangshan earthquake of 1976 and the Haicheng earthquake of 1975, *J. Geophys. Res.*, 91, 665 – 673.
- Johnson, P.A. and Jia, X., 2005. Nonlinear dynamics, granular media and dynamic earthquake triggering, *Nature*, 437, 871-874, doi: 10.1038/nature04015.
- Johnson, P.A., Zinszner, B. and Rasolofosaon, P.N.J., 1996. Resonance and elastic nonlinear phenomena in rock, *J. Geophys. Res.*, 101(B5), 11,553–11,564.
- Kanamori, H., 1977. The energy release in great earthquakes, *J. Geophys. Res.*, 82, 2981-2988.
- Karabulut, H. and Bouchon, M., 2007. Spatial variability and non-linearity of strong ground motion near a fault, *Geophys. J. Int.*, 170, 262-274, doi:10.1111/j.1365-246X.2007.03406.x.
- Kaneko, Y. and Lapusta, N., 2008. Variability of earthquake nucleation in continuum models of rate-and-state faults and implications for aftershock rates, *J. Geophys. Res.*, 113, B12312, doi:10.1029/2007JB005154.
- Langbein, J., Borchardt, R., Dreger, D., Fletcher, J., Hardebeck, J.L., Hellweg, M., J., C., Johnston, M., Murray, J.R. and Nadeau, R., 2005. Preliminary report on the 28 September 2004, M 6.0 Parkfield, California earthquake, *Seism. Res. Lett.*, 76, 10-26.

- Le Pichon, X., Kreemer, C. and Chamot-Rooke, N., 2005. Asymmetry in elastic properties and the evolution of large continental strike-slip faults, *J. Geophys. Res.*, 110, B03405, doi:10.1029/2004JB003343.
- Lees, J.M. and Malin, P.E., 1990. Tomographic images of P-wave velocity variation at Parkfield, California, *J. Geophys. Res.*, 95(B13), 21,793–21,804.
- Lengliné, O. and Marsan D., 2009. Inferring the coseismic and postseismic stress changes caused by the 2004 $M_w = 6$ Parkfield earthquake from variations of recurrence times of microearthquakes, *J. Geophys. Res.*, 114, B10303, doi:10.1029/2008JB006118.
- Lewis, M.A., Peng, Z., Ben-Zion, Y., and Vernon, F.L., 2005. Shallow seismic trapping structure in the San Jacinto fault zone near Anza, California, *Geophys. J. Int.*, 162(3), 867-881, doi: 10.1111/j.1365-246X.2005.02684.
- Lewis, M.A., Ben-Zion, Y. and McGuire, J.J., 2007. Imaging the deep structure of the San Andreas Fault south of Hollister with joint analysis of fault-zone head and direct P arrivals, *Geophys. J. Int.*, doi:10.1111/j.1365-246X.2006.03319.x.
- Li, Y.-G., Vidale, J.E., Aki, K., Xu, F., and Burdette, T., 1998. Evidence of shallow fault zone strengthening after the 1992 $M_{7.5}$ Landers, California, earthquake, *Science*, 279, 217-219.
- Li, Y.-G., Chen, P., Cochran, E.S., Vidale, J.E. and Burdette, T., 2006. Seismic evidence for rock damage and healing on the San Andreas Fault associated with the 2004 $M 6.0$ Parkfield earthquake, *Bull. Seismol. Soc. Am.*, 96(4B), 349-363.
- Lindh, A.G. and Boore, D.M., 1981. Control of rupture by fault geometry during the 1966 Parkfield earthquake, *Bull. Seismol. Soc. Am.*, 71, 95–116.
- Liu, Y., Teng, T.-L., and Ben-Zion, Y., 2004. Systematic analysis of shear-wave splitting in the aftershock zone of the 1999 Chi-Chi earthquake: Shallow crustal anisotropy and lack of precursory variations, *Bull. Seismol. Soc. Am.*, 94, 2330 – 2347.
- Lutter, W.J., Fuis, G.S., Ryberg, T., Okaya, D.A., Clayton, R.W., Davis, P.M., Prodehl, C., Murphy, J.M., Langenheim, V.E., Benthien, M.L., Godfrey, N.J., Christensen, N.I., Thygesen, K., Thurber, C.H., Simila, G. and Keller, G.R., 2004. Upper crustal structure from the Santa Monica mountains to the Sierra Nevada, southern

- California: tomographic results from the Los Angeles regional seismic experiment, Phase II (LARSE II), *Bull. Seismol. Soc. Am.*, 94(2), 619–632.
- Ma, S., 2008. A physical model for widespread near-surface and fault zone damage induced by earthquakes, *Geochem. Geophys. Geosyst.*, 9, Q11009, doi:10.1029/2008GC002231.
- Manaker, D.M., Michael, A.J. and Bürgmann, R., 2005. Subsurface structure and kinematics of the Calaveras-Hayward fault stepover from three-dimensional Vp and seismicity, San Francisco Bay Region, California, *Bull. Seismol. Soc. Am.*, 95(2), 446–470.
- Manga, M. and Brodsky, E.E., 2006. Seismic triggering of eruptions in the far field: Volcanoes and geysers, *Annu. Rev. Earth. Planet. Sci.*, 34, 263–291.
- Manga, M. and Wang, C.-Y., 2007. Earthquake hydrology, in *Treatise on Geophysics 4*: 293–320, ed. Schubert, G., Elsevier Science, Amsterdam.
- Marzorati, S. and Bindi, D., 2008. Characteristics of ambient noise cross correlations in northern Italy within the frequency range of 0.1–0.6 Hz, *Bull. Seismol. Soc. Am.*, 98, 1389–1398, doi: 10.1785/0120070140.
- Matsumoto, S., Obara, K., Yoshimoto, K., Saito, T., Ito, A., and Hasegawa, A., 2001. Temporal change in P-wave scatterer distribution associated with the M6.1 earthquake near Iwate volcano, northeastern Japan, *Geophys. J. Int.*, 145, 48–58.
- McLaughlin, R.J., Sliter, W.V., Sorg, D.H., Russell, P.C., and Sarna-Wojcicki, A.M., 1996. Large-scale right-slip displacement on the east San Francisco Bay region fault system, California: implications for location of late Miocene to Pliocene Pacific plate boundary, *Tectonics*, 15, 1–18.
- McGuire, J.J. and Ben-Zion, Y., 2005. High-resolution imaging of the Bear Valley section of the San Andreas fault at seismogenic depths with fault-zone head waves and relocated seismicity, *Geophys. J. Int.*, 163, 152–164.
- McGuire, J.J., Zhao, L. and Jordan, T.H., 2001. Teleseismic inversion for the second-degree moments of earthquake space–time distributions, *Geophys. J. Int.*, 145, 661–678.

- McPhee, D.K., Jachens, R.C and Wentworth, C.M., 2004. Crustal structures across the San Andreas Fault at the SAFOD site from potential field and geologic studies, *Geophys. Res. Lett.*, 31, L12S03, doi: 10.1029/2003GL019363.
- Menke, W., 1999. Using waveform similarity to constrain earthquake locations, *Bull. Seismol. Soc. Am.*, 89, 1143-1146.
- Michael, A., 1988. Effects of three-dimensional velocity structure on the seismicity of the 1984 Morgan Hill, California, aftershock sequence, *Bull. Seismol. Soc. Am.*, 78, 1199–1221.
- Michelini, A and McEvilly, T.V., 1991. Seismological studies at Parkfield. I. Simultaneous inversion for velocity structure and hypocenters using cubic B-splines parameterization, *Bull. Seismol. Soc. Am.*, 81, 524-552.
- Miyazawa, M. and Brodsky, E.E., 2008. Deep low-frequency tremor that correlates with the passing surface waves, *J. Geophys. Res.*, 113, B01307, doi:10.1029/2006JB004890.
- Miyazawa, M., Brodsky, E.E., and Mori, J., 2008. Learning from dynamic triggering of low-frequency tremor in subduction zones, *Earth Planets Space*, 60(10), e17-e20.
- Mogi, K., 1979. Global variations of seismic activity, *Tectonophysics*, 57, T43-T50.
- Mooney, W.D. and Colburn, R.H., 1985. A seismic-refraction profile across the San Andreas, Sargent, and Calaveras faults, west-central California, *Bull. Seismol. Soc. Am.*, 75, 175-191.
- Mooney, W.D. and Ginzburg, A., 1986. Seismic measurements of the internal properties of fault zones, *Pure appl. Geophys.*, 124, 141-157.
- Nadeau, R.M. and Guilhem, A., 2009. Nonvolcanic tremor and the 2003 San Simeon and 2004 Parkfield, California earthquakes, *Science*, 325, 191-193.
- Nadeau, R.M., Foxall, W. and McEvilly, T.V., 1995. Clustering and periodic recurrence of microearthquakes on the San Andreas Fault at Parkfield, California, *Science*, 267, 503–507.

- Nishimura, T., Tanaka, S., Yamawaki, T., Yamamoto, H., Sano, T., Sato, M., Nakahara, H., Uchida, N., Hori, S. and Sato, H., 2005. Temporal changes in seismic velocity of the crust around Iwate volcano, Japan, as inferred from analyses of repeated active seismic experiment data from 1998 to 2003, *Earth Planets Space*, 57,491-505.
- Niu, F., Silver, P.G., Nadeau, R.M. and McEvilly, T.V., 2003. Stress-induced migration of seismic scatters associated with 1993 Parkfield aseismic transient event, *Nature*, 426, 544-548.
- Niu, F., Silver, P.G., Daley, T., Cheng, X., and Majer, E., 2008. Prerupture dilatancy observed from active source monitoring at the Parkfield SAFOD drill site, *Nature*, 454, doi:10.1038/nature07111.
- Ohmi, S., Hirahara, K., Wada, H. and Ito, K., 2008. Temporal variations of crustal structure in the source region of the 2007 Noto Hanto Earthquake, central Japan, with passive image interferometry, *Earth Planets Space*, 60(10), 1069-1074.
- Olsen, K.B., Day, S.M., Minster, J.B., Cui, Y., Chourasia, A., Faerman, M., Moore, R., Maechling, P. and Jordan, T., 2006. Strong shaking in Los Angeles expected from southern San Andreas earthquake, *Geophys. Res. Lett.*, 33, L07305, doi:10.1029/2005GL025472.
- Oppenheimer, D.H., Bakun, W.H. and Lindh, A.G., 1990. Slip partitioning of the Calaveras fault, California, and prospects for future earthquakes, *J. Geophys. Res.*, 95, 8483–8498.
- Pacheco, C. and Snieder, R., 2006. Time-lapse travelttime change of single scattered acoustic waves, *Geophys. J. Int.*, 165, 485-500.
- Page, B.M., 1981. The southern Coast Ranges, in *The Geotectonic Development of California*, W. G. Ernst (Editor), Prentice–Hall, New York, 329–417.
- Page, B.M., 1984. The Calaveras fault zone of California, an active plate boundary element, in *The 1984 Morgan Hill, California Earthquake*, California Division of Mines and Geology Special Publication 68, J. H. Bennett and R. W. Sherburne, Editors, Sacramento, California, 109–122.

- Parsons, T., 2002. Global Omori law decay of triggered earthquakes: Large aftershocks outside the classical aftershock zone, *J. Geophys. Res.*, 107(B9), 2199, doi:10.1029/2001JB000646.
- Peng, Z. and Ben-Zion, Y., 2004. Systematic analysis of crustal anisotropy along the Karadere-Duzce branch of the north Anatolian fault, *Geophys. J. Int.*, 159, 253-274, doi: 10.1111/j.1365-246X.2004.02379.x.
- Peng, Z. and Ben-Zion, Y., 2005. Spatio-temporal variations of crustal anisotropy from similar events in aftershocks of the 1999 M7.4 İzmit and M7.1 Duzce, Turkey, earthquake sequences, *Geophys. J. Int.*, 160, 1027-1043, doi: 10.1111/j.1365-246X.2004.02379.x.
- Peng, Z. and Ben-Zion, Y., 2006. Temporal changes of shallow seismic velocity around the Karadere-Duzce branch of the North Anatolian fault and strong ground motion, *Pure appl. Geophys.*, 163, 567-599.
- Peng, Z. and Chao, K., 2008. Non-volcanic tremor beneath the Central Range in Taiwan triggered by the 2001 M_W 7.8 Kunlun earthquake, *Geophys. J. Int. (fast track)*, 825–829, 10.1111/j.1365-246X.2008.03886.x.
- Peng, Z. and Zhao P., 2009. Migration of early aftershocks following the 2004 Parkfield earthquake, *Nature Geosci.*, 2, 877–881, doi: 10.1038/ngeo697.
- Peng, Z., Ben-Zion, Y., Michael, A.J. and Zhu, L., 2003. Quantitative analysis of fault zone waves in the rupture zone of the Landers, 1992, California earthquake: Evidence for a shallow trapping structure, *Geophys. J. Int.*, 155, 1021-1041. doi: 10.1111/j.1365-246X.2003.02109.x
- Peng, Z., Vidale, J.E., Marone C. and Rubin A., 2005. Systematic variations in recurrence interval and moment of repeating aftershocks, *Geophys. Res. Lett.*, 32(15), L15301, doi: 10.1029/2005GL022626.
- Peng, Z., Vidale, J.E. and Houston, H., 2006. Anomalous early aftershock decay rates of the 2004 M6 Parkfield earthquake, *Geophys. Res. Lett.*, 33, L17307, doi:10.1029/2006GL026744.
- Peng, Z., Vidale, J.E., Ishii, M. and Helmstetter, A., 2007. Seismicity rate immediately before and after main shock rupture from high-frequency waveforms in Japan, *J. Geophys. Res.*, 112, B03306, doi:10.1029/2006JB004386.

- Peng, Z., Vidale, J.E., Creager, K.C., Rubinstein, J.L., Gomberg, J., and Bodin, P., 2008. Strong tremor near Parkfield, CA excited by the 2002 Denali Fault earthquake, *Geophys. Res. Lett.*, 35, L23305, doi:10.1029/2008GL036080.
- Peng, Z., Vidale, J.E., Wech, A., Nadeau, R.M., and Creager, K.C., 2009. Remote triggering of tremor along the San Andreas fault in central California, *J. Geophys. Res.*, 114, B00A06, doi:10.1029/2008JB006049.
- Peng, Z., Wang, W., Chen, Q.-F., and Jiang, T., 2010. Remotely triggered seismicity in northeast China following the 2008 M_w 7.9 Wenchuan earthquake, *Earth Planets Space*, in press.
- Phillips, W.S. and Aki, K., 1986. Site amplification of coda waves from local earthquakes in Central California, *Bull. Seismol. Soc. Am.*, 76, 627-648.
- Poupinet, G., Ellsworth, W.L. and Frechet, J., 1984. Monitoring velocity variations in the crust using earthquake doublets: an application to the Calaveras fault, California, *J. Geophys. Res.*, 89(B7), 5719–5731.
- Prejean, S.G., Hill, D.P., Brodsky, E.E., Hough, S.E., Johnston, M.J.S., Malone, S.D., Oppenheimer, D.H., Pitt, A.M. and Richards-Dinger, K.B., 2004. Remotely triggered seismicity on the United States west coast following the M_w 7.9 Denali fault earthquake, *Bull. Seismol. Soc. Am.*, 94, 348-359.
- Press, W., Flannery B., Teukolsky S., and Vetterling W., 1986. *Numerical Recipes*, Cambridge University Press, Cambridge, U.K.
- Ranjith, K. and Rice, J.R., 2001. Slip dynamics at an interface between dissimilar materials, *J. Mech. Phys. Solids*, 49, 341–361.
- Rolandone, F., Burgmann, R. and Nadeau, R.M., 2004. The evolution of the seismic-aseismic transition during the earthquake cycle: Constraints from the time-dependent depth distribution of aftershocks, *Geophys. Res. Lett.*, 31, L23610, doi:10.1029/2004GL021379.
- Rockwell, T.K. and Ben-Zion, Y. 2007. High localization of primary slip zones in large earthquakes from paleoseismic trenches: Observations and implications for earthquake physics, *J. Geophys. Res.*, 112, B10304, doi:10.1029/2006JB004764.

- Roeloffs, R.A., 1998. Persistent water level changes in a well near Parkfield, California, due to local and distant earthquakes, *J. Geophys. Res.*, 103, B1, 869-890, doi: 10.1029/97JB02335.
- Rost, S. and Thomas, C. 2002. Array seismology: Methods and applications, *Rev. Geophys.*, 40(3), 1008, doi:10.1029/2000RG000100.
- Rovelli, A., Caserta, A., Marra, F. and Ruggiero, V., 2002. Can seismic waves be trapped inside an inactive fault zone? The case study of Nocera Umbra, central Italy, *Bull. Seismol. Soc. Am.*, 92, 2217–2232.
- Rubin, A.M., 2002. Using repeating earthquakes to correct high-precision earthquake catalogs for time-dependent station delays, *Bull. Seismol. Soc. Am.*, 92, 1647–1659.
- Rubinstein, J. 2010. Nonlinear strong ground motion in medium magnitude earthquakes near Parkfield, CA, *Bull. Seismol. Soc. Am.*, in press.
- Rubinstein, J.L. and Beroza, G.C., 2004a. Evidence for widespread nonlinear strong ground motion in the M_w 6.9 Loma Prieta earthquake, *Bull. Seismol. Soc. Am.*, 94, 1595-1608.
- Rubinstein, J.L. and Beroza, G.C., 2004b. Nonlinear strong ground motion in the ML 5.4 Chittenden earthquake: Evidence that preexisting damage increases susceptibility to further damage, *Geophys. Res. Lett.*, 31, L23614, doi: 10.1029/2004GL021357
- Rubinstein, J.L. and Beroza, G.C., 2005. Depth constraints on nonlinear strong ground motion from the 2004 Parkfield earthquake, *Geophys. Res. Lett.*, 32, L14313, doi: 10.1029/2005GL023189.
- Rubinstein, J. L., Uchida, N. and Beroza, G.C., 2007a. Seismic velocity reductions caused by the 2003 Tokachi-Oki earthquake, *J. Geophys. Res.*, 112, B05315, doi:10.1029/2006JB004440.
- Rubinstein, J.L., Vidale, J.E., Gomberg, J., Bodin, P., Creager, K.C., and Malone, S.D., 2007b. Non-volcanic tremor driven by large transient shear stresses, *Nature*, 448, 579-582.

- Rubinstein, J.L., Gomberg, J., Vidale, J.E., Wech, A.G., Kao, H., Creager, K.C., and Rogers, G., 2009. Seismic wave triggering of nonvolcanic tremor, episodic tremor and slip, and earthquakes on Vancouver Island, *J. Geophys. Res.*, 114, B00A01, doi:10.1029/2008JB005875.
- Rymer, M.J., Tinsley, J.C., Treiman, J.A., Arrowsmith, J.R., Clahan, K.B., Rosinski, A.M., Bryant, W.A., Snyder, H.A., Fuis, G.S., Toke, N. and Bawden, G.W., 2006. Surface fault slip associated with the 2004 Parkfield, California, Earthquake, *Bull. Seismol. Soc. Am.*, 96(4B), S11–S27.
- Sabra, K.G., Gerstoft, P., Roux, P., Kuperman, W.A., and Fehler, M.C., 2005a. Extracting time-domain Green's function estimates from ambient seismic noise, *Geophys. Res. Lett.*, 32, L03310, doi: 10.1029/2004GL021862.
- Sabra, K.G., Gerstoft, P., Roux, P., Kuperman, W.A., and Fehler, M.C., 2005b. Surface wave tomography from microseisms in Southern California, *Geophys. Res. Lett.*, 32, L14311, doi: 10.1029/2005GL023155.
- Sabra, K.G., Roux, P., Gerstoft, P., Kuperman, W.A., and Fehler, M. 2006. Extracting coherent coda arrivals from cross-correlations of long period seismic waves during the Mount St. Helens 2004 eruption, *Geophys. Res. Lett.*, 33, L06313, doi:10.1029/2005GL025563.
- Sawazaki, K., Sato, H., Nakahara, H. and Nishimura, T., 2006. Temporal change in site response caused by earthquake strong motion as revealed from coda spectral ratio measurement, *Geophys. Res. Lett.*, 33, L21303, doi:10.1029/2006GL027938.
- Sawazaki, K., Sato, H., Nakahara, H. and Nishimura, T., 2009. Time-lapse changes of seismic velocity in the shallow ground caused by strong ground motion shock of the 2000 Western-Tottori earthquake, Japan, as revealed from coda deconvolution analysis, *Bull. Seismol. Soc. Am.*, 99, 352-366.
- Schaff, D.P. and Beroza, G.C., 2004. Coseismic and postseismic velocity changes measured by repeating earthquakes, *J. Geophys. Res.*, 109, B10302, doi: 10.1029/2004JB003011.
- Schaff, D.P., Bokelmann, G.H.R., Beroza, G.C., Waldhauser, F. and Ellsworth, W.L., 2002. High-resolution image of Calaveras fault seismicity, *J. Geophys. Res.*, 107(B9), 2186, doi: 10.1029/2001JB000633.

- Sens-Schönfelder, C. and Wegler, U., 2006. Passive image interferometry and seasonal variations of seismic velocities at Merapi Volcano, Indonesia, *Geophys. Res. Lett.*, 33, L21302, doi: 10.1029/2006GL027792.
- Shapiro, N.M., Campillo, M., Stehly, L. and Ritzwoller, M.H., 2005. High-resolution surface-wave tomography from ambient seismic noise, *Science*, 307, 1615–1618, doi: 10.1126/science.1108339.
- Shi, Z. and Ben-Zion, Y., 2006. Dynamic Rupture on a bimaterial interface governed by slip-weakening friction, *Geophys. J. Int.*, 164, doi: 10.1111/j.1365-246X.2006.02853.x.
- Sieh, K., 1978. Slip along the San Andreas fault associated with the great 1857 earthquake, *Bull. Seismol. Soc. Am.*, 68, 1421–1448.
- Silver, P.G., Daley, T.M., Niu, F., and Majer, E.L., 2007. Active source monitoring of cross-well seismic travel time for stress-induced changes, *Bull. Seismol. Soc. Am.*, 97, 1B, 281–293, doi: 10.1785/0120060120.
- Simpson, R.W., Barall, M., Langbein, J., Murray, J.R. and Rymer, M.J., 2006. San Andreas fault geometry in the Parkfield, California, region, *Bull. Seismol. Soc. Am.*, 96(4B), S28-S37.
- Snieder, R., Grêt, A., Douma, H., Scales, J., 2002. Coda Wave Interferometry for Estimating Nonlinear Behavior in Seismic Velocity, *Science*, 295, 2253–2255, doi: 10.1126/science.1070015.
- Sleep, N., 2009. Depth of Rock Damage from Strong Seismic Ground Motions near the 2004 Parkfield Mainshock, *Bull. Seismol. Soc. Am.*, 99(5), 3067–3076, doi: 10.1785/0120090065.
- Sleep, N.H. and Ma, S., 2008. Production of brief extreme ground acceleration pulses by nonlinear mechanisms in the shallow subsurface, *Geochem. Geophys. Geosyst.*, 9, Q03008, doi:10.1029/2007GC001863.
- Spudich, P. and Olsen, K.B., 2001. Fault zone amplified waves as a possible seismic hazard along the Calaveras fault in central California, *Geophys. Res. Lett.*, 28, 2533–2536.

- Sylvester, A.G., 1988. Strike-slip faults, *Geol. Soc. Am.*, 100, 1666–1703.
- Taira, T., Silver, P.G., Niu, F. and Nadeau, R.M., 2008. Detecting seismogenic stress evolution and constraining fault zone rheology in the San Andreas Fault following the 2004 Parkfield earthquake, *J. Geophys. Res.*, 113, B03303, doi: 10.1029/2007JB005151.
- Taira, T., Silver, P.G., Niu, F., and Nadeau, R.M., 2009. Seismic evidence for remote triggering of fault-strength changes on the San Andreas fault at Parkfield, *Nature*, 461, 636–640.
- Templeton, D.C., Nadeau, R.M. and Bürgmann, R., 2008. Behavior of repeating earthquake sequences in Central California and the implications for subsurface fault creep, *Bull. Seismol. Soc. Am.*, 98, 52-65.
- Templeton, D.C., Nadeau, R.M. and Bürgmann, R., 2009. Distribution of postseismic slip on the Calaveras fault, California, following the 1984 M6.2 Morgan Hill earthquake, *Earth and Planetary Science Letters*, 277, doi:10.1016/j.epsl.2008.1009.1024.
- TenCate, J.A., Pasqualini, D., Habib, S., Heitmann, K., Higdon, D., and Johnson, P.A., 2004. Nonlinear and Nonequilibrium Dynamics in Geomaterials, *Phys. Rev. Lett.*, 93, doi: 10.1103/PhysRevLett.93.065501.
- Thurber, C.H., Roecker, S., Roberts, K., Gold, M., Powell, L. and Rittger, K., 2003. Earthquake locations and three-dimensional fault zone structure along the creeping section of the San Andreas Fault near Parkfield, CA: Preparing for SAFOD, *Geophys. Res. Lett.*, 30, doi 10.1029/2002GL016004.
- Thurber, C.H., Roecker, S., Zhang, H., Baher, S. and Ellsworth, W., 2004. Fine-scale structure of the San Andreas fault and location of the SAFOD target earthquakes, *Geophys. Res. Lett.* 31, L12S02, doi: 10.1029/2003GL019398.
- Thurber, C.H., Zhang, H., Waldhauser, F., Hardebeck, J., Michael, A. and Eberhart-Phillips, D., 2006. Three-dimensional compressional wavespeed model, earthquake relocations, and focal mechanisms for the Parkfield, California, region, *Bull. Seismol. Soc. Am.*, 96(4B), S38-S49, doi: 10.1785/0120050825.

- Thurber, C.H., Brocher, T.M., Zhang, H. and Langenheim V.E., 2007. Three-dimensional P wave velocity model for the San Francisco Bay region, California, *J. Geophys. Res.*, 112, B07313, doi: 10.1029/2006JB004682.
- Velasco, A.A., Hernandez, S., Parsons, T., and Pankow, K., 2008. Global ubiquity of dynamic earthquake triggering, *Nature Geoscience*, 1, 375–379, doi:10.1038/ngeo204.
- Vidale, J.E. and Li, Y., 2003. Damage to the shallow Landers fault from the nearby Hector Mine earthquake, *Nature*, 421, 524-426.
- Waldhauser, F. and Ellsworth, W.L., 2000. A double-difference earthquake location algorithm: method and application to the northern Hayward Fault, *Bull. Seismol. Soc. Am.*, 90, 1330-1368.
- Waldhauser, F. and Ellsworth, W.L., 2002. Fault structure and mechanics of the Hayward Fault, California, from double-difference earthquake locations, *J. Geophys. Res.*, 107(B3), 2054, doi:10.1029/2000JB000084.
- Waldhauser, F. and Schaff, D.P., 2008. Large-scale relocation of two decades of Northern California seismicity using cross-correlation and double-difference methods, *J. Geophys. Res.*, 113, B08311, doi:10.1029/2007JB005479.
- Waldhauser, F., Ellsworth, W.L., Schaff, D.P. and Cole, A., 2004. Streaks, multiplets, and holes: High-resolution spatio-temporal behavior of Parkfield seismicity, *Geophys. Res. Lett.*, 31, L18608, doi:10.1029/2004GL020649.
- Walter, A.W. and Mooney, W.D., 1982. Crustal structure of the Diablo and Gabilan ranges central California; a reinterpretation of existing data, *Bull. Seismol. Soc. Am.*, 72, 1567–1590.
- Wang, C., Chia, Y., Wang, P., and Dreger, D., 2009. Role of S waves and Love waves in coseismic permeability enhancement, *Geophys. Res. Lett.*, 36, L09404, doi:10.1029/2009GL037330.
- Wdowinski S., Smith-Konter, B., Bock, Y. and Sandwell, D., 2007. Diffuse interseismic deformation across the Pacific-North America plate boundary, *Geology*, 35(4), 311–314.

- Weertman, J., 1980. Unstable slippage across a fault that separates elastic media of different elastic constants, *J. Geophys. Res.*, 85, 1455–1461.
- Weertman, J., 2002. Subsonic type earthquake dislocation moving at approximately $\sqrt{2} \times$ shear wave velocity on interface between half spaces of slightly different elastic constants, *Geophys. Res. Lett.*, 29(10), doi:10.1029/2001GL013916.
- Wegler, U. and Sens-Schönfelder, C., 2007. Fault zone monitoring with passive image interferometry, *Geophys. J. Int.*, 168, 1029-1033.
- Wegler, U., Nakahara, H., Korn, M. and Shiomi, K., 2009. Sudden drop of seismic velocity after the 2004 M_w 6.6 Mid-Niigata earthquake, Japan, observed with passive image interferometry, *J. Geophys. Res.*, 114, B06305, doi:10.1029/2008JB005869.
- Whitcomb, J.H, Garmany, J.E. and Anderson, D.L., 1973. Earthquake prediction: Variation of seismic velocities before the San Francisco earthquake, *Science*, 180, 632 – 635.
- Wu, J., Hole, J.A., J.A. Snoke, J.A. and Imhof, M.G., 2008. Depth extent of the fault zone seismic waveguide: Effects of increasing velocity with depth, *Geophys. J. Int.*, 173, 611-622.
- Wu, C., Peng, Z. and Ben-Zion, Y., 2009a. Non-linearity and temporal changes of fault zone site response associated with strong ground motion, *Geophys. J. Int.*, 176, 265-278, doi: 10.1111/j.1365-246X.2008.04005.x.
- Wu, C., Peng, Z. and Assimaki D., 2009. Temporal changes in site response associated with strong ground motion of 2004 M_w 6.6 Mid-Niigata earthquake sequences in Japan, *Bull. Seismol. Soc. Am.*, 99(6), 3487-3495, doi: 10.1785/0120090108.
- Wu, C., Peng, Z., and Ben-Zion, Y., 2010. Refined thresholds for nonlinear ground motion and temporal changes of site response associated with medium size earthquakes, *Geophys. J. Int.*, revised.
- Xu, Z. J. and Song, X., 2009. Temporal changes of surface wave velocity associated with major Sumatra earthquakes from ambient noise correlation, *Proc. Natl. Acad. Sci. USA*, 106(34), 14207-14212.

- Zhang, J., Gerstoft, P., Shearer, P.M., 2009. High-frequency P-wave seismic noise driven by ocean winds, *Geophys. Res. Lett.*, 36, L09302, doi: 10.1029/2009GL037761.
- Zhang, H., Liu, Y., Thurber, C. and Roecker, S., 2007. Three-dimensional shear-wave splitting tomography in the Parkfield, California, region, *Geophys. Res. Lett.*, 34, L24308, doi:10.1029/2007GL031951.
- Zhao, P. and Peng, Z., 2008. Velocity contrast along the Calaveras fault from analysis of fault zone head waves generated by repeating earthquakes, *Geophys. Res. Lett.*, 35, L01303, doi:10.1029/2007GL031810.
- Zhao, P. and Peng, Z., 2009. Depth extent of damage zones around the central Calaveras fault from waveform analysis of repeating earthquakes, *Geophys. J. Int.*, 179, 1817-1830, doi: 10.1111/j.1365-246X.2009.04385.x.
- Zhao, P., Peng, Z., Shi, Z., Lewis, M., and Ben-Zion, Y. 2010a. Variations of the velocity contrast and rupture properties of M6 earthquakes along the Parkfield section of the San Andreas fault, *Geophys. J. Int.*, 180, 765-780, 10.1111/j.1365-246X.2009.04436.x.
- Zhao, P., Peng, Z., and Sabra K., 2010b. Detecting remotely triggered temporal changes around the Parkfield section of the San Andreas Fault, *Earthquake Science, Special Issue on Ambient Noise Seismology*, Submitted.
- Zhou, Y., McNally, K.C. and Lay, T., 1993. Analysis of the 1986 Mt. Lewis, California, earthquake: preshocks sequence-mainshock-aftershock sequence, *Phys. Earth Planet. Inter.*, 75, 267-288.
- Zinszner, B., Johnson, P.A. and Rasolofosaon, P.N.J., 1997. Influence of change in physical state on elastic nonlinear response in rock: Significance of effective pressure and water saturation, *J. Geophys. Res.*, 102(B4), 8105–8120.